

**University of Alberta**

**Compositional and Material Properties of Rat Bone after  
Drug Treatment**

by

**Yuchin Wu**

A thesis submitted to the Faculty of Graduate Studies and Research  
in partial fulfillment of the requirements for the degree of

**Doctor of Philosophy**

**Medical Sciences – Biomedical Engineering**

©Yuchin Wu

Fall 2013

Edmonton, Alberta

Permission is hereby granted to the University of Alberta Libraries to reproduce single copies of this thesis and to lend or sell such copies for private, scholarly or scientific research purposes only. Where the thesis is converted to, or otherwise made available in digital form, the University of Alberta will advise potential users of the thesis of these terms.

The author reserves all other publications and other rights in association with the copyright in the thesis and, except as herein before provided, neither the thesis nor any substantial portion thereof may be printed or otherwise reproduced in any material form whatsoever without the author's prior written permission.

To my beloved Mom  
Wu, Lifong

## **Abstract**

Various X-ray imaging modalities, such as planar X-ray films, dual energy X-ray absorptiometry and computed tomography have been utilized to estimate bone strength for osteoporotic subjects. However, emerging cases of spontaneous femoral shaft fracture in osteoporotic patients after years of bisphosphonate (BP) medication and controversial gains in bone mineral density (BMD) after medication with strontium ranelate (SrR) have questioned the reliance of X-ray based imaging for accurately assessing fracture risk. Therefore, assessments of bone strength must further account for the influence of bone microarchitecture, changes in elemental composition and material properties of bone following potent drug interventions. Accordingly, in this thesis, the hypothesis was that osteoporotic bone would be influenced by alterations in bone microarchitecture, elemental composition and corresponding material properties following drug treatment, which in the aggregate, affect bone strength.

In order to investigate the elemental composition and material properties, electron probe micro analysis and nanoindentation tests were applied to bone samples following SrR and/or BP treatment. The results confirmed that elemental strontium (Sr) was incorporated into bone predominantly in regions of new bone formation, through either the bone remodelling process or by incorporation during appositional and elongating bone growth. The material properties of bone were maintained following high dose strontium treatment, however, bone hardness was degraded following BP treatment. To measure bone strength, a simplified finite element analysis was established to calculate bone strength. Those analyses indicated that the strength of bone was positively related to the structural

parameters of bone volume/tissue volume, BMD and fractal dimension. To further explore the controversial increase in BMD following Sr drug therapy, a series of known solution standards for Sr and calcium (Ca) were evaluated using micro-computed tomography (Micro-CT). Our results proved that for every 1 mole% increase in Sr/(Sr+Ca), there was a corresponding 6.4% increase in BMD using X-ray based Micro-CT.

In summary, both elemental composition and material properties of rat bone were substantially altered following three months treatment with BP and/or SrR. Those alterations affected bone strength and microarchitecture, and the incorporation of Sr resulted in the bias of elevated BMD using X-ray based imaging modalities.

## **Acknowledgement**

I would like to express my gratefulness to my supervisor, Dr. Michael Doschak, for his advice on the research, his patience in reading my writings and for his support of my admission to the program.

I also wish to thank my labmates and anyone who may have helped me during the completion of this work. Without you, I would not have been able to reach success here. My special thanks to Dr. Samer Adeeb and Dr. John Duke who served as my committee members and gave me support with specialized research resources. Furthermore, my deep appreciation to Dr. Sergei Matveev who helped me with the experiments for elemental compositions and Dr. David Munoz-Paniagua who shared with me the nanoindentation techniques. Regarding the skills I learned in the bio-lab, I do appreciate my lab colleague Biwen Xu, who helped me to start the bio-lab work and refine the experimental process.

In addition, I also thank the funding support I obtained through the Alberta Osteoarthritis Team Grant and Queen Elizabeth II Graduate Scholarship.

Lastly, I am grateful to my friends, parents, my best brother and my love for their love and support of my decisions.

## Table of Contents

---

<b>CHAPTER 1 INTRODUCTION.....</b>	<b>1</b>
1.1. SCOPE OF DISSERTATION.....	2
1.2. HYPOTHESES, OBJECTIVES, AND EXPERIMENTS .....	6
1.2.1. HYPOTHESES .....	6
1.2.2. OBJECTIVES.....	6
1.2.3. EXPERIMENTS .....	7
1.3. REFERENCES .....	7
<b>CHAPTER 2 MEASUREMENT OF BONE COMPOSITION AND MATERIAL PROPERTY.....</b>	<b>1</b>
2.1. ELECTRON PROBE MICRO ANALYSIS (EPMA).....	2
2.2. NANOINDENTATION TEST.....	19
2.3. REFERENCES .....	25
<b>CHAPTER 3 COMPOSITIONAL AND MATERIAL PROPERTIES OF RAT BONE AFTER BISPHOSPHONATE AND/OR STRONTIUM RANELATE DRUG TREATMENT ...</b>	<b>30</b>
3.1. ABSTRACT.....	31
3.2. INTRODUCTION.....	32
3.3. MATERIALS AND METHODS.....	34
3.4. RESULTS.....	40
3.5. DISCUSSION.....	48
3.6. REFERENCES .....	55
<b>CHAPTER 4 A SIMPLE METHOD FOR THE FINITE ELEMENT ANALYSIS OF BONE STIFFNESS FROM MICRO- CT DERIVED BONE MICROARCHITECTURE FOR THE NON-ENGINEER - A CASE STUDY ON OSTEOPOROSIS RAT BONE</b>	<b>60</b>
4.1. ABSTRACT.....	61
4.2. INTRODUCTION.....	63
4.3. MATERIALS AND METHODS.....	65
4.4. RESULTS.....	72

4.5. DISCUSSION.....	79
4.6. CONCLUSION .....	84
4.7. REFERENCES .....	85

**CHAPTER 5 STRONTIUM DRUG TREATMENT IN OSTEOPOROSIS RESULTS IN THE BIAS OF BONE MINERAL DENSITY BY X-RAY IMAGING..... 90**

5.1. ABSTRACT.....	91
5.2. INTRODUCTION.....	92
5.3. MATERIALS AND METHODS.....	96
5.4. RESULTS.....	101
5.5. DISCUSSION.....	108
5.6. CONCLUSION .....	110
5.7. REFERENCES .....	110

**CHAPTER 6 MATERIAL PROPERTIES AND ELEMENTAL COMPOSITION OF RAT BONE IN CORRELATION WITH BONE STRENGTH AFTER TREATMENT WITH RISEDRONATE OR STRONTIUM RANELATE..... 113**

6.1. ABSTRACT.....	114
6.2. INTRODUCTION.....	116
6.3. MATERIALS AND METHODS.....	119
6.4. RESULTS.....	127
6.5. DISCUSSION.....	137
6.6. CONCLUSION .....	142
6.7. REFERENCES .....	143

**CHAPTER 7 GENERAL DISCUSSION AND CONCLUSION  
148**

7.1. DISCUSSION.....	149
7.1.1. THE EFFECTS OF SRR ON BONE.....	149
7.1.2. LIMITATION OF THIS RESEARCH.....	154
7.2. CONCLUSION .....	155
7.3. FUTURE DIRECTION.....	157
7.4. REFERENCES .....	157

## **List of Tables**

---

Table 2-1 Nanoindentation settings and calculations. ....	24
Table 3-1 Data of Micro-CT, EPMA, nanoindentation and mechanical test.....	42
Table 4-1 Definitions of structural parameters of trabecular bone. ....	65
Table 4-2 3D structure parameters of rat lumbar vertebrae calculated from Micro- CT images.....	74
Table 4-3 3D structural parameters & stiffness index of the 4/10 length L4. ....	79
Table 5-1 Sample list of Sr-Ca solutions (Note: 200-1:10 % of B at equivalent minerals to BMD 200g/cm <sup>3</sup> and so on.) .....	98

## List of Figures

---

Figure 2-1 Transverse and coronal directions of vertebrae. ....	5
Figure 2-2 Areas for EPMA qualitative analysis (upper panel) and locations for signal quantification (lower panel). ....	9
Figure 2-3 BSE images (Left) and WDS Sr maps (Right) of the transverse plane of vertebrae. White arrows point Sr accumulation. Warmer color means higher concentration. ....	10
Figure 2-4 Sr Maps on the coronal plane of L4 vertebrae. White arrows point Sr accumulation. Warmer color means higher concentration.....	12
Figure 2-5 P and Ca maps on the transverse plane of vertebrae. Warmer color means higher concentration. ....	13
Figure 2-6 Atomic ratios of P:Ca (left) and P:(Ca+Sr) (right) at EDGE and CENTER. ....	14
Figure 2-7 Atomic ratios of P:(Ca+Sr) from the edge of cortical bone toward vertebral center (200 $\mu$ m).....	15
Figure 2-8 Sr wt%: EDGE vs. CENTER (left) and measurement at the cortical bone from the edge toward vertebral center (0~200 $\mu$ m) (right). ....	15
Figure 2-9 Locations of rat vertebrae for nanoindentation tests. ....	22
Figure 3-1 (a) 3D Micro-CT render of rat L4 vertebral bone, sectioned in the coronal plane. The ventral block was examined by EPMA, with the spatially registered dorsal block used for nanoindentation. (b) Regions of vertebral bone that underwent sequential nanoindentation (line of white dots), either with incorporated strontium (EDGE), or without (CENTER). The light-blue color indicates EPMA detection of elemental strontium. (c). Photomicrograph of triangular nanoindentations (Berkovich tip) on rat vertebral bone surface (Zeiss Axio CSM 700, 100x objective). ....	37
Figure 3-2 Force (P) – Displacement (h) curve of nanoindentation tests. ....	40
Figure 3-3 Upper panel: Cross-sectional images of Micro-CT in the coronal plane of L4 vertebral bodies. Lower panel: 3 dimensional renders of trabecular bone from a rectangular region of interest. ....	43

Figure 3-4 Electron probe micro analysis (EPMA) maps of calcium distribution. (Anterior-Posterior view of half of the vertebral body). Warmer colors indicate higher concentrations of elemental calcium. ....	46
Figure 3-5 Depth (nm) vs. Load ( $\mu\text{N}$ ) curves from nanoindentation tests of different groups. a) Curves from indenting on EDGE. OVX-RIS shows a trend towards higher contact depth under the same indenting condition. b) Curves from indenting on CENTER. There were no apparent differences in contact depth between the treatments in the CENTER region of older, non remodelling bone. ....	47
Figure 3-6 The breaking energy of rat vertebrae L5, L6 tested under load (in compression) to failure. ....	48
Figure 4-1 Draw a VOI of a trabecular bone cylinder at rat vertebrae. ....	69
Figure 4-2 Steps for calculating stiffness of the trabecular bone cylinder of rat vertebra. ....	70
Figure 4-3 Calculations of the index of stiffness ( $k/k'$ ). ....	71
Figure 4-4 3D Micro-CT structure parameter graphs comparing OP-Sham to OP-OVX-Vehicle. Only parameters which showed significant differences ( $p < 0.05$ ) were graphed. ....	76
Figure 4-5 2D structural parameters, BV/TV(%), Tb.Pf(1/mm), FD, Tb.Sp(mm), BMD( $\text{g}/\text{cm}^3$ ), of the cylinder trabecular bone along the longitudinal axis from the caudal to cranial direction. X-axis was normalized by the height of each vertebral body (trabecular cylinder). (x axis: Caudal to Cranial; 0 to 1) ....	77
Figure 4-6 Difference (absolute value) of 2D Micro-CT parameters between OP-Sham and OP-OVX- Vehicle. The maximum difference of Tb.Sp is in the middle of the vertebra. All other curves show the minimum difference in the middle right of the vertebral body. (x axis: Caudal to Cranial; 0 to 1) ....	78
Figure 4-7 Normalized stiffness index ( $k/k'$ ) of the trabecular cylinder of L4 vertebra. The values are significantly different ( $p < 0.05$ ). ....	78

Figure 5-1 BMD of HA and Sr-HA phantoms by (a) Micro-CT and (b) DXA. (HA 250: hydroxyapatite with true BMD of 250mg/cm <sup>3</sup> and so on.) Comparing Sr-HA to HA of the same true BMD, the multiples of BMD are close (1.39~1.56).....	102
Figure 5-2 BMD and BV/TV of femur and tibia by micro-CT imaging. (a) Sham vs. OVX-highSrR and (b) Sham-lowSrR vs. OVX-highSrR. (*p<0.05, the value is significant to OVX-highSrR.) The trends of BV/TV and BMD are different between groups. This indicates the bias of BMD resulting from strontium.....	103
Figure 5-3 (Sr/Sr+Ca)% in (a) femur and tibia and (b) toenails of rats. (*p<0.05, the value is significant to others.) .....	104
Figure 5-4 (a) Nominal BMD vs. (Sr/Sr+Ca)% of Sr-CA solutions (No difference was found by scanning under different X-ray energies). (b) The regression curve of the curve slopes in (a) and BMDs of Ca-solutions ((Sr/Sr+Ca)%=0).....	106
Figure 5-5 Adjusted BMD & BV/TV% of femur and tibia by Micro-CT imaging. (a) Sham vs. OVX-highSrR and (b) Sham-lowSrR vs. OVX-highSrR (*: p< 0.05, the value is significant to OVX-highSrR.) .....	106
Figure 5-6 Bone mineral content (BMC) measured by different methods, measuring ash weight, DXA, and Micro-CT. All three methods showed identical trends between groups.....	107
Figure 5-7 (a) BMC and (b) BMD measure by DXA before and after adjustment. (*p< 0.05, the value is significant to others.).....	108
Figure 6-1 The arrangement of animals and bone samples for experiments. ....	121
Figure 6-2 Longitudinal changes in structural parameters of vertebral column by Micro-CT along timecourse. The x-axis indicates the months after drug treatment. (1: Sham-lowSrR; 2: OVX-lowSrR; 3: OVX-highSrR; 4: OVX-lowSrR+RIS. Statistics result, e.g. “1-23” means 1 is significantly different from 2 and 3 while comparing results at the same time point.).....	130

Figure 6-3 Morphological changes of bone architecture of rats in different groups. Longitudinal direction, 0, 1, 2, 3, indicates the month after drug treatments. ....	131
Figure 6-4 Changes in structural parameters of vertebral column by Micro-CT at the endpoint. (Significantly different from <sup>a</sup> Sham-lowSrR; <sup>b</sup> OVX-lowSrR; <sup>c</sup> OVX-highSrR; <sup>d</sup> OVX-lowSrR+RIS) .....	132
Figure 6-5 The distributions of elemental strontium in vertebra L5 (sagittal plane) in rats by EPMA after drug treatment for three months. Warmer color indicates higher concentrations of Sr. White arrows identify locations with Sr deposition. ....	135
Figure 6-6 Distributions of elements in OVX-highSrR: (a) at the vertebra L4-the wt% of Ca, Sr and P along the line from the edge to the center of the cortical bone by EPMA. The concentration of Sr decreased from the edge (~ 2.0%) to the center. (b) at the proximal femur by synchrotron imaging. Colors show the distribution of Sr. ....	136
Figure 6-7 Material properties a) Young's Modulus (GPa) and b) Hardness (GPa) at Center and Edge regions of bone by nanoindentation tests at the endpoint. (Significantly different from <sup>a</sup> Sham-lowSrR; <sup>b</sup> OVX-lowSrR; <sup>c</sup> OVX-highSrR; <sup>d</sup> OVX-lowSrR+RIS).....	136
Figure 6-8 Stiffness of vertebral column in rats by finite element analysis at the endpoint. (Significantly different from <sup>a</sup> Sham-lowSrR; <sup>b</sup> OVX-lowSrR; <sup>c</sup> OVX-highSrR; <sup>d</sup> OVX-lowSrR+RIS).....	137

## List of Symbols, Nomenclature, or Abbreviations

---

2D	two dimensional
3D	three dimensional
A(hc)	projected area of contact area at contact depth hc
BMC	bone mineral content
BMD	bone mineral density
BMP	bitmap
BP	bisphosphonate
BPs	bisphosphonates
BSAP	bone-specific alkaline phosphatase
BSE	back-scattered electron
BV	bone volume
BV/TV	bone volume/tissue volume
Conn.Dn	connectivity density
CT	computed tomography
Ct.Ar	cortical bone area
Ct.Th	cortical bone thickness
DA	degree of anisotropy
DXA	dual energy X-ray analysis
E	Young's modulus
EDS	energy dispersive spectroscopy
ELISA	enzyme-linked immunosorbent assay
EPMA	electron probe micro analysis
Er	reduced modulus
F	force
FD	fractal dimension
FEA	finite element analysis
FWHM	full width at half maximum
H	hardness
H(t)	indenting depth
HA	hydroxyapatite
Hc	contact depth
HV	Vickers hardness
ICP-MS	inductively coupled plasma mass spectrometry
k	stiffness
k'	theoretical stiffness
Micro-CT	micro-computed tomography
OP	osteoporosis
OVX	ovariectomized
PAP	Pouchou & Pichoir
PBS	phosphate buffered saline
PIXE	proton/particle excited X-ray emission analysis
PTH	parathyroid hormone
qBSE	quantitative back-scattered electrons
QoL	quality of life

RIS	risedronate
ROI	region of interest
S	slope of the unloading curve by nanoindentation test
SD	standard deviation
SOTI	spinal osteoporosis therapeutic intervention
Sr-HA	strontium-hydroxyapatite
SrR	strontium ranelate
Tb.Th	trabecular thickness
Tb.N	trabecular number
Tb.Pf	trabecular bone pattern factor
Tb.Sp	trabecular separation
TMD	tissue mineral density
TROPOS	treatment of peripheral osteoporosis study
Tt.Ar	total cross-sectional area
TV	tissue volume
WDS	wavelength dispersive spectroscopy
XRF	X-ray fluorescence
ZAF	atomic number(Z), absorption(A), fluorescence(F) correction
$\nu$	Poisson's ratio

# **Chapter 1**

## **Introduction**

## 1.1. Scope of Dissertation

The research in this dissertation examined the influence of bone elemental composition in addition to bone mineral density (BMD) and their relation to bone strength after drug treatments for osteoporosis (OP). The origin of this research can be traced back to an appreciation of the bone remodelling process under the influence of drug medications. Throughout the lifetime of human beings, bone undergoes a balanced process of focal resorption and formation to maintain its structural microarchitecture, strength and mineral balance. However, the balance of bone remodelling can be disrupted by aging and disease that may result in a weakened bone structure, particularly when resorption is more active than formation.

One such bone condition is osteoporosis, which is associated with a high risk of fracture, morbidity and mortality [Johnell and Kanis 2006]. 2010 healthcare costs associated with osteoporosis in Canada have been calculated to be \$2.3 billion [Tarride et al. 2012]. That economic burden has been a world-wide concern with an estimated 200 million people diagnosed with osteoporosis in the year 2000 [Reginster and Burlet 2006]. Not surprisingly, substantial research efforts have been directed at strategies for improving BMD and reducing the associated risk of fracture in affected individuals.

To date, drug treatments have been focused on reversing that imbalance, by either inhibiting the resorption of bone (e.g., the bisphosphonate (BP) drugs) or by increasing bone formation (e.g. parathyroid hormone and strontium drugs). The effects of such drugs on bone volume and microarchitecture can be readily

measured using X-ray based imaging modalities, such as dual energy x-ray absorptiometry (DXA) and high resolution computed tomography, such as clinical peripheral quantitative computed tomography (pQCT) or laboratory based micro-computed tomography (Micro-CT). However, besides influencing bone volume and microarchitecture, drug therapy may result in the ingredients of the drug itself becoming deposited in bone, or change the structural composition of the bone tissue. Among current OP drugs, strontium ranelate (SrR; Protos®) serves as a prime example, as the chemical properties of strontium (Sr) are similar to those of calcium (Ca), which is the main element of bone in the crystal of hydroxyapatite (HA;  $\text{Ca}_{10}(\text{PO}_4)_6(\text{OH})_2$ ). Thus, in this dissertation, the elemental composition of bone after SrR and/or BP drug therapy was determined to gauge the subsequent effects on material properties and the X-ray evaluation of bone in an established rat model of OP. The OP that occurred was secondary to ovariectomy surgery (an established animal model of OP), as that induced high bone turn over and subsequent bone loss, which mimicked the human post-menopausal condition [(Kharode et al. 2008)]. In summary, this thesis is the first to provide a complete package for exploring elemental compositions (electron probe micro analysis (EPMA), material properties (nanoindentation), microarchitecture (Micro-CT) and stiffness (finite element analysis (FEA)) of bone, to gauge the effects of OP pathogenesis and the response to subsequent drug therapy. Although at a preliminary stage, the experimental methods developed in this research are robust and capable of evaluating drug effects upon bone strength in animals, where it is possible to access bony tissues post-mortem. However, This will lay the

foundation for the development of indirect or direct evaluation techniques for use in the clinic with human patients. In **Chapter 1**, the scope of this dissertation is introduced briefly, in order to outline the research globally as well as to define the purpose of each individual project. The hypothesis, methods and objectives of this research are described as the basis for subsequent experimental research. In **Chapter 2**, details of experimental methods, nanoindentation testing and EPMA evaluations are described. These tools are used for measuring the degree and impact of elemental composition and material changes in bone after drug therapy. The remaining chapters of this thesis are arranged as follows:

Experimentation developed for testing the hypothesis of elemental deposition and its influence on the material property of OP bone are presented in **Chapter 3**. A pilot study is completed in a rat model of OP using SrR and/or risedronate (RIS) drug treatments. A complete package of methods for exploring elemental compositions (EPMA), material properties (nanoindentation), microarchitecture (Micro-CT) and bone strength (mechanical testing) are devised and applied. The results also show clear evidence of the deposition of elemental Sr in bone after SrR treatment.

With respect to the bone microarchitecture, quantitative Micro-CT results provide evidence of effective antiresorptive drug treatment and conservation of trabecular bone volume. However, the direct relationship of those structural parameters to bone strength has limitations. In order to determine the correlation to bone strength, in **Chapter 4**, the most relevant structural parameters of Micro-CT are evaluated in rat trabecular bone, with and without the influence of OP. The

stiffness of vertebral trabeculae is calculated using FEA. Subsequently, bone stiffness is correlated to each structural parameter to assist with an interpretation of their influence upon bone strength. This investigation results in the development of a simple FEA process from Micro-CT images to calculate bone strength.

Since it is proven that elemental Sr became incorporated in bone after SrR therapy in Chapter 3, it is feasible that elemental Sr may attenuate the incident X-ray radiation more greatly than Ca during X-ray imaging procedures. This may bias the results of BMD obtained from drug treated patients using DXA or computed tomography based imaging. Therefore, in **Chapter 5**, the potential Sr bias upon BMD measurements under Micro-CT and DXA are presented. Besides rat bone samples, a series of Sr solutions are also evaluated as phantoms for calibrating the BMD of Sr-dosed bone. An equation relating between Sr mole% and BMD is developed to correct the BMD bias of Sr containing bone.

To capitalize upon the findings and defined experimental methods for exploring elemental composition and material properties of bone in previous chapters, the integration of those techniques is applied to a large cohort size of animal number in **Chapter 6**. The project is designed to explore the effects of material properties on bone strength after treatment of SrR and RIS for osteoporotic rats. This topic is of particular relevance with the increasing emergence of spontaneous femoral shaft fracture after long-term BP drug treatment.

In conclusion, **Chapter 7** summarizes the concept and results of each project. The discussions are focused on the results of drug effects on bone and describing the limitations of the methods employed. Moreover, the future directions of this study are also addressed.

## 1.2. Hypotheses, Objectives, and Experiments

### 1.2.1. Hypotheses

The general hypothesis is that BP and/or Sr drug treatments in a rat model of osteoporosis will alter the microarchitecture and elemental composition of bone, thereby influencing the material properties of bone and ultimately, the strength of that bone. Additionally, it is hypothesized that the deposition of elemental Sr in bone resulted in an increased BMD bias under X-ray imaging compared to the normal bone.

### 1.2.2. Objectives

The general objectives of this research are to:

- 1) measure the composition of bone in terms of the distribution and concentration of inorganic Ca, Sr, and P
- 2) determine the respective BMD and bone microarchitecture, and their correlation to bone strength
- 3) measure elemental Sr in bone after drug therapy and determine the degree of BMD bias under X-ray imaging
- 4) measure the material behaviour of rat bone and correlate those parameters with the measured inorganic composition

- 5) combine measures of material properties and bone microarchitecture to enable the accurate prediction of bone strength in cohorts of drug-dosed rat bones, after BP and/or SrR drug treatments

### 1.2.3. Experiments

To achieve the research objectives, the following experimental techniques were utilized in this dissertation:

- 1) Dual-energy X-ray absorptiometry (DXA) (Chapter 5)
- 2) Enzyme-linked immunosorbent assay (ELISA) (Chapter 6)
- 3) Electron probe micro analysis (EPMA) (Chapter 2,3,6)
- 4) Finite element analysis (FEA) (Chapter 6)
- 5) Inductively coupled plasma mass spectrometry (ICP-MS) (Chapter 5,6)
- 6) Mechanical compression test (Chapter 3)
- 7) Micro-computed tomography (Micro-CT) imaging (Chapter 3,4,5,6)
- 8) Nanoindentation (Chapter 2,3,6)
- 9) Synchrotron k-edge subtraction (KES) Micro-CT imaging (Chapter 6)

### 1.3. References

Johnell O, Kanis JA. 2006. An estimate of the worldwide prevalence and disability associated with osteoporotic fractures. *Osteoporos Int.* 17(12):1726–1733.

Kharode YP, Sharp MC, Bodine PV. 2008. Utility of the ovariectomized rat as a model for human osteoporosis in drug discovery. *Methods Mol Biol.* 455:111-24

Reginster JY, Burlet N. 2006. Osteoporosis: a still increasing prevalence. *Bone.* 38(2 Suppl 1):S4-9.

Tarride JE, Hopkins RB, Leslie WD, Morin S, Adachi JD, Papaioannou A, Bessette L, Brown JP, Goeree R. 2012. The burden of illness of osteoporosis in Canada. *Osteoporos Int.* 23(11):2591-600.

## **Chapter 2**

# **Measurement of Bone Composition and Material Property**

## 2.1. Electron Probe Micro Analysis (EPMA)

EPMA which includes back-scattered electron (BSE) imaging, energy dispersive spectroscopy (EDS) and wavelength dispersive spectroscopy (WDS) has been commonly implemented in the geological sciences to assess elemental composition, but has not been widely used to date in the biological field – particularly the application of WDS. Therefore, in this section, the application of this technique for rat bone sample analysis was introduced from sample preparation to the collection of qualitative maps and quantitative data relative to specific elements.

As a methodology, EPMA can be traced back to the discovery of the cathode and vacuum tube (Crooks, 1875) to the first prototype of the EPMA instrument (Castaing, 1950). During that period, the discovery of X-ray (Röntgen, 1895), the atomic number related wavelength of X-ray emission (Moseley, 1913) and characteristic X-ray (Barkla, 1909) played key roles in the subsequent development of the principles of EPMA. Evaluations commenced using a focused beam of high energy electrons interacting with elemental atoms of a sample. Those interactions yielded characteristic X-ray emissions, consisting of ejected sub-atomic particles and photons. The concentration of any constituent element can thus be quantified by the number of electron counts that were converted from the emitting characteristic X-ray photons. The electron counts were calibrated against elemental standards in order to determine the concentrations of each element in the sample. The spatial resolution of such measurements was less than 5 $\mu$ m, which corresponded to the excitation volume in the respective beam-sample

interaction. Because of the importance of beam-sample interaction, the ideal sample should present with a flat, clean and non-porous surface. In addition, electrically non-conductive samples should be coated with a thinly sprayed film of conductive material (carbon) to avoid charging and beam deflection. Relating to those requirements for appropriate samples, bone meets most requirements at the  $\mu\text{m}$  scale – except for the criteria of non-porosity and homogeneity. In addition to sample preparation, the standards for the quantitative calibration should have similar elemental concentrations and densities to the unknown samples for accurate quantification. Regarding the operation of the instrument, there are two common methods for measuring the intensities of characteristic X-ray radiations in EPMA: EDS and WDS. In EDS, the radiation is measured using Li-doped silicon crystal. On the other hand, with WDS, X-ray intensities are measured with the help of specially designed analytical crystals, which are used to diffract characteristic radiations toward the X-ray detector. Because of the diffraction, this approach provides much higher spectral resolutions and sensitivities (i.e., precision). Therefore, WDS is preferred for quantitative measurements of trace elements ( $< 1 \text{ wt}\%$ ). However, by contrast, EDS is faster, more robust, and less expensive (i.e., generally available at most academic institutions).

With respect to quantitative measurement, the principles behind EDS, WDS and BSE images provide different resolutions in elemental detection. BSE images have been applied to assess Ca concentrations for more than a decade. The Ca concentration of HA samples was built in as a feature of most EDS systems as a reference for BSE images, to calibrate the concentration of Ca in bone. However,

the method of BSE was based on counting signals of back-scattered electrons. It was constrained by the premise that bone is comprised solely of HA and that subsequent measurements are directly proportional to Ca weight percent (wt%). As a result, BSE method did not work accurately for the measurement of other elements. In order to deal with that issue, an adjusted equation was developed to calibrate Sr concentrations using HA standards and BSE images since the atomic number of Sr ( $Z=38$ ) is higher than that of Ca ( $Z=20$ ) [Busse et al. 2010]. Nonetheless, when analyzing BSE images, the specific elements still can not be measured directly. EDS can measure the characteristic X-rays of specific elements, but it does not allow high spectral resolution and is only suitable for relatively high concentrations of elements ( $> 1$  wt%). In comparison, WDS offers higher spectral resolution than EDS and allows significantly higher measurement precision. However, EDS has its strengths, such as simple mechanical design, no X-ray focusing required, comparatively lower cost. To date, most quantitative analysis of the elemental composition of bone still relies on quantitative back-scattered electrons (qBSE) and EDS [Farlay et al. 2005; Sutton-Smith et al. 2008; Fratzi-Zelman et al. 2009a; Fratzi-Zelman et al. 2009b; Boivin et al. 2010; Busse et al. 2010; Hofstaetter et al. 2010; Misof et al. 2010; Roschger et al. 2010a; Roschger et al. 2010b]. For performing good spectral resolutions, WDS is preferred.

In the following sections, a case study was introduced to explain the application of EPMA with bone samples.

## **Animals**

Sixteen 6-month old females Sprague Dawley rats were ovariectomized (OVX) to mimic the osteoporosis occurred after menopause, and divided into 4 groups (n=4/group), OVX-Vehicle, OVX-RIS (risedronate treated), OVX-SrR (strontium ranelate [Protos®] treated), and OVX-RIS+SrR. Sham-operated rats were prepared as controls (Sham; n=3/group). The protocol pertaining to all procedures and aspects of the study was approved by the University of Alberta animal care and ethics committee. After 16 weeks of treatment (RIS 0.06 mg/kg q3.5d; SrR 308mg/kg qd po), all rats were euthanized and their lumbar vertebrae L3 and L4 were dissected. The muscle and soft tissues connected to vertebrae were cleaned manually. L3 vertebrae were cut using a precision sectioning saw (IsoMet® 1000, Buehler, Illinois U.S) along the transverse plane from the middle of the vertebral body. The upper halves were reserved for EPMA. L4 vertebrae were cut along the coronal plane from the middle of the vertebral body; the front halves were reserved for EPMA [Figure 2-1].

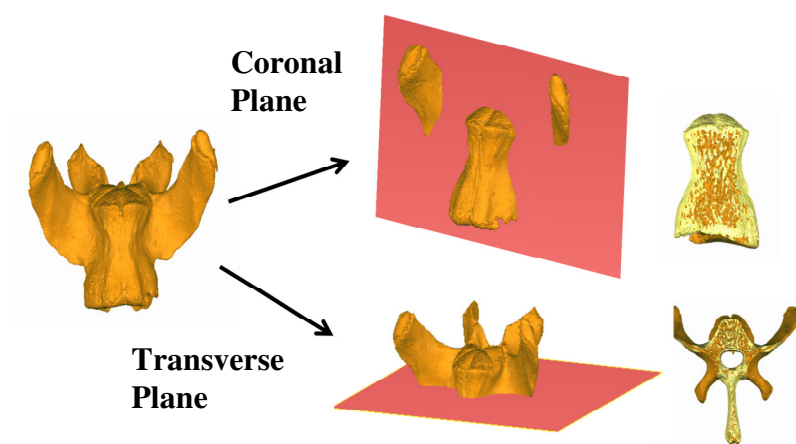


Figure 2-1 Transverse and coronal directions of vertebrae.

### **Sample Preparation, Qualitative Maps and Quantitative Data Collection**

The reserved vertebral bones were immersed in acetone separately in 15mL Falcon<sup>®</sup> tubes for 4 weeks to dehydrate and defat the bone samples. In the first week, the acetone solution was changed every day. After 4 weeks, the bones were removed from the acetone solution and dried in an oven at 40°C for 24 hours. Each dehydrated bone sample was embedded in a 1-inch diameter cylinder (Sampl-Kup<sup>®</sup>, Buehler, Illinois U.S) epoxy (Epo-Thin<sup>®</sup>, Buehler, Illinois U.S). The surface for analysis was faced down when casting the samples. To ensure the infiltration of epoxy into all the empty spaces of bone, a vacuum system (Cast N' Vac, Buehler, Illinois U.S) with -6 bar pressure was used during the casting process. Samples were left at 25°C overnight to ensure proper curing. Once the resin was fully set, it was expected to have the standard hardness (Shore D 85) for polishing. If the resin was not hard enough, the debris may infiltrate into the resin during polishing. Furthermore, soft resin may burst under the high vacuum environment during electron probe analysis. After the impregnation, the samples were cut, grounded and polished progressively to 0.5µm fineness (Thin Section Laboratory, Department of Earth and Atmospheric Sciences, University of Alberta, Canada). In order to ensure electrical conductivity of the polished surface, samples were coated with a 20-30nm thick carbon film.

A CAMECA SX100 electron probe microanalyzer (CAMECA, Paris FR), located at the Department of Earth and Atmospheric Sciences, University of Alberta (Edmonton, Canada) was used to acquire X-ray intensity maps and BSE images as well as for qualitative analysis. The instrument was equipped with 5

WDS spectrometers, EDS, secondary electron and BSE detectors. For qualitative elemental maps and quantitative analysis, the WDS spectrometers were tuned to measure the individual peak intensities of the following X-ray lines: Ca  $K\alpha$  (LPET crystal), P  $K\alpha$  (LPET crystal), Sr  $L\alpha$  (LTAP crystal). Those elements were selected to reflect the composition of HA in bone and of Sr after treatment with SrR. Additionally, the following mineral standards were used to refine spectrometer peak positions and for sample quantitative analysis: strontianite ( $SrCO_3$ ) for Sr; F-Apatite ( $Ca_5(PO_4)_3F$ ) for P; and dolomite ( $CaMg(CO_3)_2$ ) for Ca. The scanning area of the rat vertebra was determined relevant to known regions of bone turnover in osteoporotic bone. Since OP is a systematic disease and the vertebral geometry is relatively symmetric in the sagittal plane, only half of the sample surface was selected for elemental maps to minimize the significant expense associated with EPMA generation of qualitative elemental maps. For qualitative maps, the electron beam accelerating voltage was set to 15keV with the current of 15nA for coronal sections and 30nA for transverse sections. The moving step of the electron beam was 2  $\mu m$  with a dwell time of 20 ms/pixel. For quantitative analysis, the setting of the electron beam was 15keV, 10nA and 5  $\mu m$  between steps, and the dwell times were 20 seconds at the peaks and 10 seconds on each background. In addition to the peak intensities, background signals on each side of the peak were measured. PAP correction [Pouchou, Pichoir 1985] was implemented. The post-processing of signals was done using the vendor supplied software, PeakSight 4.1 (CAMECA, Paris FR).

Preliminary scans clearly demonstrated Sr deposition in these regions: 1) the areas close to growth plates; 2) the periosteal surfaces of cortical bone; 3) the endosteal surfaces of trabeculae and cortical bone. Measurements were taken on the Sr-rich exterior envelope of cortical bone (50 $\mu$ m from the edge of cortical bone; designated "EDGE") and Sr-poor middle areas of cortical bone (200 $\mu$ m from the edge of cortical bone; designated "CENTER"). Five points were measured on each region. Those values were subsequently averaged to represent the concentration for these 2 areas. In order to understand the elemental distribution along the deposition sequence, 10 points were quantitatively analyzed along a 200 $\mu$ m traverse from the edge of cortical bone toward the center of the vertebral body [Figure 2-2].

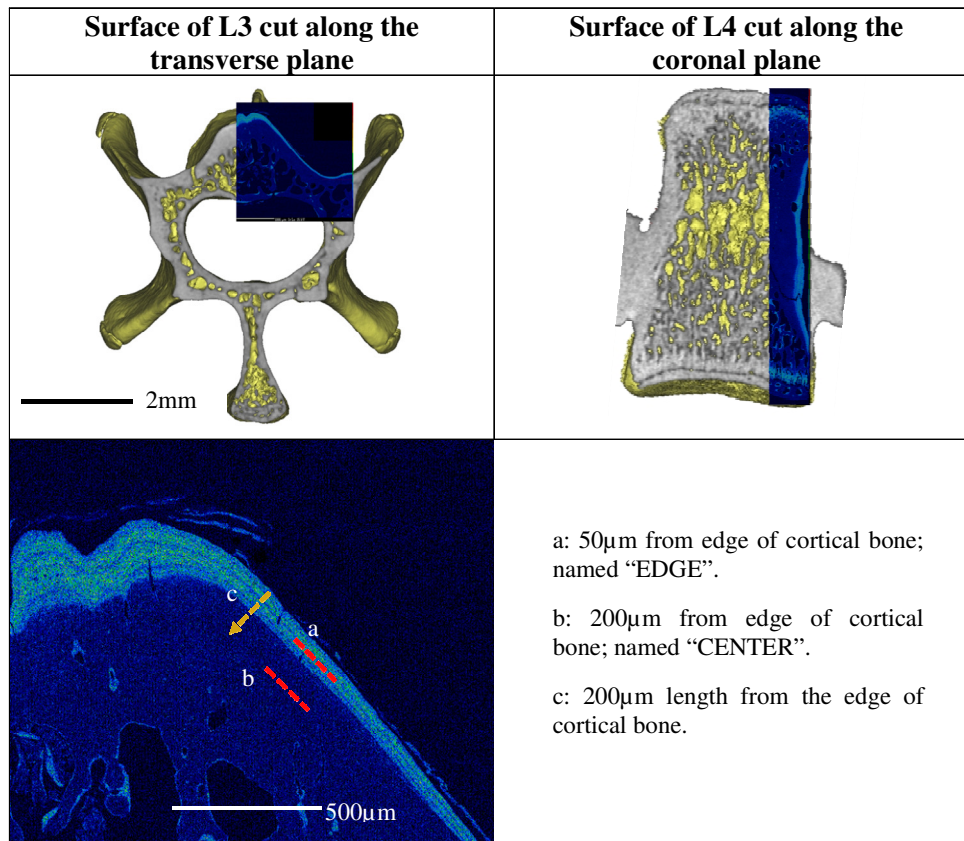


Figure 2-2 Areas for EPMA qualitative analysis (upper panel) and locations for signal quantification (lower panel).

## Results Analysis

### *BSE images*

From the results, significant differences in contrast were not seen between images [Figure 2-3]. Theoretically, the intensity of BSE signal is a function of the average atomic number of the scanned area [Skedros et al. 1993]. The heavier matrix areas should present brighter than lighter matrix areas in homogeneous samples. However, this was not observed in our inhomogeneous bone samples. The natural density variation of the bone may overprint the effect of Sr concentration on the image. Thus, the contrast of BSE images did not only reflect compositional variation in bone. The compositional analysis of BSE images

should be used with extreme caution [Busse et al. 2010], since the differences of gray scale values on the BSE images were difficult to be interpreted in terms of Sr or Ca depositions.

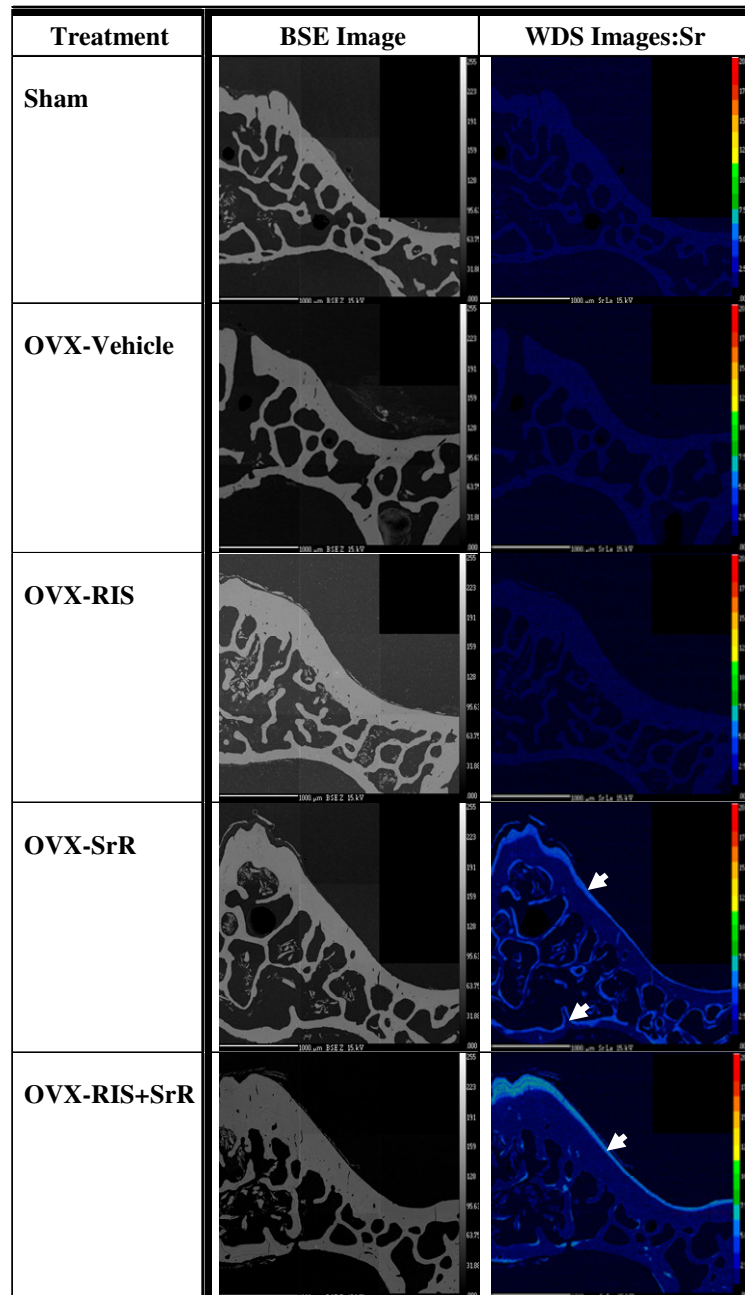


Figure 2-3 BSE images (Left) and WDS Sr maps (Right) of the transverse plane of vertebrae. White arrows point Sr accumulation. Warmer color means higher concentration.

*WDS results - elemental distributions*

In both Sr treatment groups, OVX-SrR & OVX-RIS+SrR, Sr was accumulated in higher concentrations ( $\sim 2.20 \pm 0.05$  wt%) in areas near growth plates, free surfaces of cortical and trabeculae bone [Figure 2-3]. Sr depositions formed a 50~200 $\mu$ m ring wrapping exterior cortical bone (named “EDGE”). Comparatively, smaller thickness (20~50 $\mu$ m) of Sr was founded on trabecular surfaces. Further comparing the Sr depositions on trabeculae between OVX-RIS+SrR and OVX-SrR, the former treatment group showed much fewer Sr depositions on trabecular surfaces than the latter one. The distribution of high concentrations of Sr proved that Sr was incorporated into bone through three different mineralization ways: 1) Sr element was brought to areas near growth plates during the elongation growth; 2) Appositional growth offered opportunities for Sr to deposit on the exterior surfaces of cortical bone; 3) Sr also deposited during bone remodelling on the free surfaces of trabeculae [Figure 2-4]. A review of the images of the various treatments showed that P and Ca were distributed relatively evenly [Figure 2-5]. Generally, the concentration of P accompanied with the concentrations of Ca in a ratio of  $\sim 0.6$  in SrR-free groups.

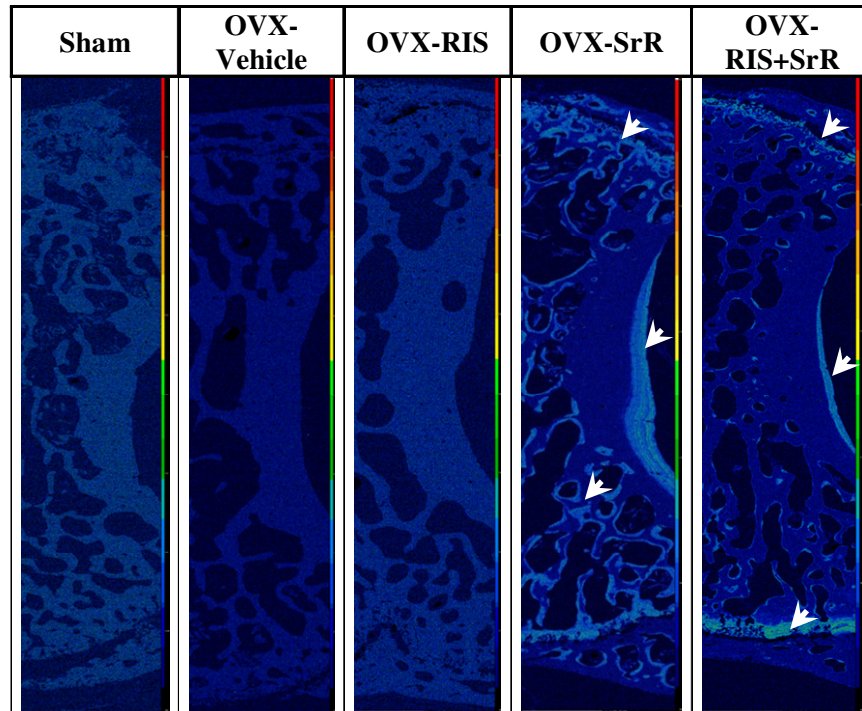


Figure 2-4 Sr Maps on the coronal plane of L4 vertebrae. White arrows point Sr accumulation. Warmer color means higher concentration.

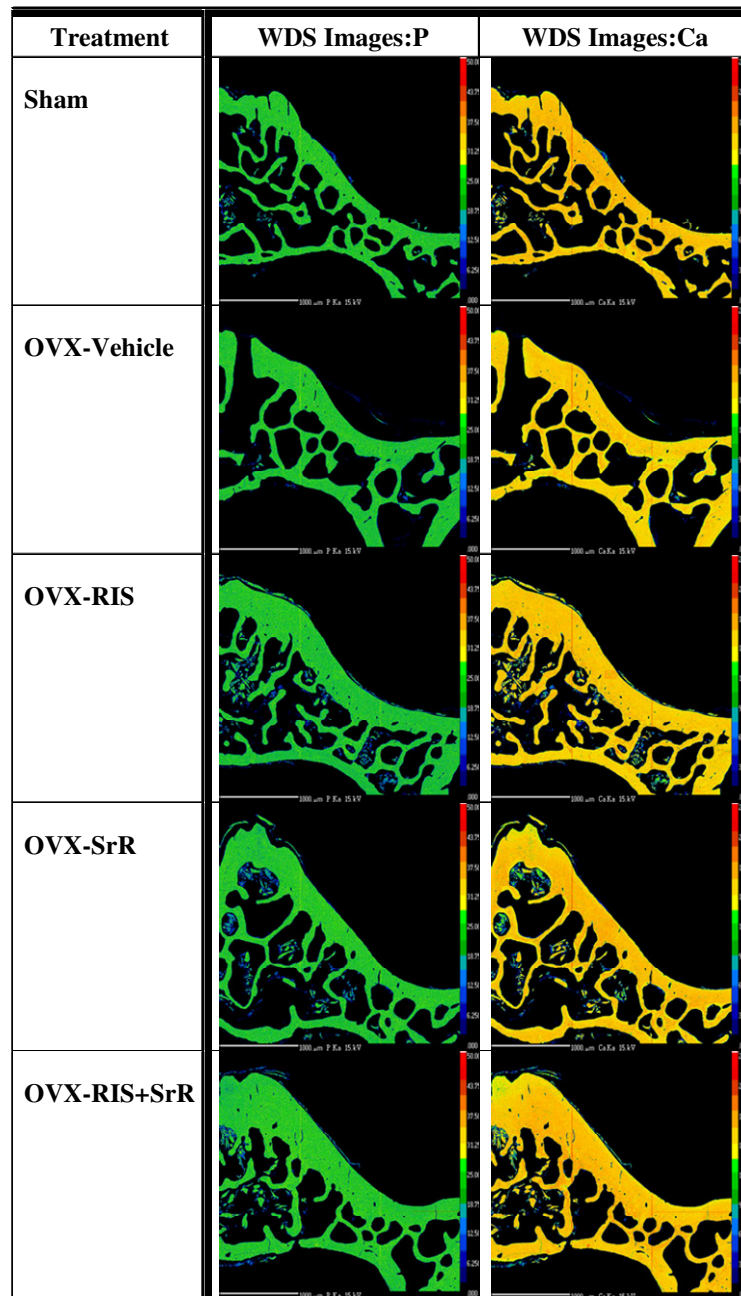


Figure 2-5 P and Ca maps on the transverse plane of vertebrae. Warmer color means higher concentration.

#### *WDS results – quantitative elemental analysis*

In both the transverse and coronal plane of bone samples, atomic ratios of P/Ca and P/(Ca+Sr) were higher (~0.05) at the EDGE of the cortical bone in SrR treatment groups than other groups [Figure 2-6]. Relatively, the values of P/Ca were stable in the SrR-free groups. This indicated that SrR changed the

mineralization both qualitatively and quantitatively. In both SrR treatment groups, the quantitative data showed the values of P/Ca and P/(Ca+Sr) decreased with the position moving towards the center of the bone. The value of P/(Ca+Sr) approached normal (0.6) as the bone became old [Figure 2-7]. The OVX-RIS group did not show significant difference in P/Ca in comparison to Sham and OVX-Vehicle groups. No significant differences in P/(Ca+Sr) and Sr wt% were found between OVX-SrR and OVX-RIS+SrR treatments. This indicated that combining the treatment of RIS and SrR did not show synergistic effects in the deposition wt% of Ca and Sr.

In addition to those regions mentioned above, a  $\sim 0.12 \pm 0.02$  wt% of Sr [Figure 2-8] was observed in CENTER bone areas, which were supposed to have no new bone formation after SrR treatment. This indicated that Sr was incorporated into bone crystals not only through the mechanism of bone formation but also other mechanisms, such as secondary mineralization. This information is a new discovery which has not been presented in other publications [Busse et al. 2010; Li et al. 2010].

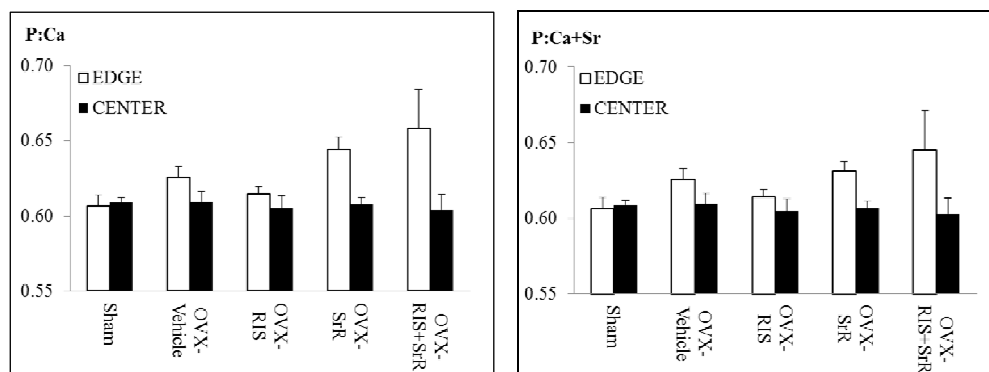


Figure 2-6 Atomic ratios of P:Ca (left) and P:(Ca+Sr) (right) at EDGE and CENTER.

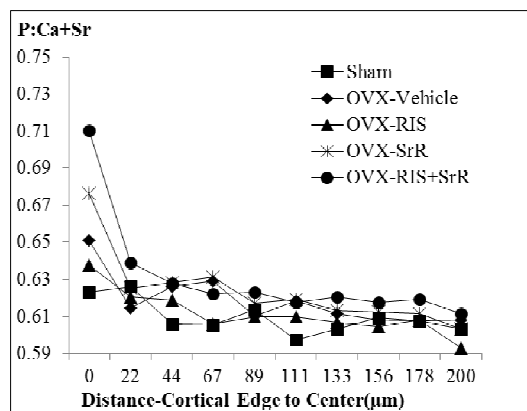


Figure 2-7 Atomic ratios of P:(Ca+Sr) from the edge of cortical bone toward vertebral center (200µm).

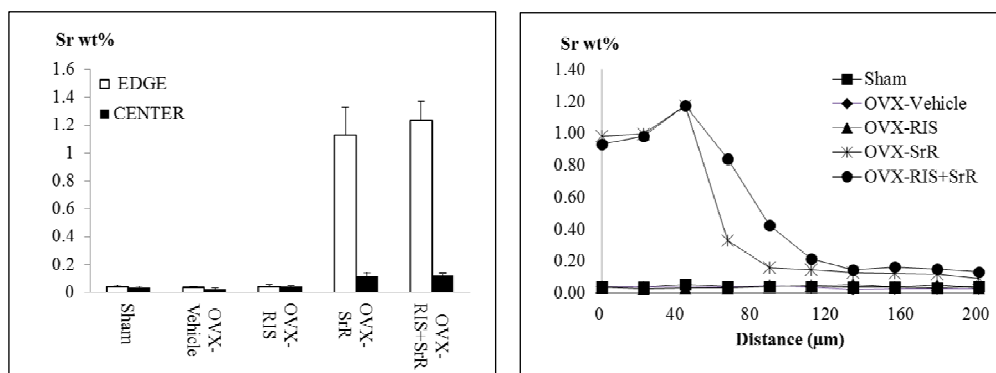


Figure 2-8 Sr wt%: EDGE vs. CENTER (left) and measurement at the cortical bone from the edge toward vertebral center (0~200µm) (right).

## Discussion

In practical experiments, there are both systematic and random errors. Some of them may be critical, especially mistakes in quantifying elements with small concentrations. Those problems for studying bone samples were discussed below.

### *Porosity and heterogeneity of bone*

When performing quantitative analyses, the idealized standards should contain approximate amount wt% of elements as the samples, and both standards and samples should be non-porous and homogeneous. Unfortunately, porosity and heterogeneity are characteristics of bone. Charges may accumulate in the pores of the samples and then interfere with the scattering of electrons and absorption of

X-ray energies. The matrix correction (ZAF) usually overcompensated for heterogeneous materials. Our quantification standard, F-Apatite-PP ( $\text{Ca}_5(\text{PO}_4)_3\text{F}$ ), of Ca and P had slightly higher wt% of P and Ca (P wt%=17.84%, Ca wt%=38.74%) as compared with the general bone. The standard, strontianite-EPS3 ( $\text{SrCO}_3$ ), used for Sr quantification contained 57.22 wt% of Sr. This concentration was much higher than the typical concentration in bones analyzed (1.2 wt% in average). Although the standards used were not ideal, the quantitative results were still comparable among groups. The discussions of Mg were ignored here, because the data for Mg was measured constant over all groups and values were minor.

#### *Surface roughness and tilt*

Roughness and tilt of sample surfaces were reflected with improper sample preparation. If the sample surface was tilted, the signals may reflect as gradual changing in color. This may be misinterpreted as a change in concentrations.

#### *Detection Limit and Standard Deviation*

Since determination of the wt% of Sr was essential in this study, the detection limits and standard deviations of raw data were important for knowing actual elemental concentrations. Under the settings of 95% confidence interval, and a 20-second count time, the detection limit for each element was as follows: 0.028 wt% (P), 0.024 wt% (Ca), 0.052 wt% (Sr) and 0.020 wt% (Mg). The standard deviations were 0.300 wt% (P), 0.290 wt% (Ca), 0.049 wt% (Sr) and 0.042 wt% (Mg).

#### *Other approaches for assessing elemental composition*

By analyzing the BSE images in this study, no specific elemental distribution can be deduced from the gray scales. However, BSE images have been applied for references for Ca concentrations in the literature. This is based on the principle that the fraction of beam electrons backscattered from a sample is proportional to the average atomic number ( $Z$ ) of the regional scanned volume. Higher  $Z$  on regional volume results in fewer electrons penetrating the sample and producing more backscattering electrons. This method needed levels of synthetic HA standards as references, and was only available for measuring Ca [Sutton-Smith et al. 2008; Fratzl-Zelman et al. 2009a; Hofstaetter et al. 2010; Misof et al. 2010; Roschger et al. 2010a]. Based on the levels of synthetic HA, an adjusting equation was developed to relate BSE intensities to Sr concentrations [Busse et al. 2010].

The other tool for determining elemental composition is EDS. It is more common and cheaper than WDS for elemental detections. However, EDS is not good as WDS in spectral resolution. Farlay et al (2005) applied EDS with 15keV and a 100-second count time to detect Sr  $L\alpha$ , P  $K\alpha$ , Ca  $K\alpha$  [Farlay et al. 2005; Boivin et al. 2010]. The count time was much longer than the, 20~40 seconds, used for WDS in this study. For our WDS system (CAMECA SX100), the full width at half maximum (FWHM) of energy resolution was 12.45eV for Sr, 2.39eV for P and 11.60eV for Ca. These values were one tenth compared to the spectral resolution of EDS.

#### *The accuracy of quantitative results*

As to the problem of the lower total weight percent of our samples, the accuracy of each quantification method should be discussed. Although the

principle of WDS offered higher spectral resolutions, most published researches focused on EDS and qBSE methods to measure wt% of Ca. The qBSE method provided only Ca concentration and Sr concentration with multiplication to an atomic number correction equation. For normal bone, qBSE results showed the concentration of Ca  $\approx$  21 wt% [Busse et al. 2010]. By normalizing the total detection elements (i.e. P, Ca, Mg, O and Na) to 100 wt%, the wt% of Ca was  $\approx$  33 & 38, and P was  $\approx$ 14% [Farlay et al. 2005; Boivin et al. 2010]. The ratio of wt% P/Ca was  $\approx$ 0.37~0.42. The difference was apparent between the results of qBSE and EDS. Theoretically, the overall composition of bone consists of 60 wt% of inorganic material (e.g. HA), 8~10 wt% of water and 30~32 wt% of organic materials (e.g. Type I collagen, non-collagen and cells) [Kanis et al. 1994]. The samples prepared for EPMA in this study were dehydrated, so only had 90~92 wt% of fresh bone left. According to the information listed above, wt% of Ca and P in our EPMA samples could be calculated by the following equation (e.g. wt% of Ca = inorganic matter in bone (%) x dehydrated bone (%) x theoretical Ca wt% of HA).

$$\text{Ca wt\%} = 60\% \div (90\% \sim 92\%) \times 39.82\% = 25.97\% \sim 26.52\% \approx \mathbf{26.25\%}$$

$$\text{P wt\%} = 60\% \div (90\% \sim 92\%) \times 18.46\% = 12.03\% \sim 12.29\% \approx \mathbf{12.16\%}$$

From the calculations, the theoretical wt% of Ca and P in normal bone should be around 26 and 12 with the ratio of wt% P/Ca  $\approx$  0.46. Comparing the theoretical values with the WDS results in this study, WDS results were very convincing (Ca (29.20 wt%), P (13.75 wt%); wt% of P/Ca =0.47), although there were only 70~80 wt% in total elements. Coats et al (2003) applied WDS on osteoarthritis

and OP patients; the measured wt% of Ca was approximately 27 and elements in total were around 80 [Coats et al. 2003]. The data were similar to the results of this study. In summary, the wt% results by EPMA were reasonable without normalization, although the total percentage of elements was not equal to 100%.

## 2.2. Nanoindentation Test

The nanoindentation test was chosen to measure the material property in this study, due to the irregular shape and small testing area (in the scale of  $\mu\text{m}$ ) of the rat bone.

In the literature, researchers have investigated the material properties of normal, fractured and drug treated OP bone by various testing methods, such as nano and micro indentations. In the analysis of normal rat bones, newly formed tissue (0-4 days) was 84% less stiff and had 79% lower mineral to matrix ratio than older intracortical (15-70 days) tissue [Donnelly et al. 2010]. Regarding differences between fractured and non-fractured OP bone, no differences in Young's modulus (E) or hardness (H) were found [Fratzl-Zelman et al. 2009a]. Studies of OP bone were categorized as those with and without drug treatments. The tests on rat vertebrae of OVX (H:0.91 $\pm$ 0.13GPa, E:21.01 $\pm$ 2.48GPa) and sham (H:0.90 $\pm$ 0.09GPa, E:22.03 $\pm$ 2.44GPa) groups without drug treatments showed no significant difference in hardness and Young's modulus [Guo and Goldstein 2000; Jämsä et al. 2002]. However, there was evidence of changes in material properties after drug treatment. The bone in the OVX treated group showed a reduced modulus compared to the normal groups after 12 months but not after 31 months [Brennan et al. 2011]. Significantly higher hardness measurements by

nanoindentation tests were found in the vertebrae of BP treated OP beagle dogs than in the vehicle group [Wang et al. 2008]. On the subject of SrR treatment, the nano-mechanical property (reduced modulus,  $E_r$ ) of the transiliac bone was not compromised when experimenting on OP women [Ammann et al. 2007; Roschger et al. 2010]. SrR dosed normal rats showed that no difference in modulus was found in dry bone on the trabecular level. Nevertheless, under physiological conditions, the SrR dosed rat bone increased 15% in modulus and 11.1% in hardness [Ammann et al. 2007]. Besides nanoindentation tests, Vickers hardness (HV) from micro-indentations was also commonly applied for testing bone materials. Osteoporotic patients had lower HV than people without OP. The hardness was correlated positively with the degree of mineralization of bone [Boivin et al. 2008]. From the above studies, the results of elastic modulus and hardness of bone in normal, OVX, and BP or SrR treatment were not consistent among publications. There were several possible explanations for these discrepancies. Since bone was heterogeneous and anisotropic in nature, the means of nano-mechanical properties did not represent the actual properties locally. On the other hand, the method for calculating E and H by nanoindentation tests was based on the assumption that the testing material was elastic-plastic. This method did not take into account the viscous properties of bone [Fan and Rho 2003; Oyen 2005]. According to the points listed above, the inconsistency of results was anticipated, especially if there was only a minor difference among groups.

The origin of calculating  $E_r$  and H from nanoindentation tests can be traced to Sneddon's theory for the elastic contact in 1965. A relation between the contact

depth and force was formulated [Sneddon 1965]. The differential of the force to contact depth was equal to the slope of the initial part of unloading curve from nanoindentation tests. This calculation was based on the assumption that the contact area between the tip and sample were constant for the initial unloading parts [Oliver et al. 1992]. For further analyzing the unloading curve, Oliver and Pharr developed an improved model from the Sneddon's model. This model provided a novel calculation to determine the slope and find the contact depth. The contact area at maximum loading can be calculated from the contact depth and the shape area function of the indenter [Pharr and Oliver 1992]. However, this method was ideal for elastic-plastic materials, and was improper to understand materials with viscous properties, such as bone. Additionally, the nanoindentation testing methods were developed for materials that are viscoelastic, and viscoelastic-plastic materials. Besides, most commercial instruments were equipped with the function of dynamic material analysis, which was designed for testing viscoelastic materials. Regarding the solutions for the viscos-elastic-plastic materials, several methods, such as cyclic loadings to eliminate viscos-plasticity and long dwell time to reduce viscosity, were developed [Fan and Rho 2003]. In this thesis, the general load-unload testing method was used for the nanoindentation test to investigate the elastic property of bone.

### **Sample Preparation**

The preparation of bone samples was referenced to the sample preparation of EPMA.

### **Testing Methods**

### *Define indenting locations*

The area in the 80 $\mu\text{m}$  distance from the exterior cortical edge toward the center of the bone was named EDGE, and the remaining cortical area was named CENTER. EDGE was supposed to be the newly formed bone region because of appositional growth. CENTER was the old bone region without obvious bone activities. The nanoindentation tests were performed at 20 $\mu\text{m}$  from the exterior edge of cortical bone (EDGE) and 100 $\mu\text{m}$  in the CENTER regions [Figure 2-9Error! Reference source not found.].

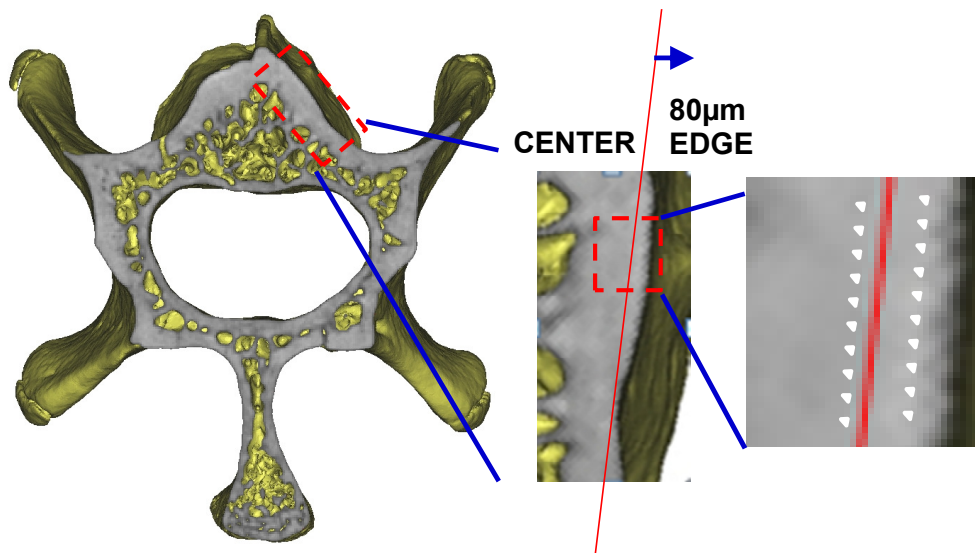


Figure 2-9 Locations of rat vertebrae for nanoindentation tests.

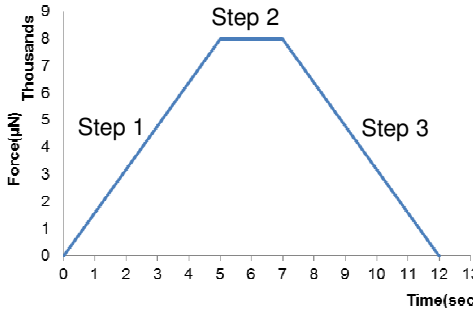
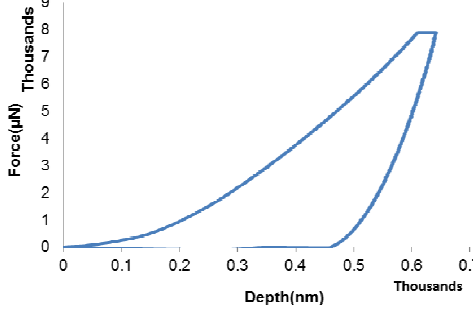
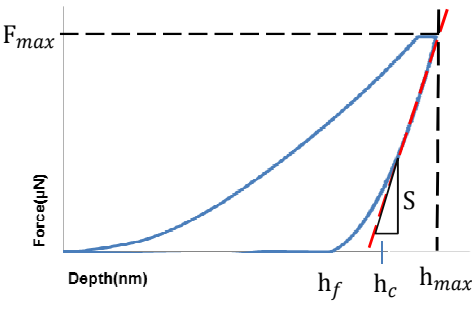
### *Settings*

Nanoindentation tests were performed using a TI 900 TriboIndenter (Hysitron Inc., Minneapolis MN). The Berkovich tip (100~200nm radius, Young's modulus = 1140GPa, Poisson's ratio=0.07) was selected as the indenter. The following preparations were done before tests: The distance between the stage and the tip was calibrated to ensure the accuracy of the indenting locations. For a new tip, tip

bashing was done by indenting on a fused quartz material for one thousand times to blunt the tip to a stable shape. The nano to micro scale indentions emphasized the significance of the machine compliance, even though the machine compliance was small. The machine compliance calibration was done by indenting on an aluminum sample to have higher indentation depths than indenting on quartz with a range of forces. Since the calculation of  $E_r$  and  $H$  depended on the projected contact area of the tip, the shape area function curve (contact depth vs. projected contact area) of the tip was measured by indenting on a quartz sample with a range of forces. The results of contact depth and projected contact area were fitted by a polynomial function. After getting correct shape area function, the machine compliance parameter could be corrected. The machine compliance test should be done every time if the sensor or tip was changed.

A 3-step testing method with three time sections, 5 seconds (loading)-2 seconds (hold)-5 seconds (unloading) and loading at maximum  $8000\mu\text{N}$ , was applied with the loading rate of  $1600\mu\text{N/s}$ . The indenting depth ( $h(t)$ ) and force ( $F$ ) were recorded. The material behaviour was interpreted as an elastic-plastic material. Based on this assumption, the loading section was assumed to show elasticity and plasticity; the unloading section was assumed to be pure elastic. The Oliver-Pharr method [Pharr and Oliver 1992] was applied to calculate the slope ( $S$ ). Reduced modulus ( $E_r$ ) and hardness ( $H$ ) were calculated from  $S$ , the shape area function of the tip ( $h_c$  vs.  $A(h_c)$ ) and contact depth ( $h_c$ ) [Table 2-1].

Table 2-1 Nanoindentation settings and calculations.

<p>Input Loading Curve (time vs. force)</p>	
<p>Output Curve (depth vs. force)</p>	
<p>Curve for Calculations</p>	
<p>Parameters</p>	<p><math>A(h_c)</math>: projected area of contact area between tip and specimen at <math>h_c</math>.</p> <p>The holding time is short. It's contribution in deformations will be ignored.</p>
<p>Equations (Black: input; Red: output)</p>	<p>CurvFit the unloading curve by equation <math>F = \alpha(h - h_f)^m</math></p> <p><math>S = \left(\frac{dF}{dh}\right)_{F_{max}}</math> ;</p> <p>If <math>\frac{h_f}{h} &lt; 0.7</math>, Then</p> <p><math>h_c = h_{max} - \frac{\epsilon}{S} F_{max}</math> ,</p> <p>(<math>\epsilon = 0.75</math>); for Berkovich tip</p>

### 2.3. References

- Ammann P, Badoud I, Barraud S, Dayer R, Rizzoli R. Sep 2007. Strontium ranelate treatment improves trabecular and cortical intrinsic bone tissue quality, a determinant of bone strength. *J Bone Miner Res*, 22(9):1419-1425
- Boivin G, Bala Y, Doublier A, Farlay D, Ste-Marie L G, Meunier P J, Delmas P D. Sep 2008. The role of mineralization and organic matrix in the microhardness of bone tissue from controls and osteoporotic patients. *Bone*, 43(3):532-538
- Boivin G, Farlay D, Khebbab MT, Jaurand X, Delmas PD, Meunier PJ. Apr 2010. In osteoporotic women treated with strontium ranelate, strontium is located in bone formed during treatment with a maintained degree of mineralization. *Osteoporos Int*, 21(4):667-677
- Brennan O, Kennedy OD, Lee TC, Rackard SM, O'Brien FJ, McNamara LM. Feb 2011. The effects of estrogen deficiency and bisphosphonate treatment on tissue mineralisation and stiffness in an ovine model of osteoporosis. *J Biomech*, 44(3):386-390
- Busse B, Jobke B, Hahn M, Priemel M, Niecke M, Seitz S, Zustin J, Semler J, Amling M. 2010. Effects of strontium ranelate administration on bisphosphonate-altered hydroxyapatite: Matrix incorporation of strontium is accompanied by changes in mineralization and microstructure. *Acta Biomaterialia*, 6(12):4513-4521
- Coats AM, Zioupos P, Aspden RM. 2003. Material properties of subchondral bone from patients with osteoporosis or osteoarthritis by microindentation

- testing and electron probe microanalysis. *Calcified Tissue International*, 73:66-71
- Donnelly E, Boskey AL, Baker SP, van der Meulen M CH. Mar 2010. Effects of tissue age on bone tissue material composition and nanomechanical properties in the rat cortex. *J Biomed Mater Res A*, 92(3):1048-1056
- Fan Z, Rho JY. Oct 2003. Effects of viscoelasticity and time-dependent plasticity on nanoindentation measurements of human cortical bone. *J Biomed Mater Res A*, 67(1):208-214
- Farlay D, Boivin G, Panczer G, Lalande A, Meunier P J, Sep 2005. Long-term strontium ranelate administration in monkeys preserves characteristics of bone mineral crystals and degree of mineralization of bone. *J Bone Miner Res*, 20(9):1569-1578
- Fratzl-Zelman N, Roschger P, Gourrier A, Weber M, Misof B, Loveridge N, Reeve J, Klaushofer K, Fratzl P. Sep 2009a. Combination of nanoindentation and quantitative backscattered electron imaging revealed altered bone material properties associated with femoral neck fragility. *Calcif Tissue Int*, 85:335-343
- Fratzl-Zelman N, Roschger P, Misof BM, Pfeffer S, Glorieux FH, Klaushofer K, Rauch F. 2009b. Normative data on mineralization density distribution in iliac bone biopsies of children, adolescents and young adults. *Bone*, 44(6):1043-1048

- Guo X, Goldstein SA. Mar 2000. Vertebral trabecular bone microscopic tissue elastic modulus and hardness do not change in ovariectomized rats. *J Orthop Res*, 18(2):333-336
- Hofstaetter JG, Roetzer KM, Krepler P, Nawrot-Wawrzyniak K, Schwarzbraun T, Klaushofer K, Roschger P. 2010. Altered bone matrix mineralization in a patient with Rett syndrome. *Bone*, 47(3):701-705
- Jämsä T, Rho JY, Fan Z, MacKay CA, Marks SC, Tuukkanen J. Feb 2002. Mechanical properties in long bones of rat osteopetrotic mutations. *J Biomech*, 35(2):161-165
- Kanis JA, Melton LJ, Christiansen C, Johnston CC, Khaltsev N. Aug 1994. The diagnosis of osteoporosis. *J Bone Miner Res*, 9(8):1137-1141
- Li C, Paris O, Siegel S, Roschger P, Paschalis EP, Klaushofer K, Fratzl P. May 2010. Strontium is incorporated into mineral crystals only in newly formed bone during strontium ranelate treatment. *J Bone Miner Res*, 25(5):968-975
- Misof BM, Paschalis EP, Blouin S, Fratzl-Zelman N, Klaushofer K, Roschger P. 2010. Effects of 1 year of daily teriparatide treatment on iliacal bone mineralization density distribution (BMDD) in postmenopausal osteoporotic women previously treated with alendronate or risedronate. *J Bone Miner Res*, 25(11):2297-2303
- Oliver WC, Pharr GM, Brotzen FR. 1992. On the generality of the relationship among contact stiffness, contact area, and elastic modulus during indentation. *J Mater Res*, 7:613-617

- Oyen ML. Ultrastructural characterization of time-dependent, inhomogeneous materials and tissues. Jun 2005. PhD thesis, University of Minnesota. Biophysical Sciences and Medical Physics
- Pharr GM, Oliver WC. 1992. An improved technique for determining hardness and elastic modulus using load and displacement sensing indentation experiments. *J Mater Res*, 7:1564-1583
- Pouchou JL, Pichoir F. 1985. "PAP"(phi-rho-z) procedure for improved quantitative microanalysis. In: Armstrong JT, editor. *Microbeam Analysis*. San Francisco Press: San Francisco, 104-106
- Roschger P, Lombardi A, Misof BM, Maier G, Fratzl-Zelman N, Fratzl P, Klaushofer K. 2010a. Mineralization density distribution of postmenopausal osteoporotic bone is restored to normal after long-term alendronate treatment: qBEI and sSAXS data from the fracture intervention trial long-term extension (FLEX). *J Bone Miner Res*, 25(1):48-55
- Roschger P, Manjubala I, Zoeger N, Meirer F, Simon R, Li C, Fratzl-Zelman N, Misof BM, Paschalis EP, Strelci C, Fratzl P, Klaushofer K. Apr 2010b. Bone material quality in transiliac bone biopsies of postmenopausal osteoporotic women after 3 years of strontium ranelate treatment. *J Bone Miner Res*, 25(4):891-900
- Skedros JG, Bloebaum RD, Bachus KN, Boyce TM, Constantz B. Jan 1993. Influence of mineral content and composition on graylevels in backscattered electron images of bone. *J Biomed Mater Res*, 27(1):57-64

- Sneddon IN. 1965. The relation between load and penetration in the axisymmetric boussinesq problem for a punch of arbitrary profile. *Int J Engng Sci*, 3(1):47-57
- Sutton-Smith P, Beard H, Fazzalari N. 2008. Quantitative backscattered electron imaging of bone in proximal femur fragility fracture and medical illness. *J Microsc*, 229(1):60-66
- Wang X, Allen MR, Burr DB, Lavernia EJ, Jeremić B, Fyhrie DP. Oct 2008. Identification of material parameters based on mohr-coulomb failure criterion for bisphosphonate treated canine vertebral cancellous bone. *Bone*, 43(4):775-780

## **Chapter 3**

# **Compositional and Material Properties of Rat Bone after Bisphosphonate and/or Strontium Ranelate Drug Treatment**

---

The contents of this chapter have been previously published: Yuchin Wu, Samer M. Adeeb, M. John Duke, David Munoz-Paniagua, Michael R. Doschak. 2013. J Pharm Pharmaceuti Sci, 16(1):52-64

### 3.1. Abstract

**Purpose:** We investigated elemental strontium and/or bisphosphonate (BP) drug incorporation upon the compositional and biomechanical properties of vertebral bone, in a rat model of osteoporosis secondary to ovariectomy.

**Methods:** Six month old female rats were ovariectomized (OVX) and divided into untreated OVX-Vehicle, OVX-RIS (risedronate bisphosphonate [BP] treated), OVX-SrR (strontium ranelate [Protos®] treated), combination OVX-RIS+SrR, and sham-operated controls. After 16 weeks of treatment, rats were euthanized and lumbar vertebrae were dissected. Micro-computed tomography (Micro-CT), electron probe micro analysis (EPMA), mechanical testing in compression and nanoindentation testing were then undertaken to evaluate bone morphometry, elemental composition, material properties and strength.

**Results:** Bone volume was significantly reduced in the OVX-Vehicle ( $133\pm 10\text{mm}^3$ ) compared with OVX-RIS ( $169\pm 22\text{mm}^3$ ), OVX-SrR ( $145\pm 2\text{mm}^3$ ), and OVX-RIS+SrR ( $172\pm 8\text{mm}^3$ ). EPMA mapped elemental Sr deposition to the periosteal surface of cortical bone (50-100 $\mu\text{m}$  thick), endosteal trabecular surfaces (20 $\mu\text{m}$  thick), as well as to both vertebral growth plates. The atomic ratios of (Ca+Sr)/P were significantly reduced with SrR treatment (2.4%-6.6%), indicating Sr incorporation into bone mineral. No significant differences were measured in vertebral bone reduced modulus by nanoindentation. Conversely, all BP-dosed groups had significantly increased structural bone strength.

**Conclusions:** Thus, we concluded that BP drugs dominated the conservation

of trabecular geometry and structural strength in osteoporotic rats, whereas Sr drugs likely influenced bone volume and material composition locally.

### 3.2. Introduction

Osteoporosis (OP) related fractures affect one third of postmenopausal women worldwide, with an estimated two million OP related fractures occurring annually in the United States alone [de Villiers 2009]. Fracture occurs when bone encounters a load of sufficient magnitude (and rate of loading) to exceed its mechanical strength. Currently, bone mineral density (BMD) measurements derived from dual-energy X-ray absorptiometry (DXA) are heavily relied upon in order to estimate bone strength for OP patients in the clinic. Using patient BMD to diagnose OP is based on the hypothesis that BMD is directly related to Young's modulus (the isotropic elastic material property) of bone, and Young's modulus is therefore used as an index of bone strength. However, as only 50-70% of fractures will be predicted based upon BMD measurements [Griffiths 2007], clearly BMD values from DXA do not serve as the sole indicator of bone strength, and other important descriptors of bone quality and health (such as microarchitecture and material strength) need to be established, accepted and factored into the patient assessment scheme.

Both bisphosphonate (BP) and strontium ranelate (SrR) drug regimens have been shown to reduce the incidence of bone fracture in OP patients in large multicenter clinical trials [Reginster et al. 2000; Meunier et al. 2004], and thus, both drugs are currently indicated in the treatment of OP worldwide [Hwang et al.

2008; Borgström et al. 2010; Hiligsmann et al. 2010]. BPs are known to conserve trabecular bone volume and microarchitecture, and therefore, bone strength. In contrast, SrR has attracted much attention due to claims of potential dual functionality, with reports of both antiresorptive and formative events in bone after treatment. Although BP drugs effectively blocked the resorption of bone, they were well known to interfere with the subsequent phase of coupled osteoblast activity, and reduce bone formation by up to 50% [Reszka and Rodan 2004; Iwata et al. 2006]. Conversely, studies suggested that SrR enhanced osteoblastic cell function in remodelling and new bone growth [Ammann et al. 2004; Bonnelye et al. 2008]. Subsequent clinical studies indicated that SrR taken over a 3-year period resulted in the heterogeneous distribution of Sr in bone, resulting in the preservation of the bone micro-structure at the tissue level – but not translating into increased stiffness, as measured by indentation modulus [Roschger et al. 2010]. Research has evaluated the effectiveness of SrR and BP treatments respectively over an extended period to determine the effect at both clinical and tissue mechanical level [Muscoso et al. 2004; Roschger et al. 2010]. However, there remains a lack of data about the chemical composition and material properties of bone tissue when those drugs are administered independently – or potentially in combination.

Hence, the purpose of our study was to: (1) map the distribution and concentration of elemental calcium, strontium, and phosphorus in bone (after BP and/or SrR drug treatments); (2) measure associated BMD and bone microarchitecture (by Micro-CT); (3) assess the material behavior of drug-dosed

bone (using nanoindentation); and (4) combine those measurements of bone material property and microarchitecture to assess the outcomes of drug treatments from cohorts of bones in a rat model of developing OP.

### 3.3. Materials and Methods

#### **Animals and Drug Treatments**

[For animals groups and treatment, please refer to Chapter 2, 2.1-Animals.](#)

The dosage corresponded to an established effective dose for preventing bone loss in this animal model as well as maintaining relevance to the dose currently used in BP treatment of OP in humans [Campbell et al. 2011]. The SrR was dosed at 308mg/kg once per day by oral gavage, in order to assure the minimum threshold concentration was achieved to show the potential antiresorptive properties of SrR [Marie et al. 1993; Bonnelye et al. 2008], while still trying to assess the SrR function at a concentration that could be regarded as clinically relevant for use in human patients [Fuchs et al. 2008].

In rats dosed with RIS+SrR combination therapy, RIS was dosed s.c. 2 hours before giving the oral SrR dose, to allow for RIS to bind bone before strontium entered the system. One 2g sachet of commercially available SrR (Servier Laboratories, France) was reconstituted with distilled water and mixed to ensure dissolution. The rats were weighed, and the calculated amount of stock solution was dosed daily by oral gavage using a gastric feeding needle. Those rats were fasted for two hours before and two hours after the dose to prevent any food

interaction with calcium and any other elements within the feed. After 16 weeks of treatment, the rats were euthanized, and the L4, L5 and L6 vertebral bones were dissected fresh and cleaned of soft tissues, wrapped with phosphate buffer saline (PBS) - dampened paper towel and stored frozen at -20°C for subsequent analyses.

### **Micro-CT Imaging**

Dissected L4, L5 and L6 vertebrae were scanned ex-vivo by Micro-CT (SkyScan 1076, Kontich BE) at 18µm resolution with 70kV, 100µA using a 1.0mm aluminum filter. Projected images of the samples were reconstructed using vendor supplied software (Nrecon 1.6.1.5, SkyScan NV, Kontich BE), with images oriented in an axial plane of section. A rectangular region of interest (ROI) which was relative to the size of the vertebral body was used to sample a standardized amount of trabecular bone in the vertebral body in order to conduct standard histomorphometric analyses. The dimension of ROIs varied with the size of the vertebral body. The vertebral body growth plates were utilized as anatomical landmarks in order to consistently segment and sample the same region of trabecular bone from all samples. Vendor morphometric software (CTAn 1.10.0.1, SkyScan, Kontich BE) was then used to analyze the trabecular bone volume (BV, mm<sup>3</sup>), fractal dimension (FD) [Chappard et al. 2001], trabecular thickness (Tb.Th, mm), trabecular separation (Tb.Sp, mm) and tissue mineral density (TMD, g/cm<sup>3</sup>) [Bouxsein et al. 2010] against the vendor-supplied bone phantoms of known mineral density (0.25g/cm<sup>3</sup> and 0.75g/cm<sup>3</sup>) in order to calibrate BMD values from Hounsfield units.

### **Electron Probe Micro Analysis (EPMA)**

All L4 vertebrae were bisected coronally [Figure 3-1] using an Isomet diamond wafer saw (Buehler Ltd., Lake Bluff IL) with the dorsal bone half reserved for subsequent nanoindentation testing. The ventral bone half was defatted in acetone for 2 weeks then dried in a 40°C oven and embedded in epoxy (Epo-Kwick<sup>®</sup>, Buehler Ltd., Lake Bluff IL).

For the sample preparations and experimental settings, please refer to Chapter 2, 2.1-Sample Preparation.

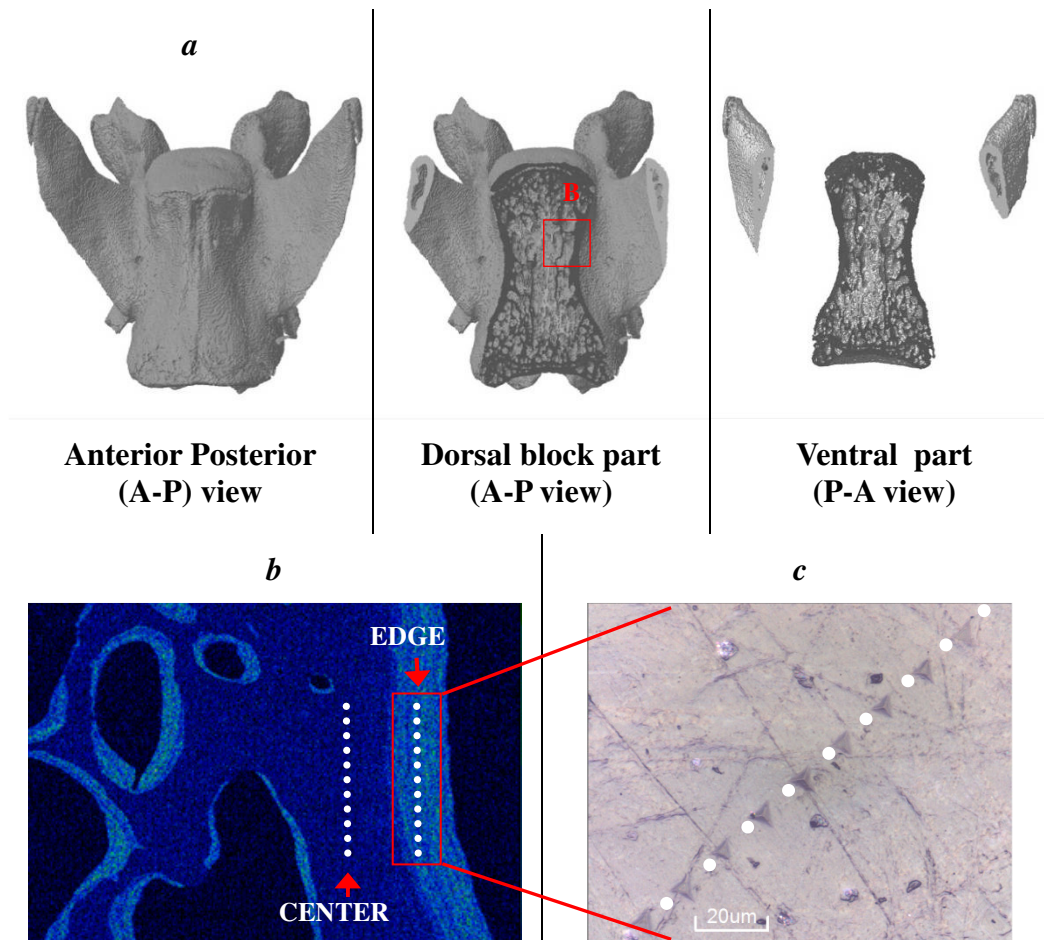


Figure 3-1 (a) 3D Micro-CT render of rat L4 vertebral bone, sectioned in the coronal plane. The ventral block was examined by EPMA, with the spatially registered dorsal block used for nanoindentation. (b) Regions of vertebral bone that underwent sequential nanoindentation (line of white dots), either with incorporated strontium (EDGE), or without (CENTER). The light-blue color indicates EPMA detection of elemental strontium. (c). Photomicrograph of triangular nanoindentations (Berkovich tip) on rat vertebral bone surface (Zeiss Axio CSM 700, 100x objective).

### Nanoindentation Testing

The dorsal vertebral bone half was secured with modelling clay to orient and support the cut surface parallel to the indenter crosshead. Samples were glued to 15mm diameter specimen metal disks and surfaces polished to a depth of 15µm

(0.05 $\mu$ m progressively) then cleaned with flowing distilled water under ultrasonic agitation.

[For the preparation of experiments and instrument, please refer to Chapter 2, 2.2.](#)

The Berkovich tip (100-200nm radius, with angle from perpendicular to face = 65.35°; diamond material with Young's modulus = 1141GPa, Poisson's ratio = 0.07) was used to make 10 indentations on regions with and without Sr [Figure 3-1 b, c]. Force control was 8000  $\mu$ N with 5 seconds of loading, 2 seconds holding and 5 seconds unloading. The reduced modulus ( $E_r$ ) and hardness ( $H$ ) of each indentation were calculated from the unloading displacement-force curve based on the Oliver and Pharr method [Fischer-Cripps 2004; Fischer-Cripps 2007].  $E_r$  and  $H$  were calculated from the displacement-force curve in [Figure 3-3].

[For calculations of  \$E\_r\$  and  \$H\$ , please refer to Chapter 2, 2.2.](#)

Indented bone regions were referred to the corresponding EPMA-derived elemental distribution maps, in order to compare the depth-force curves on regions of bone with (or without) Sr incorporation.

### **Mechanical Testing**

L5 and L6 vertebra were thawed at room temperature, trimmed of bony processes using the diamond wafer saw, with transverse cuts applied to both metaphyseal growth plates. An Instron 4443 materials testing device (Instron, Norwood USA) was used to test L5 and L6 vertebral body in axial compression

under displacement control at a speed of 2mm/min, to avoid the effect of crosshead impact on the sample prior to failure. Load cell capacity was  $\pm 1\text{kN}$  with displacement recorded according to the position of the crosshead in mm, both with a resolution of  $1\text{E-}5$ . Merlin™ Software and Series IX™ 8.0.7.0 vendor-supplied software (Instron, Norwood USA) were used to control testing and output the load deformation curve. Since the displacement-force curves were curved before, breaking energy (areas below the displacement-force curve) was more objective to represent physical properties of the bone than stiffness. It was then calculated to analyze the difference between treatment groups after BP and/or SrR treatments in the OVX rats.

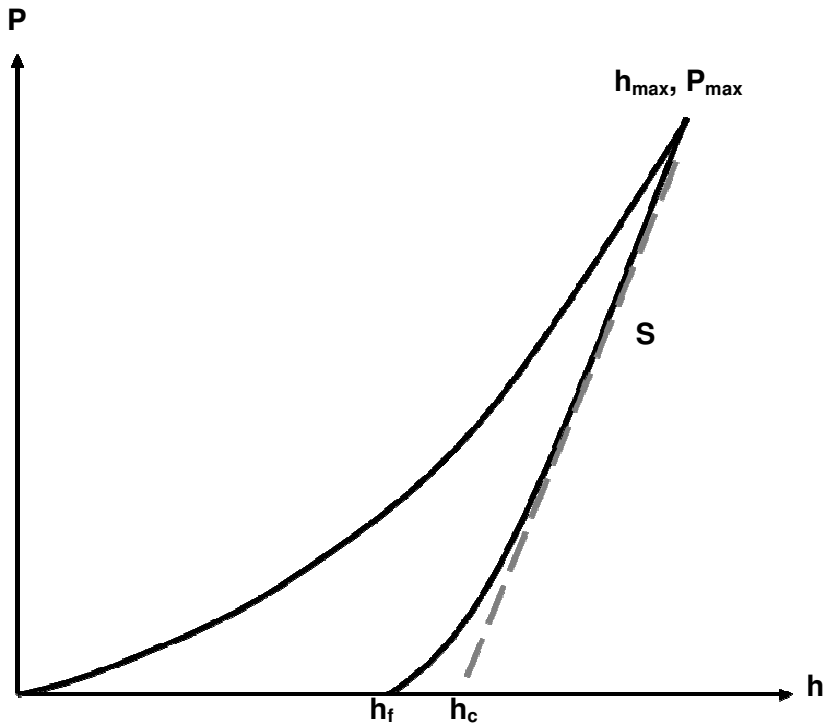


Figure 3-2 Force (P) – Displacement (h) curve of nanoindentation tests.

### Statistical Analysis

PASW<sup>®</sup> Statistics 17.0 was used for statistical evaluations. Due to the small sample numbers, non-parametric Kruskal-Wallis H test was used to compare differences amongst groups, with the Mann-Whitney U test used to compare between individual groups. An asymptotic value  $\leq 0.05$  was used to test for significant differences.

## 3.4. Results

### Structural Parameters from Micro-CT

All drug treatment groups were measured to have significantly greater trabecular BV compared to untreated OVX-Vehicle [Table 3-1]. The 3

dimensional FD values were increased in treatment groups where BV was also increased. However, we did not measure significant synergistic effects of BP+SrR treatments over the BP treatments individually, in either the BV or the FD values. According to the results of FD, SrR treatment increased the complexity of trabecular connectivity in OVX-SrR; however, the complexity was lower than for normal bone. Similarly, we did not measure significant differences in trabecular thickness (Tb.Th) or BMD between the different treatment groups. From the Micro-CT 3-D renders, we examined the trabeculae (FD, Tb.Sp) and the thickness of cortical bone among groups. It was evident that OVX-RIS and OVX-RIS+SrR dosed animals had significant conservation of trabecular bone volume 4 months after OVX surgery [Figure 3-3].

Table 3-1 Data of Micro-CT, EPMA, nanoindentation and mechanical test.

	Treatment				
	Sham	OVX-Vehicle	OVX-RIS	OVX-SrR	OVX-RIS+SrR
<b><i>Micro-CT parameters of the average of L4,L5,L6</i></b>					
BV (mm <sup>3</sup> )	153±11 <sup>b,e</sup>	133±10 <sup>a,c,d,e</sup>	169±22 <sup>b,d</sup>	145±2 <sup>b,c,e</sup>	172±8 <sup>a,b,d</sup>
TMD (g/cm <sup>3</sup> )	0.65±0.05	0.64±0.01	0.67±0.02	0.65±0.02	0.65±0.01
FD	2.48±0.04 <sup>b,d</sup>	2.36±0.03 <sup>a,c,e</sup>	2.53±0.03 <sup>b,d</sup>	2.41±0.02 <sup>a,c,e</sup>	2.54±0.02 <sup>b,d</sup>
Tb.Th (mm)	0.13±0.02	0.11±0.01	0.13±0.01	0.12±0.01	0.12±0.01
Tb.Sp (mm)	0.22±0.02 <sup>b,d</sup>	0.32±0.05 <sup>a,c,e</sup>	0.21±0.02 <sup>b,d</sup>	0.29±0.03 <sup>a,c,e</sup>	0.22±0.01 <sup>b,d</sup>
<b><i>EPMA atomic ratio of Sr,Ca and,P at Sr deposition region</i></b>					
(Sr+Ca)/P	1.65±0.01 <sup>d,e</sup>	1.65±0.01 <sup>d,e</sup>	1.66±0.01 <sup>d,e</sup>	1.61±0.02 <sup>a,b,c</sup>	1.54±0.10 <sup>a,b,c</sup>
Sr/P-HSr	0.00<0.00 <sup>d,e</sup>	0.00<0.00 <sup>d,e</sup>	0.00<0.00 <sup>d,e</sup>	0.03<0.00 <sup>a,b,c</sup>	0.03<±0.00 <sup>a,b,c</sup>
<b><i>Nanoindentation results of Reduced Modulus(Er) and Hardness(H)</i></b>					
Er(GPa)-EDGE	31.52±6.62	31.78±3.68	23.82±3.80	31.10±6.85	29.85±5.73
Er(GPa)-CENTER	33.02±2.90	32.63±3.53	30.55±5.45	36.28±2.10	33.78±1.26
H(GPa)-EDGE	1.57±0.56	1.62±0.39	1.20±0.38	1.48±0.14	1.52±0.31
H(GPa)-CENTER	1.62±0.17	1.61±0.14	1.42±0.47	1.96±0.34	1.73±0.14
<b><i>Mechanical Testing for Breaking Energy of L5,L6</i></b>					
Breaking Energy (mm-kN)	0.19±0.01	0.18±0.04	0.23±0.07	0.19±0.01	0.27±0.03

Data expressed as Mean±SD. <sup>a</sup>Significantly different from Sham. <sup>b</sup>Significantly different from OVX-Vehicle. <sup>c</sup>Significantly different from OVX-RIS. <sup>d</sup>Significantly different from OVX-SrR. <sup>e</sup>Significantly different from OVX-RIS+SrR.

Abbreviations: BV: bone volume; TMD: tissue mineral density; FD: fractal dimension; Tb.Th: trabecular thickness; Tb.Sp: trabecular separation.

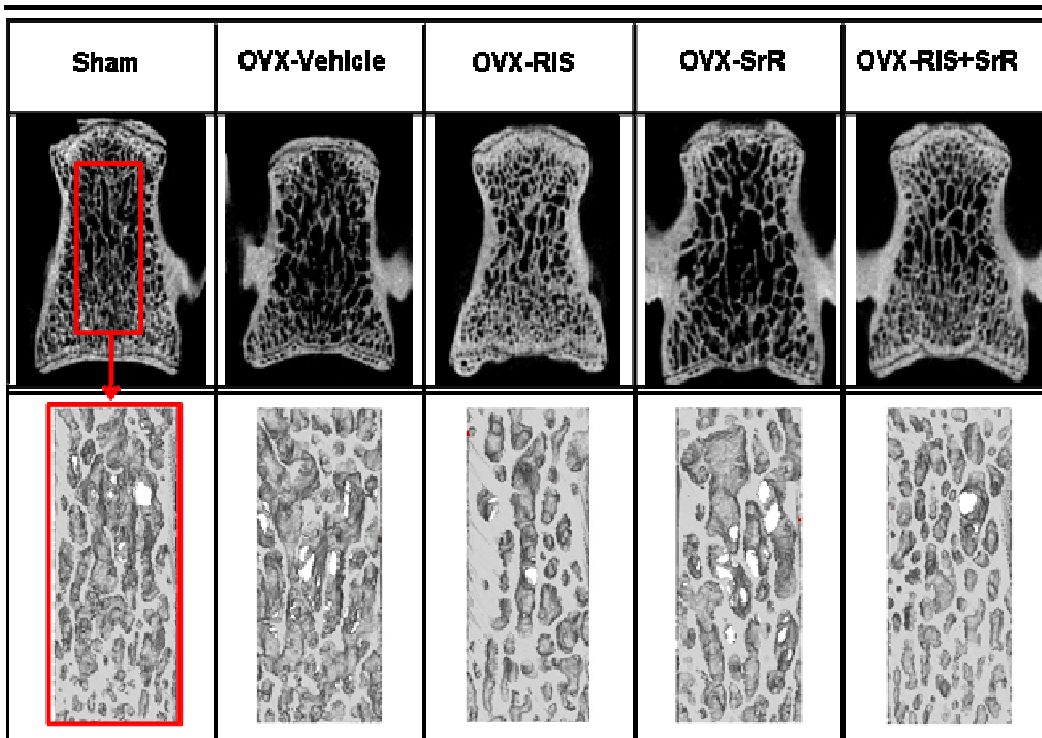


Figure 3-3 Upper panel: Cross-sectional images of Micro-CT in the coronal plane of L4 vertebral bodies. Lower panel: 3 dimensional renders of trabecular bone from a rectangular region of interest.

### **Sr, Ca, P Distributions and Atomic Ratio from EPMA**

From EPMA maps of different groups, we noted that Ca and P distributed evenly on the imaged surfaces [Figure 3-4]. Upon closer examination of individual trabeculae, we noted higher concentrations of Ca localized centrally in most trabeculae, with lower calcium concentrations localized as a thin layer on the exterior surfaces of both cortical and trabecular bone. Those observations suggested new bone formation events through appositional growth on the periosteal surface of cortical bone, and through remodelling on endosteal trabecular surfaces. Trabecular bone in proximity to the growth plate was also measured to have increased Ca concentration. Of particular significance was the dynamic localization of elemental Sr (using EPMA) to bone turnover in this

animal model of OP [Figure 2-4]. The periosteal cortical bone in both the OVX-SrR and OVX-RIS+SrR groups exhibited layers of Sr-enriched appositional bone growth in the order of 50-100 $\mu$ m over the 16 weeks period. Sr also deposited in trabecular bone distal to the growth plate (i.e., at the primary spongiosum). In EPMA maps of OVX-SrR, Sr incorporation encompassed individual trabeculae throughout the marrow cavity, to a depth of approximately 20 $\mu$ m. In stark contrast, Sr deposition was significantly reduced in the presence of the BP drug (i.e., in the OVX-RIS+SrR group), both in the number of formative events as well as in the depth of mineral deposition compared to SrR treatment alone. Quantitative analysis measured reduced wt% values in the OVX-RIS+SrR treated group for P<sub>2</sub>O<sub>5</sub>, CaO and SrO (48-80% of normal). In the Sr-free groups (i.e., Sham, OVX-Vehicle, OVX-RIS), no significant quantity of elemental Sr was measured. The Ca or Ca+Sr and P concentrations always maintained a consistent ratio. The atomic ratio (Ca/P or Ca+Sr/P) was 1.66 in all groups [Table 3-1]. The examined average wt% of Ca is 29% and 14% for P. There was no significant difference of the Ca/P ratio among non-Sr treatment groups. In both Sr treated groups (OVX-SrR and OVX-RIS+SrR), we measured 2.4%-6.6% lower atomic ratio of (Ca+Sr)/P in comparison with non-Sr groups. Accordingly, our data indicated that the wt% of Sr after 16 weeks of dosing with SrR (at the dosage employed) resulted in less than 2 wt% elemental Sr incorporation into the bone of the OVX-SrR and OVX-RIS+SrR groups.

### **Depth-Force Curves from Nanoindentation Tests**

Using nanoindentation, we did not measure any differences in reduced modulus or hardness after 16 weeks of drug treatment at the drug dosages employed in this study. We also compared force-displacement curves of nanoindentation on the areas shown by EPMA with and without Sr (EDGE/CENTER of cortical bone) [Figure 3-1 b] relative to each group. The curves showed there were no significant differences among groups in areas of CENTER cortical bone under the given indentation conditions. We noted a non-significant trend of OVX-RIS samples exhibiting increased contact depth under the standardized loading conditions compared to all other treatment groups [Figure 3-5].

### **Mechanical Testing**

In contrast to the nanoindentation, the breaking energy of the global vertebral body compression in L5 and L6 showed that both BP treated groups had increased structural bone strength compared with all other groups [Figure 3-6]. Both OVX-RIS and OVX-RIS+SrR dosed animals showed improved breaking energy compared to the other OVX groups (OVX-Vehicle and OVX -SrR).

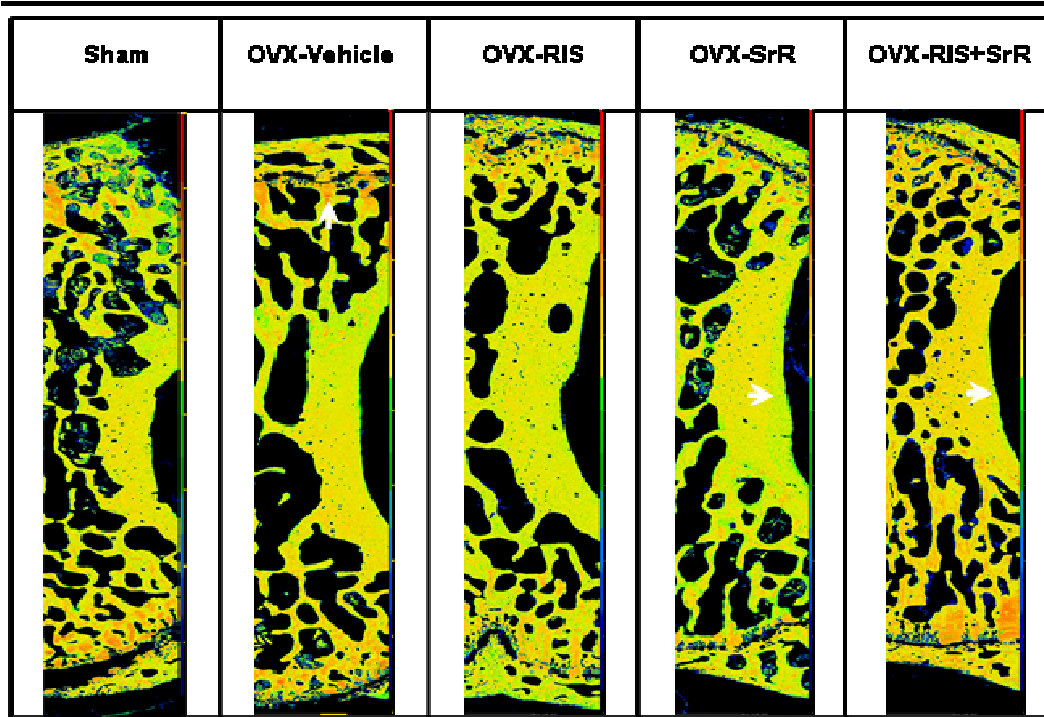


Figure 3-4 Electron probe micro analysis (EPMA) maps of calcium distribution. (Anterior-Posterior view of half of the vertebral body). Warmer colors indicate higher concentrations of elemental calcium.

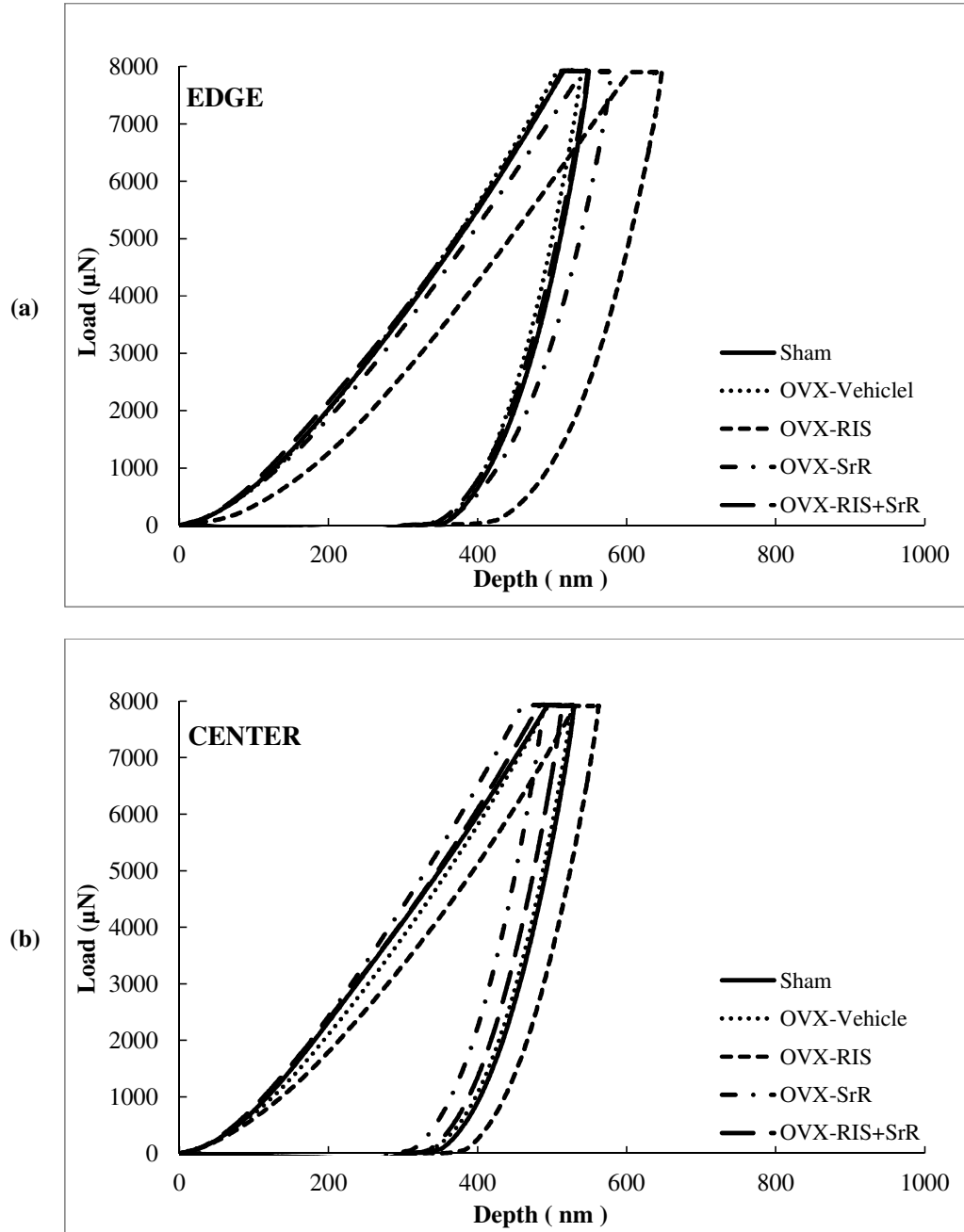


Figure 3-5 Depth (nm) vs. Load ( $\mu\text{N}$ ) curves from nanoindentation tests of different groups. a) Curves from indenting on EDGE. OVX-RIS shows a trend towards higher contact depth under the same indenting condition. b) Curves from indenting on CENTER. There were no apparent differences in contact depth between the treatments in the CENTER region of older, non remodelling bone.

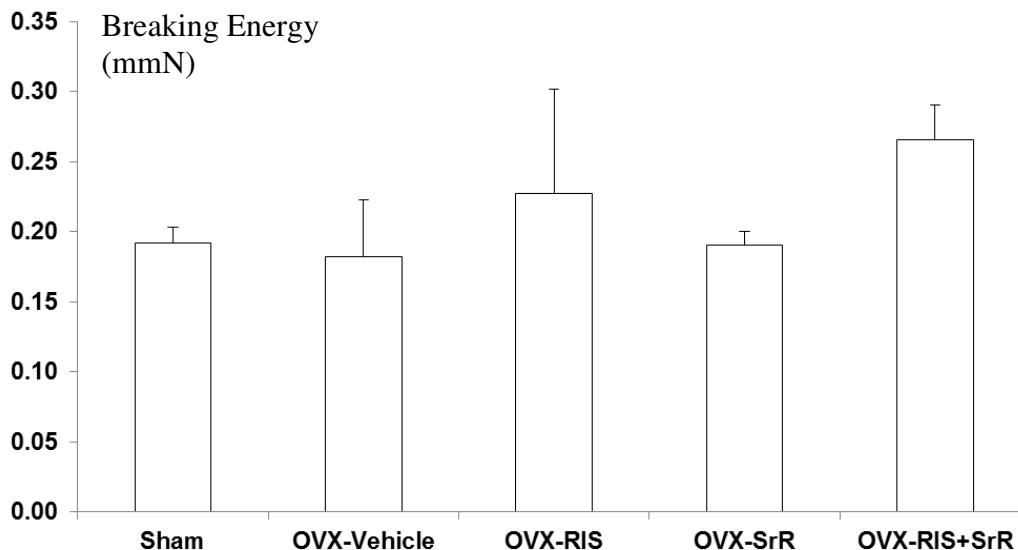


Figure 3-6 The breaking energy of rat vertebrae L5, L6 tested under load (in compression) to failure.

### 3.5. Discussion

Bone fracture is a serious health concern with postmenopausal osteoporosis. Current BP antiresorptive drug interventions are highly effective in the conservation of existing bone volume, trabecular microarchitecture (and structural strength respectively), thereby preventing OP-related fracture during therapy. In our study, it was clear that the BP-treatment of OVX rats resulted in a significant conservation of bone volume and microarchitectural quality over all other treatment groups, which further translated into increased structural breaking energy during mechanical loading in compression.

However, an extensive period of BP drug treatment may also introduce alterations in the remodelling (i.e., replenishing) ability of bone in the long-term [Seeman 2009]. Recent studies have reported the unexpected occurrence of spontaneous atypical subtrochanteric and diaphyseal femoral fractures in OP

patients after long-term BP treatment [Ali and Jay 2009], and those reports were reviewed by an ASBMR appointed task force [Shane et al. 2010]. They concluded that the incidence of fracture associated with BP therapy for osteoporosis appears to be very low, and that a causal association has not been established. Among other recommendations, however, they encouraged further research in animal models to gather additional data to establish the true risk of BP use associated with the conditions of catastrophic structural bone failure, which serves as a rationale for our current investigation.

In contrast to BP drug therapy, SrR treatment (at the dose tested) did not increase the structural breaking energy of vertebral bone during mechanical loading in compression – despite showing some ability in the preservation of trabecular bone volume by *ex-vivo* Micro-CT. Those results agreed with published clinical findings showing that SrR taken over a 3-year period resulted in the preservation of the bone microstructure at the tissue level, but did not translate into increased bone strength, as measured by indentation modulus [Roschger et al. 2010]. They also agreed with the results by Bain et al who found that bone stiffness in SrR-treated animals was unchanged from values measured in OVX animals treated with vehicle – despite measuring the contrasting outcomes of dose-dependent higher maximal load, and the significant conservation of maximal energy to fail compared to OVX-untreated animals [Bain et al. 2009].

Hence, the biological mechanism whereby SrR contributes to improve bone strength and anti-fracture efficacy in clinical trials is still not entirely understood. Recent research by Boyd et al measured improved bone microarchitecture and

reported an increase in stiffness in SrR treated rats as compared to controls [Boyd, Szabo, Ammann 2011]. In that research, dosing with SrR commenced in growing juvenile (i.e., 16 wk) normal Wistar rats, with a SrR dosage of 900mg/kg/day for 104 weeks. The researchers found that SrR-treated rats did not show a decrease in bone strength compared to age-matched normal controls. However, it is difficult to compare those results to our study as we employed 6-month mature OVX Sprague-Dawley rats, with a significantly reduced dosage and duration of SrR (308 mg/kg/day for 16 weeks) which, nonetheless, was previously reported to be at an effective dose range to affect both antiresorptive and anabolic activity [Marie et al. 1993; Ammann et al. 2004].

Our EPMA findings confirmed that in the normal rat, the mineralized bone matrix is heterogeneous in material composition with only trace amounts of elemental Sr uptake from the diet. In stark contrast, after SrR treatment, the Sr atom serves as a surrogate for elemental Ca uptake and was rapidly and heavily incorporated at sites of newly mineralizing bone. Those observations agreed with previously published reports on the incorporation and distribution of Sr in bone [Boivin et al. 2010]. In our study, profound regional differences in elemental composition were sensitively mapped to periosteal cortical and endosteal trabecular bone surfaces. Despite the significant increase in elemental Sr deposited in those regions of mineralized bone matrix, our mechanical testing evaluations of those same defined regions of Sr-enriched bone using nanoindentation did not measure significant differences in bone tissue modulus, albeit confined to the SrR dosage we tested.

The 4 months duration of SrR drug administration in our study was significantly less than that used in the clinical treatment of human patients with osteoporosis. Nonetheless, the 2 wt% of Sr deposition we measured was in accord with Sr deposition attained by taking higher dosages and treating patients for 3 years [Roschger et al. 2010]. Previous studies have concluded that SrR was effective in preventing rat OVX-induced bone loss and improving bone mechanical strength in doses as low as 125 mg/kg/day [Ammann et al. 2004]. In contrast, Fuchs et al suggested that a SrR dosage of 25mg/kg/day for the rat was comparable to the human dosage of 2g/day on a mg/kg basis. Their study also confirmed the 25mg/kg/day dose levels produced serum levels of strontium similar to those found clinically [Marie et al. 1993], but they were not able to confirm the anabolic effect of SrR treatment on the OVX rat at the 25mg/kg/day dose. In a letter to the editor regarding that study, the authors were challenged in that the dose of SrR used was likely too low (i.e., sub-therapeutic)[Marie 2008], and referred to the dose of 308 mg/kg/day in an earlier published study as an effective dose that increased the trabecular bone volume by 30-36% [Marie et al. 1993]. Indeed, in a more recent paper, 900mg/kg/day was used as a SrR dosage in rats to increase bone resistance and promote bone forming activity [Boyd, Szabo, Ammann 2011]. That dose was stated to correspond to twice the human serum circulating level in rats based on pharmacokinetic measurements, but those statements were not supported by the evaluations reported in that paper. If an average postmenopausal osteoporosis patient is 70 kg, on an mg/kg basis that would translate to 63g of SrR per day. Thus, clearly, establishing clarity regarding

the accuracy of pharmacokinetic and pharmacodynamic parameters surrounding SrR usage is of critical importance, as the current human clinical dose remains at the 2g SrR p.o. once daily regimen [Marie et al. 1993].

With our in-vivo Micro-CT analyses, we accurately measured the loss of trabecular bone mass and micro-architectural connectivity in vertebrae from untreated OVX animals developing OP. We found that SrR at the dose of 308 mg/kg/day over 4 months significantly conserved vertebral trabecular bone volume compared to untreated OVX controls, however remained significantly less potent than OVX-RIS treated animals. Namely, in all BP treatment groups, we measured the significant conservation of BV, FD and Tb.Sp compared to both untreated OVX controls, and OVX-SrR dosed animals. Our bone mineral density (BMD) measurements did not show significant differences between any of the treatments, including that of SrR monotherapy [Table 3-1]. In addition, we measured significantly reduced global (i.e., the entire bone sample) mechanical strength of vertebral bone in compression to failure in OVX rats, and the BP drug RIS (either as a monotherapy, or in combination with SrR) significantly improved the mechanical strength of OVX vertebral bone, whereas SrR was unable to significantly impact bone mechanical strength.

Despite the ability for RIS treatment to preserve existing bone mass and micro-architectural structure, remodeled bone formation frequency and duration were significantly reduced in OVX-RIS dosed rats co-administered SrR, compared to OVX-SrR dosed rats, as evidenced by EPMA analysis of incorporated elemental Sr. Thus, for remodelling BP-dosed bone, the significant reduction in trabecular

matrix formation may alter the local volume and material composition of bone. In turn, that would potentially influence the anti-fracture strength, particularly if associated with thinning trabecular bone.

One surprising finding from our study was the non-significant trend of OVX-RIS samples exhibiting increased contact depth under nanoindentation compared to all other treatment groups. Clearly, BP drugs are known to increase the global tissue modulus in great part through the conservation of bone volume and micro-architectural connectivity, which serve to stiffen the bone in response to load. However, it is important to note that our nanoindentation measurements were conducted in regions of newly formed bone (i.e., mineralized osteoid) that incorporated significant amounts of BP, SrR, or a combination of those drug molecules. Thus, the localized presence of those drugs likely influenced cellular biology and bone matrix formation in a “site-specific” manner.

There are several limitations of this preliminary study. Firstly, the sample number per treatment group remained small, due to the complexity and expense of coordinating precise regional analyses of drug-dosed bone regions between the Micro-CT, EPMA and nanoindentation techniques that were employed. However, as our study purpose was to contrast the material and compositional make-up of bone after BP and/or SrR drug therapy in an animal model of OP, our findings should remain of interest. Another study limitation was that our nanoindentation facility is limited to the indentation of dry bone samples. Therefore, the depth-displacement curves of dried samples will likely be stiffer than that measured in hydrated samples, although bone samples from each group were treated and dried

using the same procedure. Thus, comparison of our measured values to those from other facilities may differ in magnitude, as the procedure for sample preparation, testing and handling will differ.

We concluded that BP drugs dominated the conservation of trabecular geometry and corresponding structural bone strength in OP rats, whereas SrR may influence bone volume and material composition locally. The administration of SrR and the subsequent uptake of Sr appeared to have less of an impact on the structural integrity of bone as it did on the utility of its presence in permitting new bone formation during the remodelling cycle. The incorporation of BP and/or Sr drugs (at the dosages used) did not increase the mechanical stiffness of the bone matrix in locations known to contain those drugs, and remained similar to values measured in sham-operated controls.

Our study further highlights the potential that Sr drugs offer for use as exquisite indicators of bone turnover. Perhaps it is the non-ionizing, tracer potential observed when administering sub-therapeutic quantities of SrR that could prove of greatest utility for clinicians in the assessment and understanding of regional bone turnover for individual patients. Further studies will help shed light on the diagnostic tracer utility of Sr based compounds that may eventually find use as effective clinical diagnostic tools in the diagnosis and treatment of bone injury, repair and disease.

### **Acknowledgments**

The authors thank Michael D. Jones and Colin T. Lee for help with drug dosing, and John Simon for help with preparation of the manuscript. We also thank Sergei Matveev for assistance with the EPMA analyses and Eric Flaim for assistance with the Hysitron Triboindenter.

This research was funded by The (Canadian) Arthritis Society (TAS), and by the OA Alberta Team Grant from the Alberta Heritage Foundation for Medical Research (AHFMR).

Authors' roles: Study design: YW, SMA, MJD and MRD. Study conduct: YW, and MRD. Data collection: YW, and DM-P. Data analysis: YW, DM-P, and MRD. Data interpretation: YW, and MRD. Drafting manuscript: YW, and MRD. Revising manuscript content: YW, SMA, MJD, DM-P, and MRD. Approving final version of the manuscript: YW, SMA, MJD, DM-P, and MRD. MRD takes responsibility for the integrity of the data analysis.

### 3.6. References

- Ali T, Jay RH. 2009. Spontaneous femoral shaft fracture after long-term alendronate. *Age Ageing*, 38(5):625-626
- Ammann P, Shen V, Robin B, Mauras Y, Bonjour J P, Rizzoli R. 2004. Strontium ranelate improves bone resistance by increasing bone mass and improving architecture in intact female rats. *J Bone Miner Res*, 19:2012- 2020.

- Bain SD, Jerome C, Shen V, Dupin-Roger I, Ammann P. 2009. Strontium ranelate improves bone strength in ovariectomized rat by positively influencing bone resistance determinants. *Osteoporos Int*, 20:1417-1428
- Boivin G, Farlay D, Khebbab M T, Jaurand X, Delmas P D, Meunier P J. 2010. In osteoporotic women treated with strontium ranelate, strontium is located in bone formed during treatment with a maintained degree of mineralization. *Osteoporos Int*, 21:66-677
- Bonnelye E, Chabadel A, Saltel F, Jurdic P. 2008. Dual effect of strontium ranelate: stimulation of osteoblast differentiation and inhibition of osteoclast formation and resorption in vitro. *Bone*, 42:129-138
- Borgström F, Ström O, Coelho J et al. 2010. The cost-effectiveness of strontium ranelate in the uk for the management of osteoporosis. *Osteoporos Int*, 21:339-349
- Bouxsein ML, Boyd SK, Christiansen BA et al. 2010. Guidelines for Assessment of Bone Microstructure in Rodents Using Micro-Computed Tomography. *J Bone Miner Res*, 25: 1468-1486
- Boyd SK, Szabo E, Ammann P. 2011. Increased bone strength is associated with improved bone microarchitecture in intact female rats treated with strontium Ranelate: A finite element analysis study. *Bone*, 48:1109-1116
- Campbell GM, Bernhardt R, Scharnweber D, Boyd SK. 2011. The bone architecture is enhanced with combined PTH and alendronate treatment

- compared to monotherapy while maintaining the state of surface mineralization in the OVX rat. *Bone*, 49(2):225-232
- Chappard D, Legrand E, Haettich B. et al. 2001. Fractal dimension of trabecular bone: comparison of three histomorphometric computed techniques for measuring the architectural two-dimensional complexity. *J. Pathol.* 195: 515-521
- de Villiers TJ. 2009. Bone health and osteoporosis in postmenopausal women. *Best Pract Res Clin Obstet Gynaecol*, 23:73-85
- Fischer-Cripps AC. 2004. Nanoindentation, 2nd ed. Springer, New York, pp 197
- Fischer-Cripps AC. 2007. Introduction to contact mechanics, 2nd ed. Springer, New York, pp 221
- Fuchs RK, Allen MR, Condon KW et al. 2008. Strontium ranelate does not stimulate bone formation in ovariectomized rats. *Osteoporos Int*, 19:1331-1341
- Griffiths J. 2007. Raman spectroscopy for medical diagnosis. *Anal Chem*, 79:3975-3978
- Hiligsmann M, Bruyère O, Reginster JY. 2010. Cost-effectiveness of strontium ranelate versus risedronate in the treatment of postmenopausal osteoporotic women aged over 75 years. *Bone*, 46:440-446
- Hwang JS, Chen JF, Yang TS et al. 2008. The effects of strontium ranelate in asian women with postmenopausal osteoporosis. *Calcif Tissue Int*, 83:308-314

- Iwata K, Li J, Follet H, Phipps RJ, Burr DB. 2006. Bisphosphonates suppress periosteal osteoblast activity independently of resorption in rat femur and tibia. *Bone*, 39:1053-1058
- Marie PJ, Hott M, Modrowski D et al. 1993. An uncoupling agent containing strontium prevents bone loss by depressing bone resorption and maintaining bone formation in estrogen-deficient rats. *J Bone Miner Res*, 8:607-615
- Marie PJ. 2008. Effective doses for strontium ranelate. *Osteoporos Int*, 19:1813
- Meunier PJ, Roux C, et al. 2004. The effects of strontium ranelate on the risk of vertebral fracture in women with postmenopausal osteoporosis. *N Engl J Med*, 350:459-468
- Muscoso E, Puglisi N, Mamazza C et al. 2004. Antiresorption therapy and reduction in fracture susceptibility in the osteoporotic elderly patient: open study. *Eur Rev Med Pharmacol Sci*, 8:97-102
- Reginster J, Minne HW, Sorensen OH et al. 2000. Randomized trial of the effects of risedronate on vertebral fractures in women with established postmenopausal osteoporosis. Vertebral Efficacy with Risedronate Therapy (VERT) Study Group. *Osteoporos Int*, 11:83-91
- Reszka AA, Rodan GA. 2004. Nitrogen-containing bisphosphonate mechanism of action. *Mini Rev Med Chem*, 4:711-719
- Roschger P, Manjubala I, Zoeger N et al. 2010. Bone material quality in transiliac bone biopsies of postmenopausal osteoporotic women after 3 years of strontium ranelate treatment. *J Bone Miner Res*, 25:89-900

Seeman E. 2009. To stop or not to stop, that is the question. *Osteoporos Int*, 20:187-195

Shane E, Burr D, Ebeling PR et al. 2010. Atypical subtrochanteric and diaphyseal femoral fractures: report of a task force of the American Society for Bone and Mineral Research. *J Bone Miner Res*, 25:2267-2294

## **Chapter 4**

# **A Simple Method for the Finite Element Analysis of Bone Stiffness from Micro-CT Derived Bone Microarchitecture for the Non-Engineer - A Case Study on Osteoporosis Rat Bone**

---

The contents of this chapter have been submitted as a manuscript to the Journal of Orthopaedic Research.

## 4.1. Abstract

**Purpose:** The purpose of our study was to: 1) validate structure parameters, which can describe the changes of microarchitecture and stiffness for rat bone before/after the onset of osteopenia; 2) build a succinct finite element analysis (FEA) process to calculate bone stiffness; 3) correlate bone stiffness with structural parameters from Micro-CT images, to provide an assessment of predicted bone strength.

**Methods:** Twenty 3-month old female Sprague Dawley rats were included in this study. Ten rats were ovariectomized (OP-OVX-Vehicle) while the remaining ten rats were sham-operated (OP-Sham). After 12 weeks, all rats were euthanized and their lumbar vertebrae 4 to 6 (L4 to L6) dissected and scanned with micro-computed tomography (Micro-CT) at 18 $\mu$ m voxel imaging resolution. From the Micro-CT images, a cylindrical region of interest was segmented from the vertebral trabecular bone. The structural parameters of bone volume/tissue volume (BV/TV; %), bone mineral density (BMD; g/cm<sup>3</sup>), trabecular thickness (Tb.Th; mm), trabecular separation (Tb.Sp; mm), fractal dimension (FD), trabecular bone pattern factor (Tb.Pf; 1/mm), degree of anisotropy (DA) and connectivity density (Conn.Dn; 1/mm<sup>3</sup>) were measured. The 40% of the cylinder from the caudal side was selected for linear and elastic finite element analysis (FEA) with Young's modulus (E) = 24.5GPa and Poisson's ratio ( $\nu$ ) = 0.3. The model was fixed on the bottom and loaded on the top with 5% strain. The stiffness (k) of the bone was reported after the analysis. The values of k were further normalized with the theoretical stiffness (k') which was calculated from the size

of each cylinder by assuming that the cylinder was solid. The index of bone stiffness was represented as  $k/k'$ .

**Results:** For the same level of vertebrae, most of the parameters measured showed significant difference between OP-Sham and OP-OVX-Vehicle, except Tb.Th and DA. The average values of all measured parameters (except Tb.Th) showed significant differences with the onset of osteopenia, secondary to ovariectomy. The curves of BV/TV, BMD and FD decreased toward the middle of the vertebral body; the curves of Tb.Sp and Tb.Pf increased toward the middle of the vertebral body. The stiffness index of OP-OVX-Vehicle ( $0.141 \pm 0.053$ ) was significantly ( $p < 0.05$ ) less than that of OP-Sham ( $0.383 \pm 0.092$ ). Although, values of Conn.Dn were significantly different between groups, the Pearson's correlation coefficients indicated that Conn.Dn had no significant correlation to the calculated stiffness. The values of BV/TV, BMD and FD were positively correlated with the index of stiffness, and the correlation was significant at the 0.05 level. In contrast, Tb.Sp and Tb.Pf were negatively correlated with the index of stiffness.

**Conclusion:** We have developed and tested a simple and efficient method for the assessment of trabecular bone stiffness by FEA from measurements derived by Micro-CT. This methodology may find utility with the non-engineer, for the rudimentary mechanical assessment of bone strength in experimental models of bone disease, or to gauge the effects of drug interventions.

## 4.2. Introduction

Micro-computed tomography (Micro-CT) has become a common tool in most bone biology laboratories and is acknowledged as a valuable technique for investigating the microarchitecture of bone, for both in-vivo and ex-vivo applications [Kinney et al. 1998; Kim et al. 2003; Cohen et al. 2010; Ito 2011]. The Micro-CT derived images from reconstructed data accurately represent bone microstructural parameters for quantitative assessments [Bouxsein et al. 2010]. In addition, as the X-ray passes through the sample, the relative linear attenuation of the sample is represented on the image projections as values of gray scale [Davis and Wong 1996]. Corresponding X-ray attenuation on reconstructed images can thus be converted to bone mineral density (BMD) by calibrating the values with a tissue “phantom” of known mineral density. For trabecular bone, the structural parameters derived from Micro-CT data are based on traditional static bone histomorphometry, which evaluated the thickness, connectivity, distribution and spacing of the trabeculae. Measured parameters by Micro-CT, including bone volume/tissue volume (BV/TV; %), trabecular number (Tb.N), trabecular thickness (Tb.Th; mm) and trabecular separation (Tb.Sp; mm), have all been successfully utilized to assess the microarchitecture of rodent trabecular bones [Bouxsein et al. 2010]. In addition, there are other parameters that can also be used to represent bone microarchitecture, such as the fractal dimension (FD), trabecular bone pattern factor (Tb.Pf; 1/mm), degree of anisotropy (DA) and connectivity density (Conn.Dn; 1/mm<sup>3</sup>) [Table 4-1] [SkyScan 2009]. Although those parameters are well established with their own definitions, they remain

indirect indices and require other tools to interpret the bone stiffness and potential for mechanical failure (i.e., fracture) [Diederichs et al. 2009; Mazurkiewicz and Topoliński 2009]. Resultantly, in bone research, the numerical method, finite element, was applied to assist in analyzing bone stiffness [Liu et al. 2010; Jayakar et al. 2012].

Finite element method is founded on numerical methods for calculating the mechanics in various fields in industries. For bone analysis, the procedure starts by acquiring computed tomography images to build the geometry of the bone, which may include both trabecular and cortical components. Each voxel in the image stacks can be converted to an element in the finite element mesh. The material properties required in the analysis can also be inferred from the gray scale values on the images to enable a more accurate representation of the local stiffness of different bone structures [Zannoni et al. 1998; Vilayphiou et al. 2011; Rizzoli et al. 2012]. This process has been successfully implemented in many animal models [Macneil and Boyd 2008] including modelling the entire rat vertebra, the vertebral body (without the top and bottom growth plates), and the trabecular bone compartment alone [Kinney et al. 2000; Rhee et al. 2009]. Nevertheless, the procedure from image segmentation to the modelling of finite element analysis is not readily accessible to the biological scientist; and inappropriate bone modelling techniques may result in redundant calculation in finite element analysis (FEA). Thus, our aim was to simplify the selection of Micro-CT derived bone geometry for the application to FEA and subsequently correlate the FEA results to bone microstructural and density based material

parameters as an initial rudimentary assessment of bone stiffness [van Rietbergen et al. 1998].

Our study hypothesis was that structural and density based parameters of bone from Micro-CT can be correlated to bone stiffness.

Table 4-1 Definitions of structural parameters of trabecular bone.

<b>ASBMR</b>	<b>Parameter Name (ASBMR)</b>	<b>Description</b>	<b>Unit</b>
<b>BV/TV</b>	percent bone volume	Ratio of the segmented bone volume to the total volume of the region of interest.	%
<b>Tb.Th</b>	trabecular thickness	Mean thickness of trabeculae, assessed using direct 3D methods.	mm
<b>Tb.Sp</b>	trabecular separation	Mean distance between trabeculae, assessed using direct 3D methods.	mm
<b>Tb.Pf</b>	trabecular bone pattern	Index of connectivity.	mm <sup>-1</sup>
<b>Conn.Dn</b>	connectivity density	Redundant connectivity density.	mm <sup>-3</sup>
<b>DA</b>	degree of anisotropy	Length of longest divided by shortest mean intercept length vector.	
<b>FD</b>	fractal dimension	Indicator of surface complexity of an object. Quantifies how the object's surfaces fill the space.	

### 4.3. Materials and Methods

#### Animals

Twenty 3-month old female Sprague Dawley rats were obtained from Charles River and maintained at the University of Alberta Biosciences Animal Services Facility. The protocol pertaining to all procedures and aspects of the study was approved by the University of Alberta animal care and ethics committee. Before arrival, ten rats were ovariectomized (OVX); the other ten rats were sham-

operated as controls. All rats were euthanized 12 weeks after OVX and/or sham surgery and lumbar vertebrae 4 to 6 (L4 to L6) were dissected. The muscle and soft tissues connected to vertebrae were removed, and samples were wrapped in paper towels dampened with phosphate buffered saline and stored frozen at  $-30^{\circ}\text{C}$  for subsequent Micro-CT scan.

### **Micro-CT Scan**

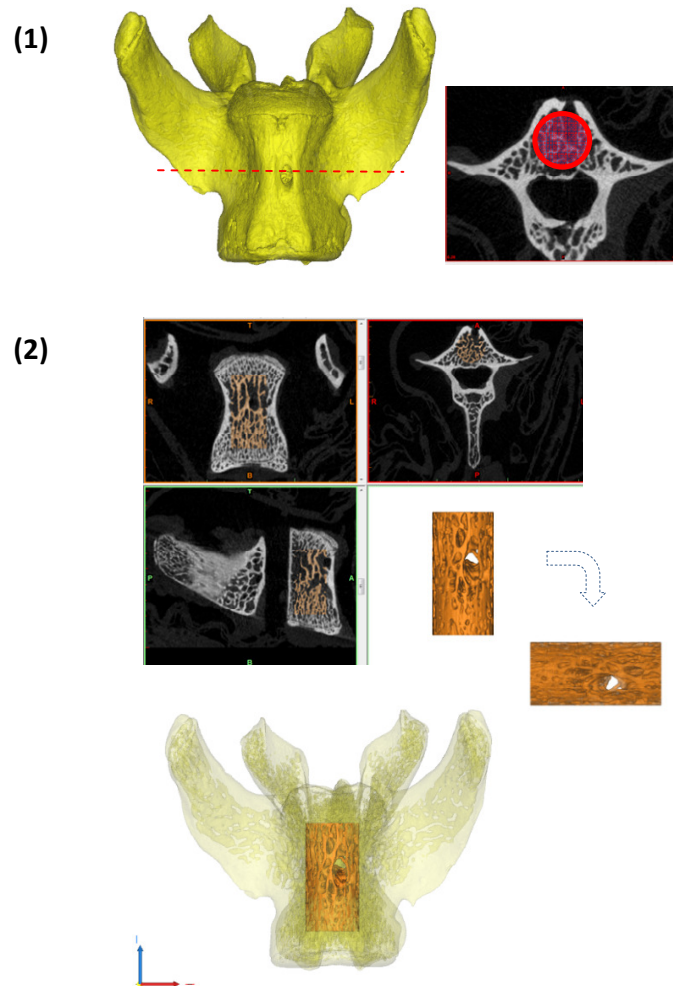
[For the settings of Micro-CT scans and the phantoms for BMD, please refer to Chapter 3, 2.3-Micro-CT imaging.](#)

The excised vertebrae, L4, L5 and L6, were thawed at room temperature for 2 hours before scanning. A cylindrical region of interest (ROI) was segmented from trabecular bone within the vertebral body [Figure 4-1]. The diameter of each cylinder was constrained by the endocortical bone margin enclosing the vertebra. The vertebral growth plates at each end were used to landmark the top and bottom segmentation boundaries. The threshold, 70~255, was chosen to segment out bone on 8-bit (0~255 gray level) bitmap (BMP) images. The measured structural parameters were BV/TV, BMD, Tb.Th, Tb.Sp, FD, Tb.Pf, DA and Conn.Dn. Those parameters were calculated three dimensionally (3D) based on the volume of the cylinder. Except for Conn.Dn, all structure parameters were also calculated two dimensionally (2D) from cross sectional images slice by slice along the longitudinal direction from caudal to cranial [Figure 4-2] and graphed with respect to the normalized height of the cylinder. The results were compared between groups and different levels of vertebrae in the same group.

## Finite Element Analysis

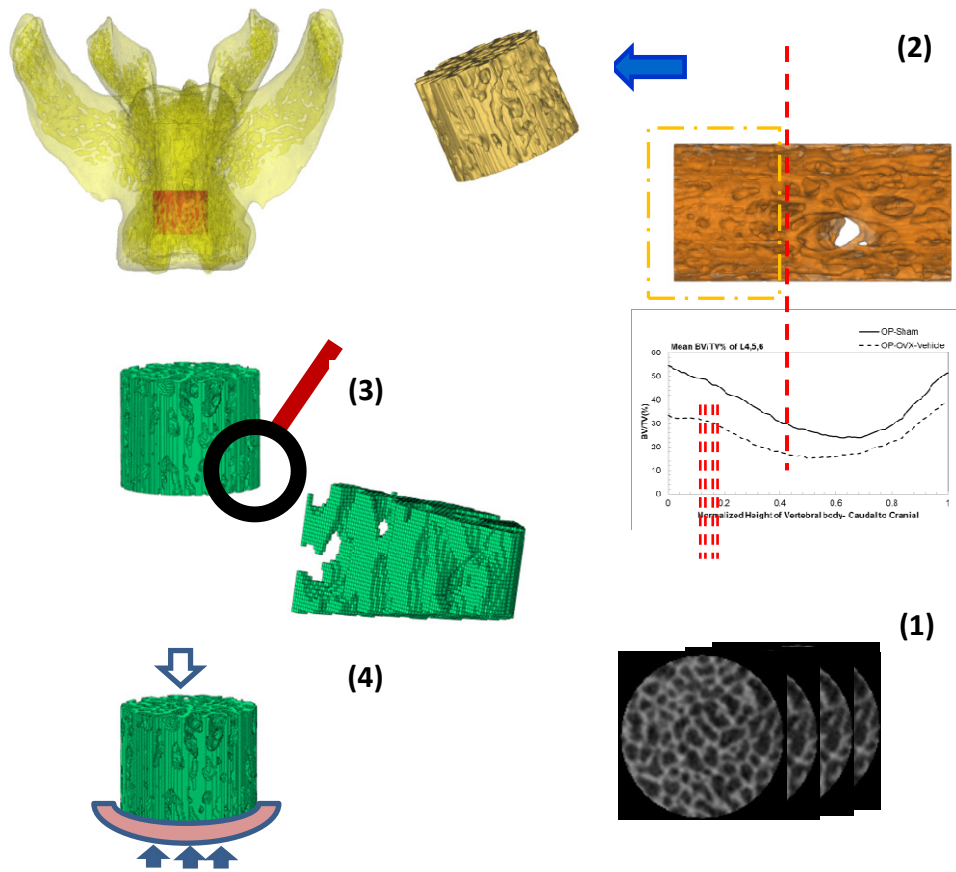
The results of the Micro-CT structural parameters indicated that the largest differences between groups were in the 40% portion of the cylindrical length from the caudal side. Thus, it was selected for FEA [Figure 4-2]. The cross sectional images from this region were imported into Mimics 14.11 (Materialise, Leuven Belgium) to build finite element meshes. Since the voxel of the Micro-CT data was  $18\mu\text{m}$  ( $\approx 17.156\mu\text{m}$ ), that dimension was used to build voxel meshes (hexahedral elements) for FEA to maintain the details of the microarchitecture. To avoid losing or distorting microarchitecture of trabeculae, no resizing or smoothing was undertaken prior to meshing. After creating hexahedral elements (hex8), the meshes were exported as an input file (\*.inp) format of ABAQUS (SIMULIA, Providence RI). The remaining pre-processing to include material properties and boundary conditions were done in ABAQUS/CAE 6.10-1. Since bone is expected to behave elastically, and failure expected with small strain [Evans 1969], the analysis was set as linear and elastic with Young's modulus ( $E$ ) = 24.5GPa and Poisson's ratio ( $\nu$ ) = 0.3 [Guo and Goldstein 2000]. All vertebrae were assigned with the same material property, as no significant difference of material properties was measured between normal and OVX bone [Guo and Goldstein 2000]. The bottom of the cylinder was fixed and a displacement ( $\Delta d$ ), 5% of the height of the cylinder (strain=0.05), was applied at the top of the cylinder. The stiffness ( $k$ ) of the bone was calculated by dividing the summation of the vertical reaction forces ( $R$ ) on the fixation to the applied displacement. Since the sizes of individual vertebrae varied, the stiffness (which comprises

information of geometry and material property) would also vary with size. Therefore, the values of  $k$  were further normalized with the theoretical stiffness ( $k'$ ) which was calculated from the size of each cylinder by assuming that the cylinder was solid [Figure 4-3]. The index of bone stiffness was represented as  $k/k'$ .



Steps	Tools
1. Region of interest (ROI) drawing. a. Find the middle slice of Micro-CT image. b. Draw an ROI to cover the trabecular bone.	CTAn 1.11.6.0
2. Volume of interest (VOI) drawing. Extend ROI up and down, but exclude the growth plates.	CTAn 1.11.6.0

Figure 4-1 Draw a VOI of a trabecular bone cylinder at rat vertebrae.



Steps	Tools
1. Excise a section for FEA. a. Analyze BV/TV% of this cylinder of trabecular bone from caudal to cranial direction. b. Greatest difference found in 2/5 length of the left part.	CTAn 1.11.6.0
2. Excise the section for FEA	Mimics 14.11
3. Mesh with 8 node hexahedral elements (element size=voxel size)	Mimics 14.11
4. Apply boundary conditions for calculating stiffness	ABAQUS 6.10-1

Figure 4-2 Steps for calculating stiffness of the trabecular bone cylinder of rat vertebra.

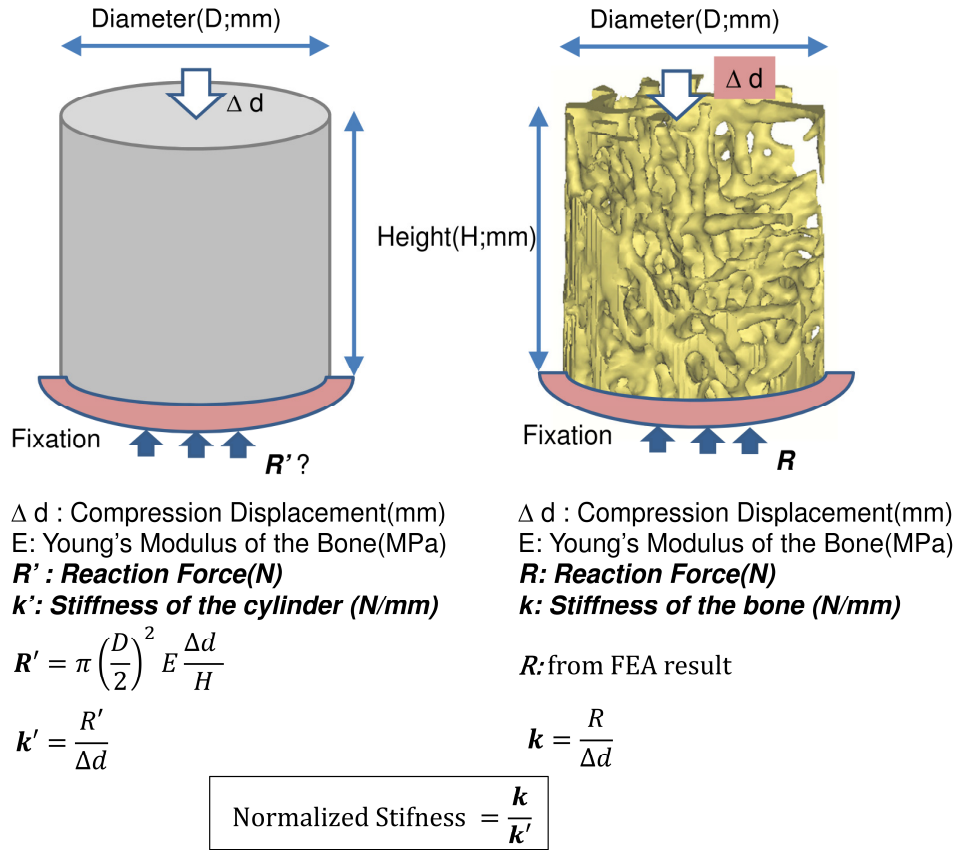


Figure 4-3 Calculations of the index of stiffness ( $k/k'$ ).

### Statistics

PASW® Statistics 17.0 was used for statistical evaluations. The independent t-test was used to find differences between individual groups on the same level of vertebrae. This method was applied to both the results of Micro-CT structure parameters, and the stiffness calculated by the FEA. The difference among three difference levels (L4, 5 and 6) of the same group was tested by one-way ANOVA. The post-hoc multiple comparisons were done by the Tukey test to understand the difference between two individual vertebral levels. The results were shown as mean  $\pm$  standard deviation (SD). An asymptotic value (p-value)  $< 0.05$  was used to evaluate the significance of differences. The correlation between Micro-CT

structural parameters and the index of stiffness were described with Pearson's correlation coefficients ( $r$ ). The significance level was set at 0.05 ( $\text{Sig} < 0.05$ ) with the two-tailed test.

## 4.4. Results

### **Micro-CT Scan**

#### *3D structural parameters*

The results of each structural parameter at different levels along the height of the vertebra were listed in Table 4-2. For the same level of the vertebrae, most of the parameters showed significant difference between OP-Sham and OP-OVX-Vehicle, except Tb.Th and DA. No significant difference of Tb.Th was found between OP-Sham and OP-OVX-Vehicle at the same level of the vertebrae. As to the results of DA, values of L5 did not show significant difference between OP-OVX-Vehicle and OP-Sham. In addition, osteoporosis (OP) did not change the thickness of trabeculae, and the change of DA was not consistent in all vertebrae to validate the occurrence of OP. Since OP is a systemic metabolic disease, all vertebrae should experience the same changes after OVX. Therefore, in addition to comparing the results of the vertebrae at the same level, all results along the height of the vertebrae in the same group were averaged then compared to the other group. Except for Tb.Th, the average values of all parameters showed significant differences after the occurrence of OP [Figure 4-4]. Besides variations between groups, the morphometric changes from L4 to L6 in the same group were analyzed to provide further evaluation of OP.

The different patterns of structural parameters among the same group and between the two groups were investigated to evaluate the spatial effect of OP. When comparing values between different levels of vertebrae in OP-Sham, no obvious trends between L4 to L6 were observed. However, in both groups, BMD, Tb.Th. and DA showed significant difference between L4 and L6 ( $L6 > L4$ ). FD in OP-OVX-Vehicle showed significant differences among vertebral levels [Table 4-2] with the values increasing with the sequential vertebral segment. This phenomenon was not seen in OP-Sham.

### *2D structural parameters*

The structural parameters of image slices were calculated and plotted as curves to show the variations along the caudal-cranial direction. As the curves in the same group showed the same shapes, the curves of L4, L5 and L6 were averaged to represent each group. The curves of BV/TV, BMD and FD were measured to decrease toward the middle; the curves of Tb.Sp and Tb.Pf increased toward the middle [Figure 4-5]. In accordance with the observation from 3D models built from Micro-CT images, it was clear this reflected the vascular foramina present in the vertebral body. Under the 18 $\mu$ m voxel resolution, several foramina were evident from the anterior view. Only Tb.Sp showed the opposite phenomena, since its measurement was magnified by the anatomical structure, foramen [Figure 4-6].

Table 4-2 3D structure parameters of rat lumbar vertebrae calculated from Micro-CT images.

		Treatment							
		OP-Sham				OP-OVX-Vehicle			
		L4 (n=10)	L5 (n=10)	L6 (n=10)	Total (n=30)	L4 (n=10)	L5 (n=10)	L6 (n=10)	Total (n=30)
<b>BV/TV(%)</b>	Mean	34.3	32.8	39.0	35.4	<sup>c</sup> 20.0	23.3	<sup>a</sup> 26.7	23.3
	SD	5.4	7.5	5.3	6.5	3.8	3.3	3.1	4.3
<b>BMD (g/cm<sup>3</sup>)</b>	Mean	<sup>c</sup> 0.207	0.251	<sup>a</sup> 0.304	0.254	<sup>bc</sup> 0.066	<sup>ac</sup> 0.157	<sup>ab</sup> 0.239	0.154
	SD	0.035	0.069	0.075	0.072	0.024	0.062	0.060	0.088
<b>Tb.Th(mm)</b>	Mean	<sup>c</sup> 0.104	<sup>c</sup> 0.104	<sup>ab</sup> 0.114	0.108	<sup>c</sup> 0.106	<sup>c</sup> 0.109	<sup>ab</sup> 0.114	0.110
	SD	0.006	0.010	0.006	0.009	0.004	0.004	0.004	0.005
<b>Tb.Sp(mm)</b>	Mean	<sup>c</sup> 0.242	0.251	<sup>a</sup> 0.264	0.252	0.410	0.384	0.367	0.387
	SD	0.015	0.019	0.025	0.022	0.078	0.063	0.047	0.064
<b>FD</b>	Mean	2.40	2.38	2.43	2.40	<sup>bc</sup> 2.23	<sup>ac</sup> 2.27	<sup>ab</sup> 2.31	2.27
	SD	0.05	0.10	0.04	0.07	0.05	0.03	0.03	0.05
<b>Tb.Pf(1/mm)</b>	Mean	-1.53	-0.54	-3.54	-1.87	<sup>c</sup> 5.46	4.02	<sup>a</sup> 2.60	4.03
	SD	2.84	4.85	2.57	3.67	1.81	1.16	1.34	1.85
<b>DA</b>	Mean	<sup>c</sup> 0.806	<sup>c</sup> 0.777	<sup>ab</sup> 0.585	0.723	<sup>c</sup> 0.901	<sup>c</sup> 0.815	<sup>ab</sup> 0.702	0.806
	SD	0.099	0.103	0.135	0.148	0.061	0.101	0.088	0.117
<b>Conn.Dn (1/mm<sup>3</sup>)</b>	Mean	<sup>c</sup> 84.6	<sup>c</sup> 87.1	<sup>ab</sup> 69.0	80.2	38.5	40.6	45.4	41.5
	SD	15.0	17.8	7.3	15.9	8.3	5.4	6.2	7.1

Data expressed as Mean, SD. p value <0.05 means significantly different from others.

<sup>a</sup>Significantly different from L4 under the same treatment. <sup>b</sup>Significantly different from L5 under the same treatment. <sup>c</sup>Significantly different from L6 under the same treatment.

Abbreviations: BV/TV: bone volume/tissue volume; BMD: bone mineral density; Tb.Th: trabecular thickness; Tb.Sp: trabecular separation; FD: fractal dimension; Tb.Pf: trabecular bone pattern factor; DA: degree of anisotropy; Conn.Dn: connectivity density

### Finite Element Analysis

Based on the reaction force extracted from FEA, the normalized stiffness values (k/k') were 0.383±0.092 for OP-Sham and 0.141±0.053 for OP-OVX-Vehicle. This stiffness index of OP-OVX-Vehicle was significantly (p<0.05) less than that for OP-Sham [Figure 4-7]. The Micro-CT structure parameters of this 40% length of the trabecular cylinder were also calculated in 3D. The results showed that DA was not different (p>0.05) between OP-Sham and OP-OVX-Vehicle. The Pearson's correlation coefficients showed that BV/TV, BMD and FD were positively correlated with the index of stiffness, and the correlation was

significant at the 0.05 level. On the contrary, Tb.Sp and Tb.Pf were negatively correlated with the index of stiffness. The values of Conn.Dn were significantly different between groups, yet; they showed no significant correlation to the calculated stiffness [Table 4-3].

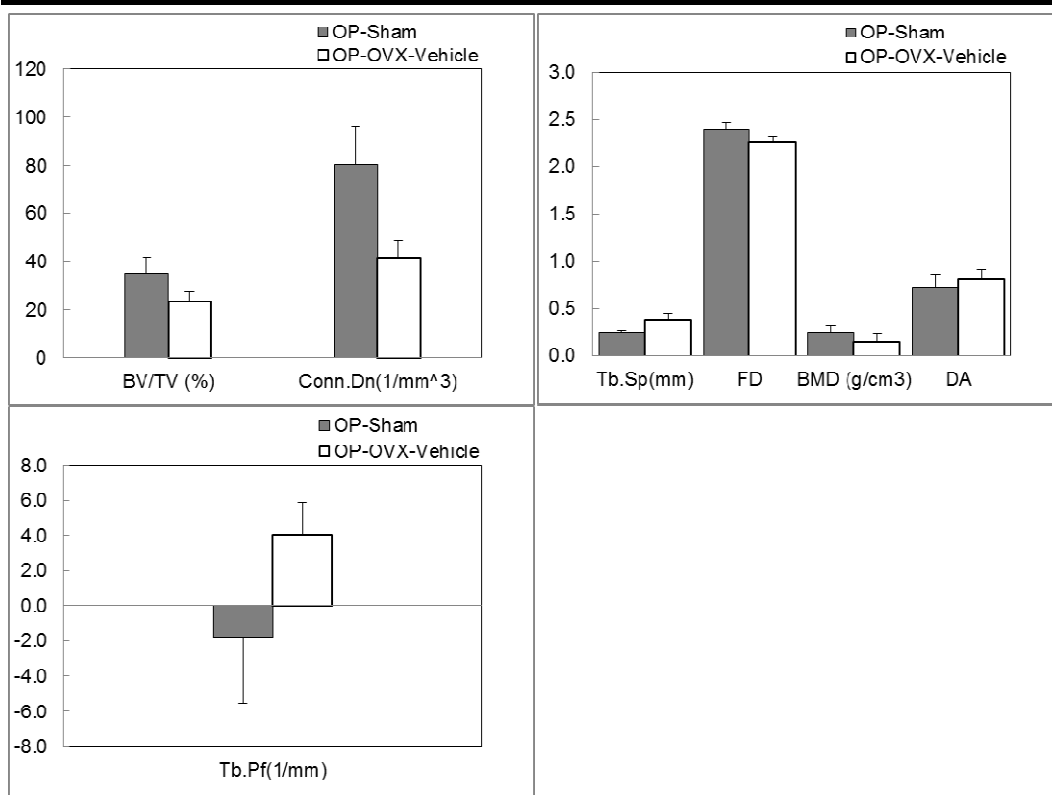


Figure 4-4 3D Micro-CT structure parameter graphs comparing OP-Sham to OP-OVX-Vehicle. Only parameters which showed significant differences ( $p < 0.05$ ) were graphed.

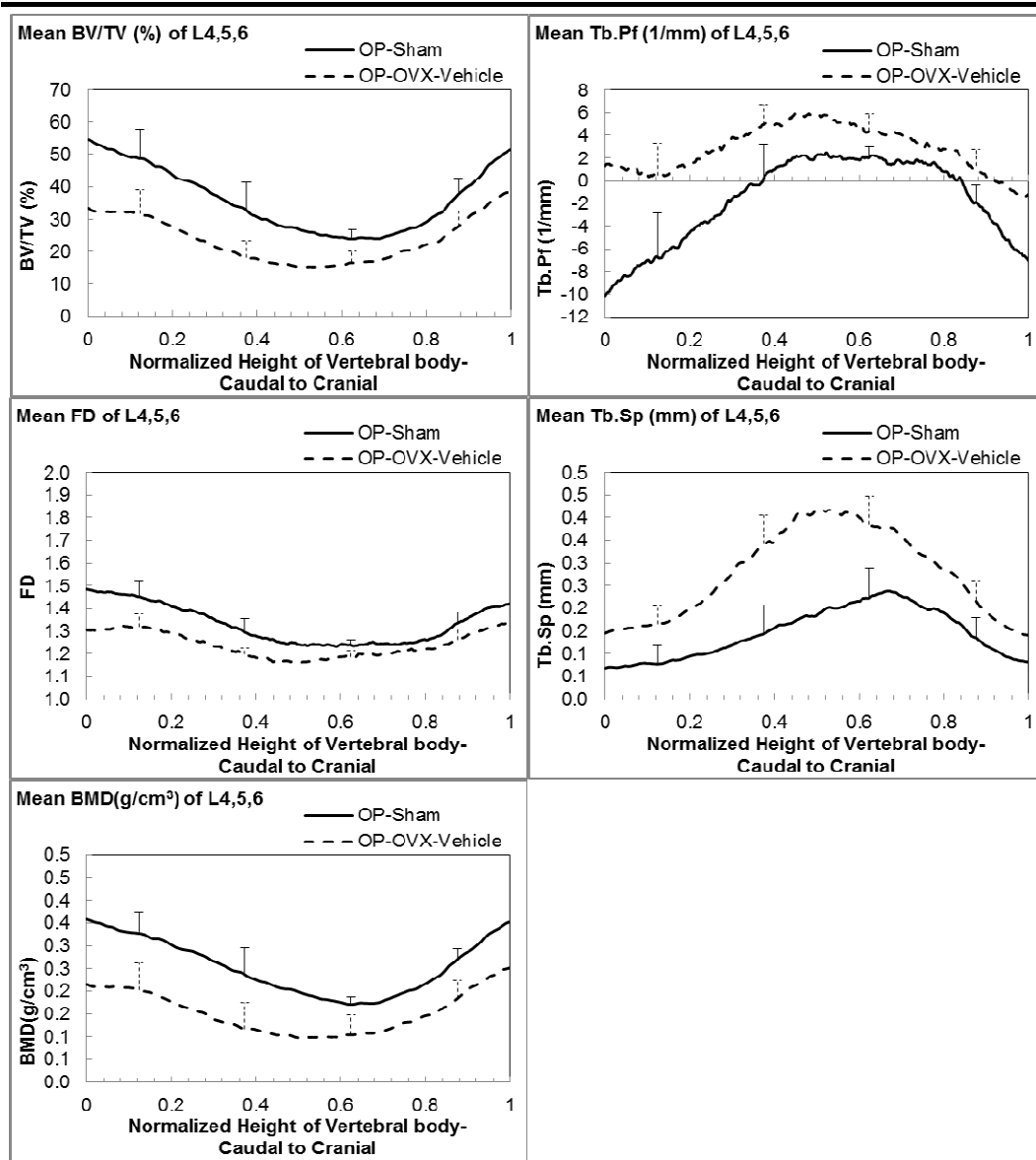


Figure 4-5 2D structural parameters, BV/TV(%), Tb.Pf(1/mm), FD, Tb.Sp(mm), BMD(g/cm<sup>3</sup>), of the cylinder trabecular bone along the longitudinal axis from the caudal to cranial direction. X-axis was normalized by the height of each vertebral body (trabecular cylinder). (x axis: Caudal to Cranial; 0 to 1)

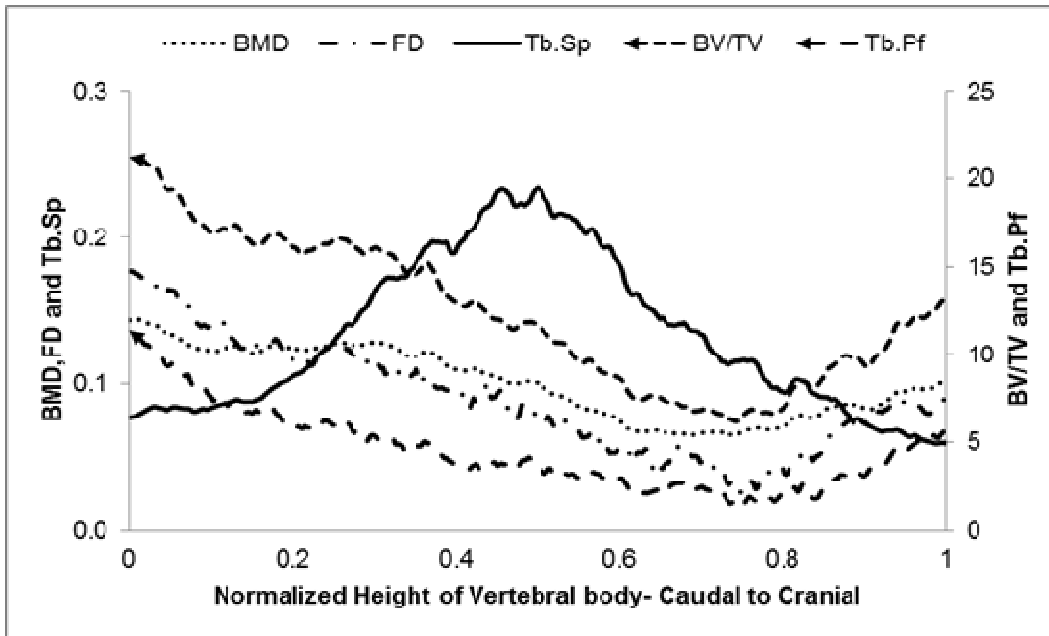


Figure 4-6 Difference (absolute value) of 2D Micro-CT parameters between OP-Sham and OP-OVX- Vehicle. The maximum difference of Tb.Sp is in the middle of the vertebra. All other curves show the minimum difference in the middle right of the vertebral body. (x axis: Caudal to Cranial; 0 to 1)

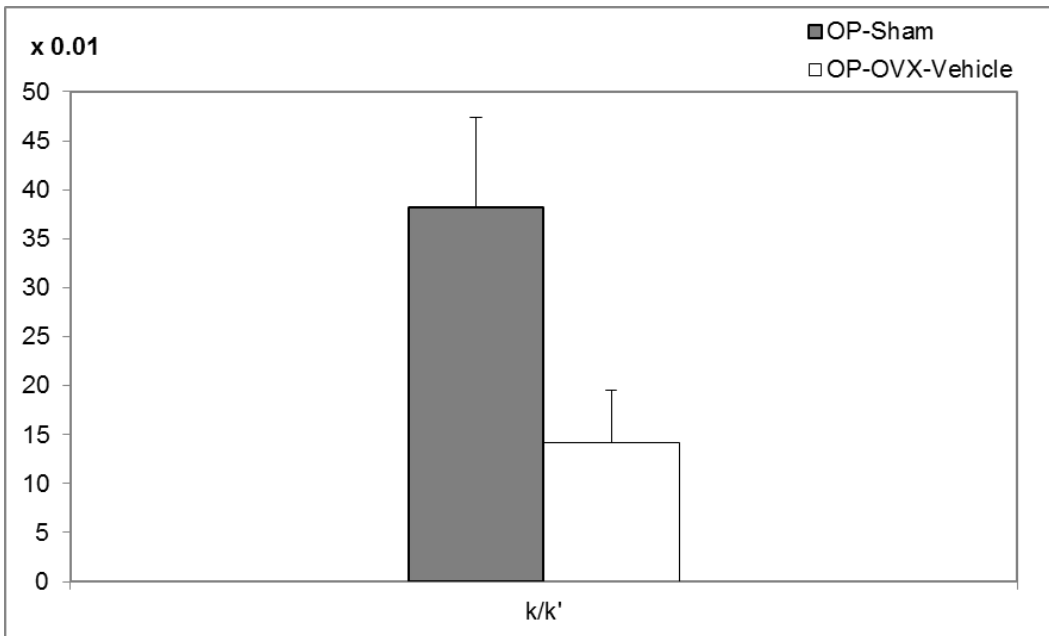


Figure 4-7 Normalized stiffness index ( $k/k'$ ) of the trabecular cylinder of L4 vertebra. The values are significantly different ( $p < 0.05$ ).

Table 4-3 3D structural parameters & stiffness index of the 4/10 length L4.

			Treatment			
			OP-Sham		OP-OVX-Vehicle	
			L4(n=10)		L4(n=10)	
<b>BV/TV(%)</b>	Mean	r	41.7	0.934	23.1	0.965
	SD	Sig.	7.2	0.000	5.2	0.000
<b>BMD (g/cm<sup>3</sup>)</b>	Mean	r	0.248	0.674	0.083	0.954
	SD	Sig.	0.032	0.032	0.030	0.000
<b>Tb.Th(mm)</b>	Mean	r	0.102	0.817	0.103	0.726
	SD	Sig.	0.006	0.004	0.005	0.018
<b>Tb.Sp(mm)</b>	Mean	r	0.166	-0.838	0.341	-0.784
	SD	Sig.	0.013	0.002	0.166	0.007
<b>FD</b>	Mean	r	2.48	0.928	2.26	0.948
	SD	Sig.	0.06	0.000	0.06	0.000
<b>Tb.Pf(1/mm)</b>	Mean	r	-4.00	-0.956	5.46	-0.965
	SD	Sig.	4.08	0.000	2.48	0.000
<b>DA</b>	Mean	r	0.557	0.238	0.525	0.502
	SD	Sig.	0.044	0.508	0.056	0.139
<b>Conn.Dn (1/mm<sup>3</sup>)</b>	Mean	r	131.6	0.542	55.2	0.648
	SD	Sig.	23.8	0.105	13.7	0.043
<b>k/k'</b>	Mean	r	0.383	1	0.141	1
	SD	Sig.	0.092		0.053	

Data expressed as Mean, SD. p value <0.05 means significantly different from the other group. p value > 0.05 was *shaded with gray*.

The significant level of Pearson's correlation coefficient (r) was set at 0.05 and means no significant correlation to k/k'. The value (Sig.) >0.05 was *shaded with light up diagonal*.

Abbreviations: BV/TV: bone volume/tissue volume; BMD: bone mineral density; Tb.Th: trabecular thickness; Tb.Sp: trabecular separation; FD: fractal dimension; Tb.Pf: trabecular bone pattern factor; DA: degree of anisotropy; Conn.Dn: connectivity density; k/k': Normalized stiffness value

#### 4.5. Discussion

##### Key Issues Relating to Micro-CT

###### *Resolution issues of images in Micro-CT*

The selection of resolution for Micro-CT imaging is a critical parameter that, if not chosen adequately, would have a high impact on the analysis results. The

average trabecular thickness of OP-Sham obtained from the analyzed images was  $108 \pm 9 \mu\text{m}$  [Table 4-2]. That number was obtained from images scanned at a target resolution of  $18 \mu\text{m}$ . In theory, other resolutions ( $9 \mu\text{m}$  and  $35 \mu\text{m}$ ) available through the Micro-CT imager in our laboratory would also be feasible for scanning rat vertebra. However, the  $18 \mu\text{m}$  resolution meant that each trabecula would contain six voxels along the thickness direction, which was adequate to capture the complex nature of the trabecular structure. In addition, the finite element mesh with six elements per trabecular thickness is considered adequate for the model accuracy. It is worth noting that a possible advantage associated with scanning with a higher resolution is to observe possible micro cracks in the trabecular bone. Nevertheless, scanning our samples with a higher resolution ( $9 \mu\text{m}$ ) was not practical because of the cumbersome file size of the resulting image and the associated doubling of scanning time.

#### *Threshold selection for segmenting bone in image processing*

Besides the resolution, the threshold for segmenting bone is also essential, since the results of the variation along the trabecular longitudinal axis may change with different thresholds. Thus, a consistent threshold should be applied in the same study to exclude differences resulting from variations in thresholds. In general, for calculating the BMD of trabecular bone among different groups, if the values of Hounsfield unit (HU) were not significantly different between groups, the trend of BMD variations should be very similar to those of BV/TV in the 2D curves. This was observed from our results [Figure 4-5] and served as evidence of no significant HU variations between normal and OP bone.

*The meaning of structural parameters and the relation to bone stiffness*

In our study, eight structural parameters were investigated between sham and OVX groups. No significance was found in Tb.Th between groups, indicating that trabecular thickness did not correlate with the bone stiffness under our bone conditions. Tb.N, which implies the traversals through the trabecular space, was not included in our analysis, since the calculation of the trabecular number corresponds to Tb.Th [SkyScan 2009]. Besides Tb.Th, the other variable in the equation (for parallel plate model of trabeculae:  $Tb.N = (BV/TV)/Tb.Th$ ; for cylinder model:  $Tb.N = (((4/\pi) * (BV/TV)) * 0.5) / Tb.Th$ ) of Tb.N was BV/TV. Therefore, the information of Tb.N can refer to BV/TV. The DA and Conn.Dn indicate the interceptions across the trabecular space in any direction in 3D when a line passing through and the redundant connectivity of trabeculae [Figure 4-1]. Although differences were found in DA and Conn.Dn between groups, they were not correlated to the index of bone stiffness. The remaining, BV/TV, BMD, Tb.Sp, FD and Tb.Pf, had significant correlations with the index of stiffness. However, as discussed previously, BV/TV and BMD are, in fact, multiples of each other under the assumption of similar HU in both groups.

The definition of FD is a measure of the amount of space which the surface of an object occupies. A more complex mesh of trabeculae will lead to increased trabecular surfaces throughout the images, and thus, the fractal dimension would be higher and vice versa. From our analysis results, the higher FD was associated with higher stiffness of bone. On the other hand, Tb.Pf (which is based on the assumption that trabecular concavity indicates connectivity and convexity

indicated disconnected structures) showed the opposite tendency. The inference from our results is that higher index of stiffness should be associated with higher BV/TV (or BMD), FD and lower Tb.Pf. From here, those parameters other than BV/TV (or BMD) alone can help to define bone stiffness.

### **Key Issues Relating to FEA**

#### *Bone section for FEA and the advantage of our model*

In rodents, histomorphometric measurements of bone remodelling are complicated by concurrent longitudinal bone growth, which expands both the bone diameter as well as trabecular bone at the growth plates. The bone remodelling, which was influenced by ovariectomy, would best be evidenced on trabecular surfaces. Our analysis of segmented trabecular cylinders excluded bone near the growth plates as well as cortical bone. Excluding cortical bone in FEA to evaluate the stiffness allowed us to isolate the effect of OP on the stiffness of the trabecular bone. Furthermore, in our model, we analyzed 40% of the trabecular cylinder starting from the caudal side. The advantage of using only this section was in avoiding the foramina effects which may reduce the difference between groups. Furthermore, the model with 40% of the length had fewer elements than the model of entire vertebra or trabecular bone. This led to less computational time for the FEA.

#### *Modelling method and the use of solver*

Meshing hexahedral elements by the voxel meshing method allowed the easy creation of the 3D geometry from the acquired CT images. The developed mesh

was adequate for solving the reaction forces and deducing the index of stiffness for the different groups. In general, the element size is often reduced in locations of high stress and strain gradients in order to obtain higher accuracy for the stresses in the direct vicinity of stress concentration. However, for our overall stiffness measurements, we chose to have one size for the elements for all the different models, which was based upon the voxel size. For comparing the stiffness caused from variations of microarchitecture, the linear and elastic material properties of bone provided enough information to analyze the bone in the “small strain” condition.

In this study, the average number of nodes for OP-Sham and OP-OVX-Vehicle were in the order of 640,000 and 380,000. For solving models with a large number of elements, the iterative solvers, in general, require less machine memory than the direct solver. In ABAQUS 6.10.1, a new iterative solver based on Krylov method was released [DS Simulia 2011]. This iterative solver plus symmetric matrix storage method was utilized in our analysis. The performance was much improved compared with the direct sparse solver in terms of memory usage. The duration of linear analysis with half-million nodes utilizing the iterative solver was approximately half an hour on a Windows Vista® desktop with 2 CPUs (Intel Xeon 3.20GHz). Resultantly, the analysis time of each job was acceptable and enabled the submission of batch jobs.

#### *Material properties of FE model*

A limitation of our study was ignoring the mapping of material properties according to different HU or gray values. The Young's modulus in each

trabecular can be correlated with values of HU [Ciarelli et al. 1991]. However, several studies on rat vertebrae of OVX ( $0.91 \pm 0.13 \text{ GPa}$  and  $21.01 \pm 2.48 \text{ GPa}$ ) and sham ( $0.90 \pm 0.09 \text{ GPa}$  and  $22.03 \pm 2.44 \text{ GPa}$ ) groups showed no significant difference in the hardness and elastic modulus [Guo and Goldstein 2000; Jämsä et al. 2002]. Thus, our study focused on the stiffness changes contributed by the alterations of trabecular bone microarchitecture. Hence, the same material properties were assigned to the two groups. If further mechanical analysis was to be required, such as permanent deformation, viscosity or time effect and crack propagation, then material properties would need to be assigned specifically, and nonlinear FEA could be applied.

#### **Future application of the results in our study**

The comparisons of structural parameters to bone stiffness in our study revealed that BV/TV, BMD, Tb.Sp, FD and Tb.Pf are correlated to bone stiffness. The first two parameters, BV/TV and BMD, reflect the geometry and material properties of bone, since BMD was calculated from both the geometry and gray scales of the image. The other three indices, Tb.Sp, FD and Tb.Pf, reflect the microstructure of the trabeculae.

#### **4.6. Conclusion**

In this paper, we have presented a simple process by which the stiffness of trabecular bone can be inferred from structural parameters, without the need for computationally exhaustive FEA models. The 2D structural parameters calculated

from Micro-CT analysis reflected the difference in the geometry of the bone between the sham and the OP group. The changes in the following Micro-CT parameters between the two groups were examined and compared to the stiffness obtained from FEA: BV/TV, BMD, Tb.Sp, FD, Tb.Pf and Conn.Dn. Of those six structural parameters, only Conn.Dn was not correlated to the index of stiffness. Values of BV/TV, BMD and FD were positively related to the stiffness. Conversely, Tb.Sp and Tb.Pf were negatively related to the stiffness. This process can be readily applied to assess trabecular bone structural changes and quickly infer stiffness, particularly during longitudinal “in-vivo” studies of laboratory rodents, or to assess the effects of drug treatment.

### **Acknowledgments**

This research was funded by the Alberta Osteoarthritis Team Grant, from the Alberta Innovates – Health Solutions (AIHS) Interdisciplinary Team Grant programme.

### 4.7. References

- Bouxsein ML, Boyd SK, Christiansen BA, Guldberg RE, Jepsen KJ, Müller R. 2010. Guidelines for assessment of bone microstructure in rodents using micro-computed tomography. *J Bone Miner Res*, 25(7):1468-1486.
- Ciarelli MJ, Goldstein SA, Kuhn JL, Cody DD, Brown MB. 1991. Evaluation of orthogonal mechanical properties and density of human trabecular bone from

the major metaphyseal regions with materials testing and computed tomography. *J Orthop Res*, 9(5):674-682.

Cohen A, Dempster DW, Müller R, Guo XE, Nickolas TL, Liu XS, Zhang XH, Wirth AJ, van Lenthe GH, Kohler T, McMahon DJ, Zhou H, Rubin MR, Bilezikian JP, Lappe JM, Recker RR, Shane E. 2010. Assessment of trabecular and cortical architecture and mechanical competence of bone by high-resolution peripheral computed tomography: comparison with transiliac bone biopsy. *Osteoporos Int*, 21(2):263-273.

Davis GR, Wong FS. 1996. X-ray microtomography of bones and teeth. *Physiol Meas*, 17(3):121-146.

Diederichs G, Link TM, Kentenich M, Schwieger K, Huber MB, Burghardt AJ, Majumdar S, Rogalla P, Issever AS. 2009. Assessment of trabecular bone structure of the calcaneus using multi-detector CT: correlation with microCT and biomechanical testing. *Bone*, 44(5):976-983.

DS Simulia. ABAQUS 6.10 ANALYSIS VolumeII, 6.10.1 edition, 2011.

Evans FG. 1969. The mechanical properties of bone. *Artif Limbs*, 13(1):37-48.

Guo XE, Goldstein SA. 2000. Vertebral trabecular bone microscopic tissue elastic modulus and hardness do not change in ovariectomized rats. *J Orthop Res*, 18(2):333-336.

Ito M. 2011. Recent progress in bone imaging for osteoporosis research. *J Bone Miner Metab*, 29(2):131-140.

Jämsä T, Rho JY, Fan Z, MacKay CA, Marks SC Jr, Tuukkanen J. 2002.

Mechanical properties in long bones of rat osteopetrotic mutations. *J Biomech*, 35(2):161-165.

Jayakar RY, Cabal A, Szumiloski J, Sardesai S, Phillips EA, Laib A, Scott BB,

Pickarski M, Duong LT, Winkelmann CT, McCracken PJ, Hargreaves R, Hangartner TN, Williams DS. 2012. Evaluation of high-resolution peripheral quantitative computed tomography, finite element analysis and biomechanical testing in a pre-clinical model of osteoporosis: a study with odanacatib treatment in the ovariectomized adult rhesus monkey. *Bone*, 50(6):1379-1388.

Kim CH, Takai E, Zhou H, von Stechow D, Müller R, Dempster DW, and Guo

XE. 2003. Trabecular bone response to mechanical and parathyroid hormone stimulation: the role of mechanical microenvironment. *J Bone Miner Res*, 18(12):2116-2125.

Kinney JH, Haupt DL, Balooch M, Ladd AJ, Ryaby JT, Lane NE. 2000. Three-

dimensional morphometry of the L6 vertebra in the ovariectomized rat model of osteoporosis: biomechanical implications. *J Bone Miner Res*, 15(10):1981-1991.

Kinney JH, Ryaby JT, Haupt DL, Lane NE. 1998. Three-dimensional in vivo

morphometry of trabecular bone in the OVX rat model of osteoporosis. *Technol Health Care*, 6(5-6):339-350.

Liu XS, Zhang XH, Sekhon KK, Adams MF, McMahon DJ, Bilezikian JP, Shane

E, Guo XE. 2010. High-resolution peripheral quantitative computed

- tomography can assess microstructural and mechanical properties of human distal tibial bone. *J Bone Miner Res*, 25(4):746-756.
- Macneil JA, Boyd SK. 2008. Bone strength at the distal radius can be estimated from high-resolution peripheral quantitative computed tomography and the finite element method. *Bone*, 42(6):1203-1213.
- Mazurkiewicz A, Topoliński T. 2009. Relationships between structure, density and strength of human trabecular bone. *Acta Bioeng Biomech*, 11(4):55-61.
- Rhee Y, Hur JH, Won YY, Lim SK, Beak MH, Cui WQ, Kim KG, Kim YE. 2009. Assessment of bone quality using finite element analysis based upon Micro-CT images. *Clin Orthop Surg*, 1(1):40-47.
- Rizzoli R, Chapurlat R, Laroche JM, Krieg M, Thomas T, Frieling I, Boutroy S, Laib A, Bock O, Felsenberg D. 2012. Effects of strontium ranelate and alendronate on bone microstructure in women with osteoporosis. *Osteoporos Int*. 23:305- 315.
- SkyScan. Structural parameters measured by the SkyScan™ CT-analyser software, 2009.
- van Rietbergen B, Majumdar S, Pistoia W, Newitt DC, Kothari M, Laib A, Rügsegger P. 1998. Assessment of cancellous bone mechanical properties from micro-FE models based on Micro-CT, pQCT and MR images. *Technol Health Care*, 6(5-6):413-420.
- Vilayphiou N, Boutroy S, Szulc P, van Rietbergen B, Munoz F, Delmas PD, Chapurlat R. 2011. Finite element analysis performed on radius and tibia HR-

pQCT images and fragility fractures at all sites in men. *J Bone Miner Res*,  
26(5):965-973.

Zannoni C, Mantovani R, Viceconti M. 1998. Material properties assignment to  
finite element models of bone structures: a new method. *Med Eng Phys*,  
20(10):735-740.

## **Chapter 5**

# **Strontium Drug Treatment in Osteoporosis Results in the Bias of Bone Mineral Density by X-ray Imaging**

---

The contents of this chapter have been written as a manuscript for journal submission.

## 5.1. Abstract

**Purpose:** The purpose of this study was to: (1) determine the degree of Sr bias of bone mineral density (BMD); (2) verify the amount of strontium (Sr) in bone after Sr drug treatment; and (3) develop a relationship to adjust the BMD to eliminate the bias attributable to Sr content.

**Methods:** Eleven of the twenty one 3-month old female Sprague Dawley rats used in this study were ovariectomized (OVX). OVX rats were dosed with strontium ranelate ((SrR) [Protos®] 5 x 900 mg/kg/wk po) and designated OVX-highSrR (n=11). The remaining rats were sham-operated, dosed with SrR (5 x 225 mg/kg/wk po) and designated Sham-lowSrR (n=10). Further ten sham-operated rats (Sham; n=10) were used as age-matched controls and received no drug treatment. After 12 weeks, all rats were euthanized and the left femur and tibia were dissected. Hydroxyapatite (HA) and Sr-HA phantoms were constructed to gauge the bias of Sr under micro-computed tomography (Micro-CT) and dual energy X-ray absorptiometry (DXA). Both imaging systems were employed to evaluate bone morphometry and BMD. A series of Sr-Ca solutions with different ratios of Sr to Ca were used to calibrate BMD relative to Sr concentration. An equation was derived from the BMD of Sr-Ca solutions as a means for adjusting the BMD of Sr-laden bone.

**Results:** By Micro-CT imaging, OVX-highSrR ( $0.89 \pm 0.04 \text{g/cm}^3$ ;  $75.08 \pm 3.98\%$ ) had significantly higher ( $p < 0.05$ ) BMD values than those for Sham ( $0.80 \pm 0.04 \text{g/cm}^3$ ;  $73.02 \pm 3.70\%$ ), but not for measurements of bone volume/tissue volume (BV/TV). OVX-highSrR showed similar values to Sham-lowSrR

( $0.88 \pm 0.02 \text{g/cm}^3$ ;  $79.05 \pm 1.58\%$ ) for BMD, but was significantly less ( $p < 0.05$ ) in bone volume/tissue volume (BV/TV). The Sr/(Sr+Ca) mole% of the femur and tibia was  $0.01 \pm 0.00$  in Sham,  $0.38 \pm 0.06$  in Sham-lowSrR and  $1.41 \pm 0.23$  in OVX-highSrR. The equation for adjusting BMD of Sr bone was determined as follows:  $\text{true BMD} = (16.023 \times \text{nominal BMD}) / (16.023 + \text{nominal BMD})$ . By DXA, OVX-highSrR ( $0.11 \pm 0.02 \text{g/cm}^2$ ) had significantly increased ( $p < 0.05$ ) BMD (Sham:  $0.09 \pm 0.02 \text{g/cm}^2$ ; Sham-lowSrR:  $0.09 \pm 0.01 \text{g/cm}^2$ ) among all groups. Surprisingly, however, the BV/TV of OVX-highSrR was not significantly higher than the others as measured by Micro-CT.

**Conclusions:** Elemental Sr was readily incorporated in bone following treatment with high-dose SrR and results in the bias of elevated BMD by X-ray imaging. That bias was confirmed by both Micro-CT and DXA. For every 1 mole% of (Sr/Sr+Ca) in bone, a corresponding increase of  $\approx 6.24\%$  in BMD will result under X-ray imaging. The bias in BMD can be corrected with known values of (Sr/Sr+Ca) mole% of the given bone sample.

## 5.2. Introduction

After menopause, bone thinning is accelerated through the imbalance of the bone formation and resorption along with the estrogen deficiency [The ESHRE Capri Workshop Group 2010]. The bone thinning condition is measured with bone mineral density (BMD) by dual energy X-ray absorptiometry (DXA). The patient is diagnosed with osteoporosis (OP) if the T-score or Z-score of BMD is less than -2.5 [World Health Organization 2003]. Studies indicated that OP leads

to a high risk of fracture, morbidity and mortality [Johnell and Kanis 2006]. For lessening this risk, pharmaceutical scientists are seeking drugs to revert the imbalance of bone actions by either inhibiting bone resorption (e.g. bisphosphonates, hormone replacement therapy, selective estrogen-receptor modulators, and calcitonin) or increasing bone formation (e.g. parathyroid hormone) [ Geusens 2009]. In addition to the highlighted drugs, strontium ranelate (SrR) was reported to have the advantages of both anabolic and anti-catabolic function in-vitro [Ammann et al. 2004]. Although the pharmaceutical mechanism of SrR is unstated scientifically, in phase III studies, SrR was also demonstrated to significantly decrease the relative risk of vertebral fractures by 45% in patients without prevalent vertebral fracture over 3 years [Ortolani and Vai 2006]. Strontium (Sr) has long been known as a bone seeking element replacing calcium (Ca) and integrating into bone as strontium-hydroxyapatite (Sr-HA) by replacing calcium (Ca) elements. During the Sr treatment, the ratio of Sr atoms can be up to 0.5 of 10 Ca in mineral crystals [Li et al. 2010]. This is ascribed to the divalent nature and similar chemical properties of Sr and Ca which are both alkaline earths in the periodic table. Those two elements are divalent cations and have comparable atomic diameters (Ca=194pm, Sr=219pm). From all above, Sr drug has proven positive for bone actions in laboratory tests and reducing fractures in clinical trials. However, clinicians and researchers are still concerned about diagnostic decisions being reached from BMD measurements if the patient was given medications with SrR [Blake and Fogelman 2007].

The concern about diagnosis after taking SrR for OP patients is that Sr will attenuate more X-ray photons than Ca, which is presumed to be the main composition of bone minerals. When X-rays pass through bone, the attenuation is subjected to the photoelectric effect and Compton effect [Blake and Fogelman 2007]. In the photoelectric effect, the incident X-ray photon knocks out an electron attached to the nucleus and translates the remaining energy to the kinetics of the electron. In the case of the Compton effect, the residual energy scatters subsequent to the ejection of an electron. By both means X-rays are attenuated during the interaction with matter. The attenuating energy varies with the binding energy between the electron and nucleus. The binding energy increases with increasing atomic number. Accordingly, Sr ( $Z=38$ ) attenuates more X-ray photons than Ca ( $Z=20$ ) does. Therefore, Sr attenuates more signals than Ca under X-ray imaging methodologies such as micro-computed tomography (Micro-CT) imaging and DXA.

The principles of measuring BMD are different between Micro-CT and DXA. Both methodologies take the hydroxyapatite bone as the standard. As for Micro-CT imaging, BMDs were measured by comparing sample images with phantoms of known BMD [SkyScan 2009]. The phantoms were made of hydroxyapatite (HA) and resin. Regarding DXA, BMD was derived from equations consisting of the presumed mass attenuation coefficient of each component (lean, fat, bone etc.) under two X-ray energies [Blake and Fogelman 1997]. The mass attenuation coefficient was also of HA bone. From the above, the effect of Sr atoms was not

considered in both measurements. The bias of BMD is predictable while imaging Sr bone by X-ray.

This issue of BMD has been debated after the starting of SrR at OP, since BMD is widely utilized as the clinical gold standard to diagnose bone conditions. It was demonstrated that every 1 mole% of Sr results in 10% overestimation of BMD by DXA and very little difference of it at bone mineral content (BMC) and BMD [Nielsen et al. 1999]. This overestimation is both theoretically and experimentally that the effect of bone strontium on BMD measurements is different on distinctive DXA systems [Liao et al. 2010]. If the Sr content of the measured bone is known, DXA can be carried out in the presence of Sr bone, and later be interpreted as calcium hydroxyapatite equivalent [Nielsen et al. 1999]. Nonetheless, there are arguments about the necessity to adjust BMD for the Sr content of bone [Bärenholdt et al. 2009; Belissa-Chatelain et al. 2009]. Thus, this issue should be evaluated in terms of the bone microarchitecture. Our study included the X-ray imager, and Micro-CT, to assist in the explaining results by DXA. In this way, both the microarchitecture and BMD are measured by Micro-CT imaging and then compared to the BMD by DXA. The bone volume to tissue volume (BV/TV; %) [Bouxsein et al. 2010] by Micro-CT can help to determine if the biased BMD is a result of an elevated BV/TV.

In summary, the purposes of this study were to: (1) prove that Sr results in the bias BMD; (2) verify the amount of Sr incorporated into the bone after Sr drug treatment; and (3) adjust the BMD to eliminate the bias.

### 5.3. Materials and Methods

#### **Animals**

The protocol pertaining to the following procedures and aspects of the study was approved by the University of Alberta animal care and ethics committee. A cohort of twenty one 3-month old female Sprague Dawley rats were obtained from Charles River and maintained at the University of Alberta Biosciences Animal Services Facility. Eleven of the 21 rats were ovariectomized (OVX) before arriving at the facility by Charles River. The OVX rats were dosed with strontium ranelate ((SrR) [Protos®] 5x900mg/kg/wk p.o.) and designated OVX-highSrR (n=11), in order to potentially bias BMD measurements by X-ray imaging due to the unusually high Sr content in bone. The remaining ten rats were sham operated, dosed with SrR (5x225mg/kg/wk p.o.) and designated Sham-lowSrR (n=10). Ten ages matched and sham operated rats (Sham; n=10) were included in this project as control animals (i.e., without strontium treatment). All rats were euthanized after 3 months. The left femur and tibia of each rat were dissected fresh and cleaned off soft tissue, wrapped individually with 70% ethanol dampened paper towel and stored frozen at -20°C for subsequent analyses. Toenail samples were taken from hind paws in order to determine the mole percentage of (Sr/Sr+Ca) by inductively coupled plasma mass spectrometry (ICP-MS).

The purpose of this project was to validate the Sr in bone, which results in the bias of BMD. The BV/TV of other groups for comparisons should be larger than or equal to the group (OVX-highSrR) which has the highest concentration of Sr in

bone. Thus, the Micro-CT imaging was done to verify the requirements of BV/TV (OVX-highSrR  $\leq$  Sham; OVX-highSrR  $\leq$  Sham-lowSrR) before subsequent analysis. [View the section: Micro-CT imaging]

### **Hydroxyapatite (HA) and Sr-HA (strontium-hydroxyapatite) Phantoms**

Volumetric imaging phantoms were made to mimic bone samples with varying ratios of strontium content while imaging by DXA and Micro-CT, and to further validate the feasibility of recognizing the higher attenuation of Sr over Ca. Phantom dimensions were  $\approx$  PI x 4 mm x 40 mm, which approximated the dimensions of the femur and tibia of rats. HA phantoms of BMD 250mg/cm<sup>3</sup> and 750mg/cm<sup>3</sup> were made of resin (Epo-Thin<sup>®</sup>, Buehler Ltd., Lake Bluff IL) and HA powders (hydroxyapatite, Sigma-Adrich, St. Louis MO, US). In contrast to pure HA containing phantoms, Sr-HA phantoms contained Sr to Ca mole ratio of 0.5 to 9.5. We used SrCO<sub>3</sub> (strontium carbonate, Sigma-Adrich, St. Louis MO, US) as the Sr source.

### **Sr-Ca Solutions**

A series of Sr-Ca solutions with different Sr/(Sr+Ca) mole% (Note: “mole%” was written as “%” in the following content) and concentrations were made by dissolving SrCO<sub>3</sub> and CaCO<sub>3</sub> powder in concentrated nitric acid and Milli-Q water. The concentration of CaCO<sub>3</sub> in each solution was determined according to the moles of Ca derived from the BMD 200, 300 and 400 mg/cm<sup>3</sup> (labelled with A-200, A-300 and A-400). Conforming to the CaCO<sub>3</sub> solutions, Sr-CaCO<sub>3</sub> solutions were made with the equivalent of total mineral atoms but with the mole ratio of Sr to Ca equalling 0.5 to 9.5. The samples were labelled with B-200, B-

300 and B-400. Once the A and B series of samples were prepared, A-200 and B-200 were mixed with the different percentage of volume to make Sr-Ca-200 solutions (i.e. 10% of B-200 was mixed with 90% of A-200 in a 1mL Eppendorf<sup>®</sup> tube, and labelled as 200-1. It means 10% of B in the solution with the identical moles of mineral atoms to BMD 200mg/cm<sup>3</sup>). The same procedure was done for Sr-Ca-300 and Sr-Ca-400. The final Sr-Ca solutions were listed in [Table 5-1].

Table 5-1 Sample list of Sr-Ca solutions (Note: 200-1:10 % of B at equivalent minerals to BMD 200g/cm<sup>3</sup> and so on.)

Content	Samples		
SrCO <sub>3</sub> (B)	200-10	300-10	400-10
60%A+40%B	200-4	300-4	400-4
80%A+20%B	200-2	300-2	400-2
90%A+10%B	200-1	300-1	400-1
CaCO <sub>3</sub> (A)	200-0	300-0	400-0

### Micro-CT Imaging

#### *Femur and Tibia*

Femur and tibia were thawed at room temperature for two hours, wrapped with 70% ethanol soaked paper towel and stored individually in Falcon<sup>®</sup> tubes in 70% ethanol to avoid air bubbles in the tube. Micro-CT imaging was conducted for the entire femur and tibia under settings of 85kV, 18μm and 294μA using a 1.0mm aluminium filter. After scanning, projected images of the samples were reconstructed using vendor supplied software (Nrecon 1.6.1.5, Bruker-microCT, Kontich BE). Vendor morphometric software (CTAn 1.10.0.1, Bruker-microCT, Kontich BE) was then used to analyze BV/TV (%), BMC (gram) and BMD (g/cm<sup>3</sup>) against the vendor-supplied bone phantoms of known BMD (0.25g/cm<sup>3</sup>)

and  $0.75\text{g/cm}^3$ ) in order to calibrate BMD values from Hounsfield units. The samples were stored in the same ethanol filled Falcon<sup>®</sup> tubes after Micro-CT imaging for DXA at a later stage.

#### *HA and Sr-HA phantoms*

Both HA and Sr-HA phantoms were scanned following the procedures for femur and tibia, using identical imager settings.

#### *Sr-Ca solutions*

The fifteen Sr-Ca solutions were scanned at three different X-ray energies, namely 38kV, 62kV and 85kV, at a resolution of  $18\mu\text{m}$  and current of  $294\mu\text{A}$ . The 38kV and 62kV energies are those used by DXA. 85kV is the energy commonly used in the Micro-CT imaging of rat bone. The BMD of each sample was then calculated using vendor bundled software. The actual (Sr/Sr+Ca)% of Sr-Ca solutions was measured by ICP-MS following the Micro-CT imaging evaluation.

### **DXA**

The femur and tibia samples were taken out of their Falcon<sup>®</sup> tubes and dried at room temperature. Both femur and tibia of each rat were placed on rice (to approximate soft tissue density, as is the industry standard) in a Petri dish for DXA analysis (Prodigy, GE Healthcare). The femur and tibia were scanned together, for a total of ten repeats. The BMC (grams), BMD ( $\text{g/cm}^2$ ) and projected areas ( $\text{cm}^2$ ) were recorded. Following scanning, the samples were stored in Falcon<sup>®</sup> tubes with 70% ethanol for subsequent analyses.

## ICP-MS

Bone samples were dried in an oven at 100°C for 8 hours and then incinerated in a muffle-furnace at 800°C for 8 hours. The summed weight of femur and tibia before and after incinerations were recorded. All glassware and pipettes used for this experiment were cleaned with 10% nitric acid, rinsed with deionized water and dried at 50°C. Bone ash was digested in 1mL concentrated nitric acid and 1mL hydrogen peroxide and then heated at 80°C for 1 hour to speed the reaction. Samples remained at room temperature overnight. The total volumes of each sample were recorded by weight before and after the reaction. Rat toenail samples were collected and cleaned with acetone in an ultrasonic bath for 1 hour to remove potential surface contaminants. The samples were drained free of solvent and dried at room temperature for half an hour. Toenail samples were digested to completion in nitric acid and hydrogen peroxide. The Sr/(Sr+Ca)% was measured by ICP-MS (Elan6000, PerkinElmer Waltham, MA) by evaluating ions of Ca<sup>44</sup> and Sr<sup>86</sup>. A calibration curve was constructed from Sr and Ca solutions using a matrix of nitric acid. The measurement range of the standard solutions was between 0.25±0.03ppm ~1.00±0.03ppm for Ca and 5.00±0.03ppb to 20±0.03ppb for Sr. Scandium (Sc) was added to samples and standards as the internal standard, in order to reduce the effects of the matrix alone. Other than bone and toenail samples, the (Sr/Sr+Ca)% of each Sr-Ca solution standard was also measured by ICP-MS.

## Statistics

All statistical evaluations were performed using PASW® Statistics 17.0. Results were shown in bar plots as mean  $\pm$  standard deviation. The independent sample T-test was used for comparing the difference between Sham and OVX-highSrR or Sham-lowSrR and OVX-highSrR. An asymptotic value (p-value)  $<0.05$  was used to evaluate the significance of differences.

## 5.4. Results

### **BMD of HA and Sr-HA Phantom**

Using Micro-CT imaging and DXA, the measured BMD showed significant differences between HA and Sr-HA phantoms. With respect to BMD with an identical number of moles of Sr+Ca (e.g. HA 250 vs. Sr-HA 250), the values for Sr-HA phantoms were 1.39~1.56 times greater than HA phantoms. That multiple is consistent for the same (Sr/Sr+Ca)%. No significant differences were measured at different total moles of Sr+Ca [Figure 5-1]. Our results supported our hypothesis that elemental Sr results in the bias of increased BMD and that the experimental evaluations were feasible on rat bone samples using our X-ray based imaging infrastructure.

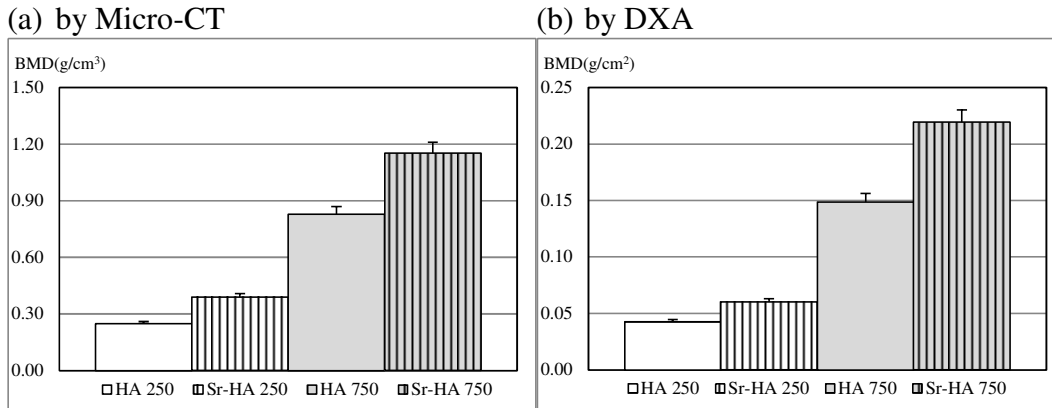


Figure 5-1 BMD of HA and Sr-HA phantoms by (a) Micro-CT and (b) DXA. (HA 250: hydroxyapatite with true BMD of 250mg/cm<sup>3</sup> and so on.) Comparing Sr-HA to HA of the same true BMD, the multiples of BMD are close (1.39~1.56).

### BV/TV and BMD by Micro-CT Imaging

BV/TV% denotes the portion of tissue volume occupied by the binarised solid objects [SkyScan 2009]. It is presented as bone volume per unit tissue volume (cm<sup>3</sup>/cm<sup>3</sup>). If alterations in bone occurred mainly with respect to microarchitecture, but not (or little) in mineralization, then BMD values would show the same trend as BV/TV, since the unit of BMD is grams per cubic centimeter (g/cm<sup>3</sup>). In our samples, the trend of BMD was not the same as BV/TV. OVX-highSrR showed significantly higher BMD than Sham, but not for BV/TV [Figure 5-2(a)]. Comparing OVX-highSrR to Sham-lowSrR, BV/TV was significantly higher in Sham-lowSrR than OVX-highSrR, but not for BMD [Figure 5-2(b)]. Those data served as evidence that Sr incorporated into the bone will result in the bias of elevated BMD. According to the results of HA & Sr-HA phantoms, the overestimation of BMD was dependent on (Sr/Sr+Ca) mole%. If the amount of Sr in bone is known, the measured BMD can be adjusted to accounting for the elemental Sr bias.

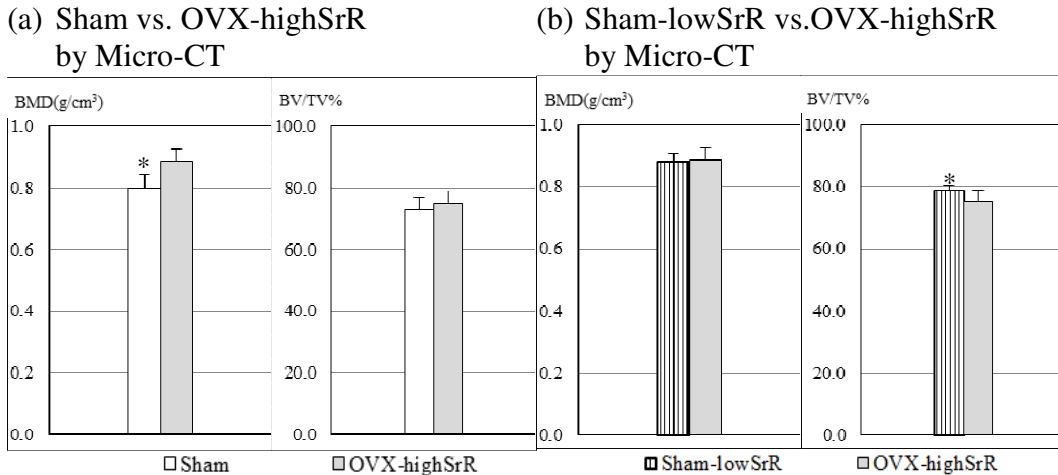


Figure 5-2 BMD and BV/TV of femur and tibia by micro-CT imaging. (a) Sham vs. OVX-highSrR and (b) Sham-lowSrR vs. OVX-highSrR. (\* $p < 0.05$ , the value is significant to OVX-highSrR.) The trends of BV/TV and BMD are different between groups. This indicates the bias of BMD resulting from strontium.

### Sr Determination by ICP-MS

Regarding the bone ash, OVX-highSrR was measured with the highest (Sr/Sr+Ca) mole% among all groups. The (Sr/Sr+Ca) mole% was  $0.01 \pm 0.00$  in sham,  $0.38 \pm 0.06$  in Sham-lowSrR and  $1.41 \pm 0.23$  in OVX-highSrR [Figure 5-3(a)]. The high (Sr/Sr+Ca) mole% in OVX-highSrR demonstrated the high Sr content of that bone and the subsequent effect upon BMD. Knowing the (Sr/Sr+Ca) %, the nominal BMD can be adjusted based upon the results of our Sr-Ca solution standards.

For the toenail samples, (Sr/Sr+Ca)% was  $0.39 \pm 0.06$  in sham,  $1.86 \pm 0.84$  in Sham-lowSrR, and  $4.21 \pm 1.71$  in OVX-highSrR [Figure 5-3(b)]. The Sr levels measured in the toenails were relatively higher than for Sr in the femur and tibia. To relate those measurements, a multiplication factor was calculated by dividing the values from toenails by those from bone. That factor was 2.99 comparing “toenails” to “femur and tibia”.

(a) in femur and tibia by ICP-MS

(b) in toenails by ICP-MS

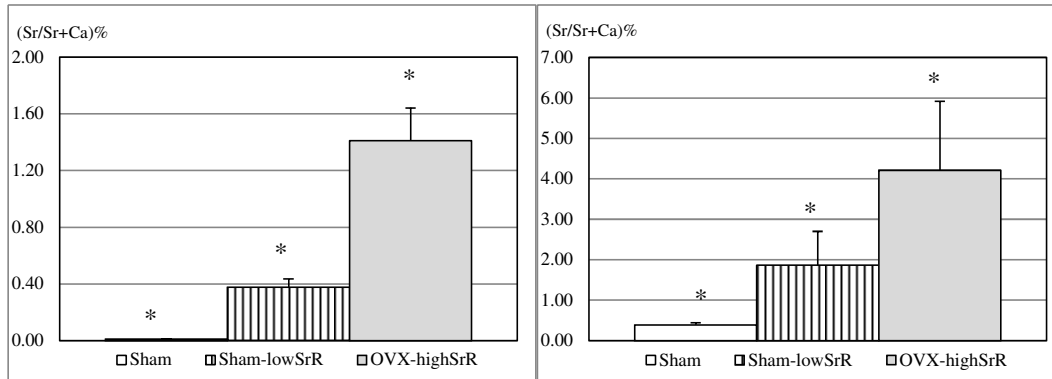


Figure 5-3 (Sr/Sr+Ca)% in (a) femur and tibia and (b) toenails of rats. (\*p<0.05, the value is significant to others.)

### The Equation to Adjust BMD

The volumetric BMD measured by Micro-CT imaging of Sr-Ca solutions and their (Sr/Sr+Ca)% were plotted as curves [Figure 5-4(a)]. No difference was found by scanning at different X-ray energies. However, accompanying the increasing BMD in Ca-solutions (e.g. 200-0, 300-0 and 400-0), the slope of the curve decreased slightly. A regression analysis was performed to determine the relationship between the BMD of Ca-solutions and slopes [Figure 5-4(b)]. The regression curve was represented by a power equation,  $y'=16.023x^{r-1.047}$  (Note:  $y'$ =slope,  $x'$ =BMD of Ca-solutions). For deriving the equation of BMD (x-axis) and (Sr/Sr+Ca)% (y-axis) in [Figure 5-4(a)], let us assume the equation is  $y=(16.023x^{r-1.047})x+R$  (Note:  $x$ =BMD( $g/cm^3$ ),  $y$ =(Sr/Sr+Ca)%,  $R$ =unknown). For any  $x'$ , if  $y=0$ , then  $R=-(16.023x^{r-1.047})x'$ . Therefore, the equation for the curve of BMD and (Sr/Sr+Ca) % can be represented as follows.

$$y = (16.023x^{r-1.047})x - (16.023x^{r-1.047})x' \quad (\text{Equation 1})$$

$$y = (\text{Sr/Sr+Ca})\%$$

$x$  = nominal BMD ( $\text{g}/\text{cm}^3$ ; BMD measured by Micro-CT imaging)

$x'$  = true BMD ( $\text{g}/\text{cm}^3$ ; BMD with the equivalent of Ca)

In Equation 1, the nominal BMD can be measured by X-ray imaging and the (Sr/Sr+Ca)% determined by ICP-MS, then the true BMD can be calculated. The exponent, -1.047, was very close to -1 in the equation. Let us simplify the equation by replacing -1.047 with -1 (Equation 2), and then check the difference of True BMD between Equation 1 and Equation 2.

$$y = (16.023x^{-1})x - 16.023 \quad (\text{Equation 2})$$

Our calculation confirmed that within a range of nominal BMD (0.00~1.50  $\text{g}/\text{cm}^3$ ) and (Sr/Sr+Ca)% (0~10%), the differences of derived true BMD by Equation 1 and Equation 2 were less than or around  $1\text{E}-3$ . Therefore, Equation 2 was used for the following calculations. The ratio of nominal BMD( $x$ ) over true BMD( $x'$ ) was denoted as Equation 3.

$$x/x' = (y + 16.023) / 16.023 \quad (\text{Equation 3})$$

From Equation 3, the ratio was only dependent on (Sr/Sr+Ca)%. This agreed with the results we observed at BMD of HA and Sr-HA phantoms.

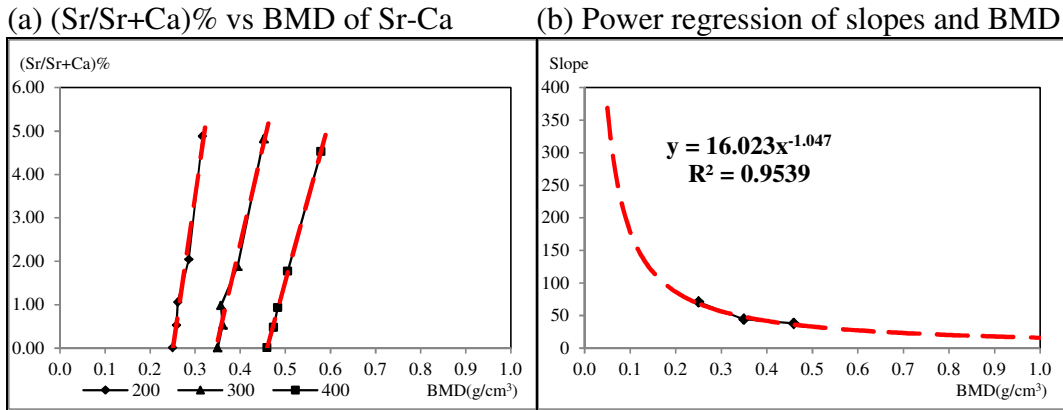


Figure 5-4 (a) Nominal BMD vs. (Sr/Sr+Ca)% of Sr-CA solutions (No difference was found by scanning under different X-ray energies). (b) The regression curve of the curve slopes in (a) and BMDs of Ca-solutions ((Sr/Sr+Ca)%=0).

### Adjusting BMD Measured by Micro-CT Imaging

By applying Equation 2 to adjust the BMD measured by Micro-CT imaging, the adjusted BMD can be seen in [Figure 5-5]. When comparing the adjusted BMD with BV/TV(%), both tendencies were now identical. Thus, our method had successfully corrected for the bias introduced by the denser Sr atom.

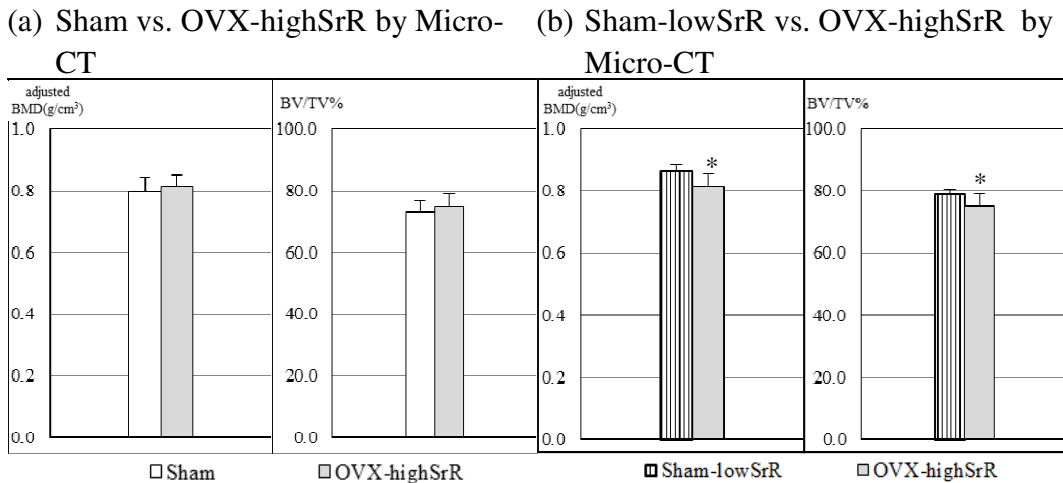


Figure 5-5 Adjusted BMD & BV/TV% of femur and tibia by Micro-CT imaging. (a) Sham vs. OVX-highSrR and (b) Sham-lowSrR vs. OVX-highSrR (\*: p< 0.05, the value is significant to OVX-highSrR.)

### Results by DXA

In order to relate the results between DXA and Micro-CT, BMD was converted to BMC (gram). In addition to comparing BMC by two imaging methods, the ash weights of bone samples were also compared to validate BMC. The results showed an identical trend for all three methods [Figure 5-6], suggesting both imaging methods were reliable in measuring BMC. As  $BMC = BMD * TV$  (Note: TV=tissue volume), if TV were to be constant, BMC would be proportional to BMD. Therefore, Equation 3 can also be applied in order to adjust BMC. Before that adjustment, BMC showed significant differences between the groups. After the adjustment, only the BMC of sham showed a significant difference compared to other groups. That confirmed the denser Sr atom resulted in the bias of increased DXA values.

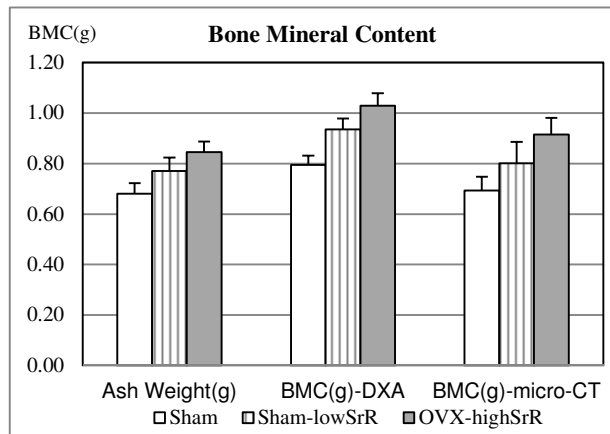


Figure 5-6 Bone mineral content (BMC) measured by different methods, measuring ash weight, DXA, and Micro-CT. All three methods showed identical trends between groups.

Furthermore, it was now possible to calculate BMD from the adjusted BMC by dividing adjusted BMC with the area. Statistically, the BMD did not show differences after the adjustment. OVX-highSrR still showed the highest BMD in comparison to Sham or Sham-lowSrR [Figure 5-7].

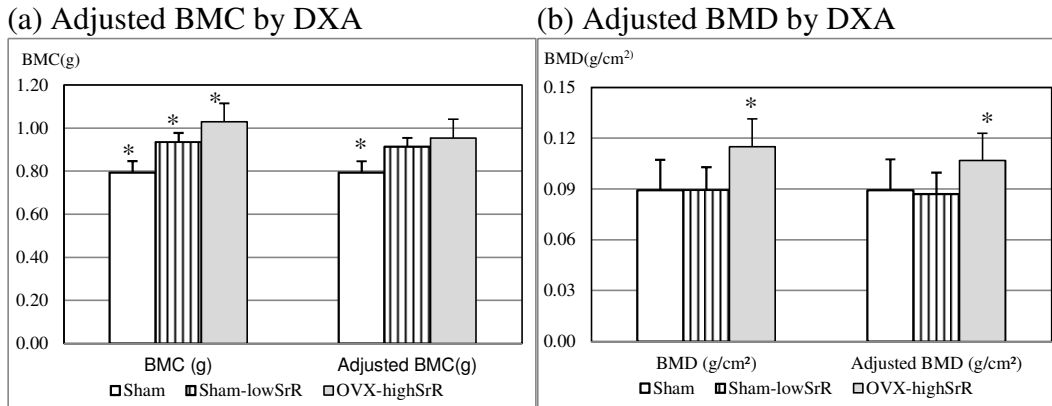


Figure 5-7 (a) BMC and (b) BMD measure by DXA before and after adjustment. (\*p < 0.05, the value is significant to others.)

## 5.5. Discussion

We have shown that elemental Sr incorporation in bone will result in the bias of elevated BMD by X-ray imaging. In contrast to volumetric BMD obtained by Micro-CT imaging, areal BMD obtained by DXA is in the unit of grams per square centimeter. Therefore, areal BMD is highly sensitive to sample size. Our samples were rat bones, with areas in the order of 4 x 40 mm<sup>2</sup> for each femur or tibia. The dimension of the DXA detection cell is ~ 1.2 x 0.6 mm<sup>2</sup>. Comparatively, the detection cell size may not be fine enough to capture the exact area being measured. Therefore, while converting BMC to areal BMD, the results were not altered. Nonetheless, OVX-highSrR showed the highest BMD by DXA but not the highest BV/TV% by Micro-CT imaging, in comparison to Sham and Sham-lowSrR (which already suggested the bias of BMD by Sr content). If the bias was not an issue, the results of BV/TV should be the same as the results of BMD.

Another point worthy of discussion was the index of (Sr/Sr+Ca)% measured in bone. In our study, toenails were collected as a non-invasively obtained reference

tissue, in order to measure  $(\text{Sr}/\text{Sr}+\text{Ca})\%$ . Thus, it may be possible to determine  $\text{Sr}/\text{Sr}+\text{Ca}$  by testing the nail clippings from patients undergoing long-term Sr therapy in the clinic. Once the relationship between different bony sites and nail content are established,  $(\text{Sr}/\text{Sr}+\text{Ca})\%$  in nail samples may serve as useful biomarkers of Sr in bone.

Although the  $(\text{Sr}/\text{Sr}+\text{Ca})\%$  is necessary to perform the correction for BMD, the approximate maximum value of the overestimation can be deduced without it. In the literature, the atomic ratio of  $\text{Sr}/\text{Sr}+\text{Ca}$  is up to 0.5/10 during Sr drug treatment [Li et al. 2010]. That ratio is reasonable scientifically according to the diameter of Sr and Ca atoms. Since the diameter of Sr atom is larger than Ca atom, substitution by the Sr atom may limit further Sr atom fit. Therefore, for the sake of simplicity, we can assume the maximum number of Sr in the Sr-HA crystal is 1. Thus, if the maximum ratio of  $\text{Sr}/\text{Ca}+\text{Sr}$  is 1/10, then  $(\text{Sr}/\text{Ca}+\text{Sr})\% \leq 10\%$ . Applying 10 for  $(\text{Sr}/\text{Ca}+\text{Sr})\%$  in Equation 3, the ratio of Nominal BMD/True BMD is  $\approx 1.6$ . For the longitudinal studies, the BMD measured before and after Sr drug treatments were compared. Applying this logic, if the BMD measured after treatment is 1.6 times that of the BMD measured before treatment, the BMD is clearly increasing. That may result as the maximum bias of BMD ratio is just  $\approx 1.6$  times. Resultantly, that may serve as a reference for BMD measurements of Sr drug dosed patients in the clinic.

Previous studies mentioned that every 1% of  $(\text{Sr}/\text{Sr}+\text{Ca})$  will result in a BMD increase of 10% [Nielsen et al. 1999]. Our study showed that every 1% of  $(\text{Sr}/\text{Sr}+\text{Ca})$  will result in a BMD increase of  $\approx 6.24\%$ . Clearly, that value will vary

depending on the imaging system used [Liao et al. 2010]. The overestimation of BMD may vary somewhat between Micro-CT and DXA. However, in our study, the resolution of the Micro-CT system was relatively finer than that of DXA in the clinic. The BV/TV helped to verify the microstructure of bone. By comparing BV/TV to areal BMD, we could demonstrate the bias of Sr as increased BMD under DXA. For future studies to understand the overestimation of BMD by different X-ray imagers, the process and concept are easy to adapt to each system.

## 5.6. Conclusion

Our study showed that Sr deposition in bone resulted in the bias of increased BMD by Micro-CT imaging and DXA. Based upon our Micro-CT measurements, every 1% of (Sr/Sr+Ca) in bone will increase BMD by  $\approx 6.24\%$ . The BV/TV of bone ascertained by Micro-CT imaging was capable of validating the true BMD of bone. We derived the following equation to correct BMD in bone that has incorporated elemental Sr, as follows:

$$\text{True } BMD = \frac{16.023 \times \text{nominal } BMD}{16.023 + \left(\frac{Sr}{Sr + Ca}\right)\%}$$

## 5.7. References

Ammann P, Shen V, Robin B, Mauras Y, Bonjour J-P, Rizzoli R. 2004.

Strontium ranelate improves bone resistance by increasing bone mass and improving architecture in intact female rats. *J Bone Miner Res.* 19(12):2012–2020

- Bärenholdt O, Kolthoff N, Nielsen ST. 2009. Effect of long-term treatment with strontium ranelate on bone strontium content. *Bone*. 45(2):200–206
- Belissa-Chatelain P, Dupin-Roger I, Cournarie F, Tsouderos Y. 2009. Re: "effect of long-term treatment with strontium ranelate on bone strontium content" by Bärenholdt et al. (*bone*, 2009). *Bone*. 45(5):1024–5; author reply 1026–7
- Blake GM, Fogelman I. 1997. Technical principles of dual energy X-ray absorptiometry. *Semin Nucl Med*. 27(3):210–228
- Blake GM, Fogelman I. 2007. The correction of BMD measurements for bone strontium content. *J Clin Densitom*. 10(3):259–265
- Bouxsein ML, Boyd SK, Christiansen BA, Guldberg RE, Jepsen KJ, Müller R. 2010. Guidelines for assessment of bone microstructure in rodents using micro-computed tomography. *J Bone Miner Res*. 25(7):1468–1486
- Geusens P. 2009. Strategies for treatment to prevent fragility fractures in postmenopausal women. *Best Pract Res Clin Rheumatol*. 23(6):727–740
- Johnell O, Kanis JA. 2006. An estimate of the worldwide prevalence and disability associated with osteoporotic fractures. *Osteoporos Int*. 17(12):1726–1733
- Li C, Paris O, Siegel S, Roschger P, Paschalis EP, Klaushofer K, Fratzl P. 2010. Strontium is incorporated into mineral crystals only in newly formed bone during strontium ranelate treatment. *J Bone Miner Res*. 25(5):968–975

Liao J, Blake GM, McGregor AH, Patel R. 2010. The effect of bone strontium on BMD is different for different manufacturers' DXA systems. *Bone*. 47(5):882–887

Nielsen SP, Slosman D, Sørensen OH et al. 1999. Influence of strontium on bone mineral density and bone mineral content measurements by dual X-ray absorptiometry. *J Clin Densitom*. 2(4):371–379

Ortolani S, Vai S. 2006. Strontium ranelate: an increased bone quality leading to vertebral antifracture efficacy at all stages. *Bone*. 38(2 Suppl 1):19–22

SkyScan. 2009. Structural parameters measured by the SkyScan™ CT-analyser software

The ESHRE Capri Workshop Group. 2010. Bone fractures after menopause. *Hum Reprod Update*. 16(6):761–773

World Health Organization. 2003. Prevention and management of osteoporosis report of a WHO Scientific Group

## **Chapter 6**

# **Material Properties and Elemental Composition of Rat Bone in Correlation with Bone Strength after Treatment with Risedronate or Strontium Ranelate**

---

The contents of this chapter have been written as a manuscript for journal submission.

## 6.1. Abstract

**Purpose:** The purpose of this study was to: 1) observe the changes in bone microarchitecture of rats developing during the treatment period; 2) understand the distribution of new bone formation after treatment; 3) measure the material properties of bone formed before/after drug treatment; 4) apply the measured material properties to calculate the bone strength; finally, 5) provide evidence to explain the possible outcomes of long-term treatment of bisphosphonates (BPs) and strontium ranelate (SrR).

**Methods:** Forty eight rats were used for this study. Thirty six rats were ovariectomized (OVX) and assigned to one of three groups (n=12/group), designated OVX-lowSrR, OVX-highSrR and OVX-lowSrR+RIS. The remaining twelve rats were sham-operated and designated as Sham-lowSrR (n=12). The rats in the lowSrR groups were dosed with SrR ([Protos®]) 5 x 225mg/kg/wk and the highSrR group dosed with SrR 5 x 900mg/kg/wk by oral gavage. The group treated with risedronate (RIS) was dosed 2 x 0.06mg/kg/wk by subcutaneous injection. One mL of whole blood was drawn from the jugular vein of each rat at baseline and again at the study endpoint. All rats were euthanized after three months of treatment. The lumbar vertebrae L5 & L6 from each rat, as well as L4 and the left hind limb long bones were dissected. Serum levels of parathyroid hormone (PTH), Ca and Sr concentration were measured using an immunoassay kit and inductively coupled plasma spectroscopy (ICP-MS) respectively. Longitudinal in-vivo micro-computer tomography (Micro-CT) scans were undertaken at baseline, 4 wk, 8 wk and 12 wk intervals to assess changes in bone

microarchitecture, notably bone volume/tissue volume (BV/TV). Electron probe micro analysis (EPMA) was conducted to detect the elemental composition and distribution of bone following the given drug regimen. K-edge subtraction Synchrotron Micro-CT (KES-SR $\mu$ CT) imaging methodology was developed and applied in order to show bone incorporated Sr distribution three dimensionally. By referencing EPMA spatial distribution maps of elemental bone composition, nanoindentation tests were subsequently performed on regions of bone formed before and after drug treatment. Once data for material properties and bone geometry were collected, the vertebral bone stiffness of each rat was calculated by finite element analysis (FEA).

**Results:** In the OVX-highSrR group, there was approximately 2wt% increase of elemental Sr in the newly formed bone without significant changes in the ratio of (Ca+Sr)/P. Following 3 months of treatment, we measured the significant conservation of trabecular bone volume/tissue volume (BV/TV) compared with untreated OVX controls. In contrast, with the OVX-lowSrR+RIS group, BV/TV was rapidly and efficiently conserved within the first month of treatment, but at the expense of reduced new bone formation, as evidenced by Micro-CT and elemental Sr deposition. The combined treatment of laser and RIS significantly reduced the hardness of bone in comparison to both the Sham-lowSrR and OVX-lowSrR groups. Newly formed bone following RIS treatment was measured to have reduced Young's modulus compared with the bone from the other groups, or from bone regions modelled prior to treatment. Regarding bone stiffness, the OVX-lowSrR+RIS group was measured with highest values

among all OVX groups at the 3 month experimental endpoint.

**Conclusions:** This study confirmed that high dose SrR was effective in the conservation of trabecular BV/TV in an OVX rat model of osteoporosis. No significant change in Young's modulus was measured in the OVX-highSrR group, despite the 2 wt% increase of elemental Sr deposited on the bone. This suggested that SrR maintained normal bone stiffness better than untreated bone as early as 3 months following initiation of treatment. On the other hand, RIS was highly effective in the rapid conservation of trabecular BV/TV. However, RIS therapy further resulted in the reduction of new trabecular bone formation. Additionally, Young's modulus and hardness of RIS treated bone was significantly reduced compared to the untreated bone. Accordingly, despite increased trabecular conservation, it is feasible that the mechanical resistance of bone to permanent deformation following RIS treatment may not be as robust as bone treated with SrR, particularly following long-term drug therapy.

## 6.2. Introduction

Bisphosphonates (BPs) are known as the primary treatment for both postmenopausal and secondary osteoporosis (OP) [Chapurlat and Delmas 2006; Keen 2007; Borgström et al. 2010; Drake et al. 2008]. OP is recognized as a bone-thinning disease, as a consequence of the imbalance of bone remodelling activity. To compensate for the inequity, BPs can be taken up by the skeleton to decrease osteoclast-mediated bone resorption [Papapoulos 2008]. Multiple studies have proven that bisphosphonate (BP) treatment for 3 years will significantly reduce

vertebral fracture up to 49% and non-vertebral fracture up to 39% for patients with postmenopausal OP [Harris et al. 1999; Reginster et al. 2000]. However, there have also been several clinical case reports of delayed or absent fracture healing while on alendronate BP treatment, from as early as 3 months to 2 years [Odvina et al. 2005]. In the last few years, several cases of spontaneous atypical sub-trochantric and diaphyseal fracture of patients on BPs in patients on continuous BP therapy for over 5 years have been reported [Shane et al. 2010; Papapoulos 2011; Rizzoli et al. 2011]. Accordingly, the U.S. Food and Drug Administration announced that the atypical fractures may be related to long-term BPs use, although the optimal duration of BP use for OP is unknown [U.S. Food and Drug Administration 2010].

The biomechanical implication of BP mediated “over-suppression” of bone turnover has long been questioned [Mashiba et al, 2001; Wang et al, 2008]. For resolving this question, studies were undertaken from different points of view, such as radiographic features, prodromal pain, clinical OP diagnosis, epidemiology as well as the dose of BPs, in order to explore the possible associations between atypical fractures and the long-term medication with BPs [Rizzoli et al 2011]. The conclusion remains controversial [Papapoulos 2011; Rizzoli et al. 2011; Zhang et al. 2011]. It is suspected that fractures resulted in response to micro-damage and changes in bone quality [Shane et al. 2010] as a consequence of “frozen” bone, which may lead to weakened bone structure, with the added inability to detect those alterations by dual energy X-ray absorptiometry (DXA). Hence, drugs with potent anabolic effect were encouraged to be taken as

either combinations with BPs, or as a monotherapy.

Strontium ranelate (SrR; [Protos®]), which may possess antiresorptive and anabolic properties, is one such option. The dual-action of SrR has been shown *in vitro* by its action in stimulating osteoblast differentiation and function, and ability to decrease osteoclast differentiation as well as function, by disrupting actin cytoskeleton organization [Bonnelye et al. 2008]. In clinical studies, SrR demonstrated antifracture efficacy at both vertebral and non-vertebral bone sites [Seeman 2006]. Notwithstanding those reported treatment effects, the strontium (Sr) element of SrR in itself also serves as a sensitive and useful dynamic tracer capable of detecting the formation of new bone [Krefting et al. 1993], since its chemical properties are similar to that of calcium (Ca). Using Sr as a tracer of bone formation can help us understand the spatial location of newly mineralizing bone following therapeutic drug treatment. As a result, differences in material properties can be measured to validate the hypothesis that the material quality of bone may change following current drug treatment regimens. Additionally, the strength of bone can be calculated by employing finite element analysis (FEA) derived from the trabecular microarchitecture, ascertained by high resolution micro-computed tomography (Micro-CT) imaging.

This study was designed to measure changes in elemental composition and material properties of osteoporotic rat bone after treatment with SrR and BP, to further validate the effects of long-term BP therapy. Hence, the aims of this study were to: 1) observe the changes in bone microarchitecture of osteoporosis (OP) rats during the treatment period; 2) understand the spatial localization and

distribution of new bone formation after treatment; 3) measure the material properties of bone formed before/after drug treatment; 4) apply the measured material properties to calculate the bone strength; and finally 5) provide evidence to help explain possible outcomes of long-term BP and SrR therapy.

### 6.3. Materials and Methods

#### **Animals**

Forty eight 12-week old female Sprague Dawley rats were obtained from Charles River. The ethical use of animals was approved by the ethics committee of University of Alberta. Thirty six of those rats were ovariectomized (OVX) by Charles River before arrival. They were randomly assigned to three groups (n=12/group), named OVX-lowSrR, OVX-highSrR and OVX-lowSrR+RIS. The other twelve rats were sham-operated as controls and assigned to the group, Sham-lowSrR (n=12). According to the group names, the rats in the lowSrR groups were treated with SrR at a dosage of 225mg/kg and the highSrR group were treated with SrR at 900mg/kg by oral gavage five working days per week. The group labelled with RIS was treated with risedronate (RIS) 0.06mg/kg by subcutaneous injection twice per week. Rats were weighed every month in order to calculate the corresponding drug dose during the treatment regimen of 12 weeks. One mL of whole blood was drawn from the jugular vein of each rat at baseline and at the 3 month study endpoint. Blood samples were allowed to clot in 1mL microcentrifuge tubes for 15 minutes at room temperature and were then centrifuged at 10,000 rpm for 5 minutes. The serum supernatant was stored frozen

in fresh tubes in a -30°C freezer. All rats were euthanized after three months of treatment. The lumbar vertebrae 5 & 6 (L5 & L6)) were dissected from every rat. Besides the lumbar vertebra 4 (L4), both the left tibia and femur were dissected from one rat in OVX-highSrR. After dissection, the soft tissues attached to the bone were removed by dissection. The excised L5 was cut in half along the sagittal plane, and then the right half vertebrae were cut in half again along the transversal plane using a precision wafer sectioning saw (IsoMet® 1000, Buehler, Illinois U.S). The pieces of L5 were immersed in acetone for 4 weeks to prepare for subsequent experimentation. All remaining excised bones (other than the L4 and long bones of OVX-highSrR) were wrapped with phosphate buffered saline (PBS) wet paper towels and stored at -30°C for subsequent Micro-CT imaging. The L4 vertebral body and long bones were preserved in 70% ethanol for subsequent synchrotron Micro-CT imaging. The arrangement of samples was illustrated on the chart below [Figure 6-1].

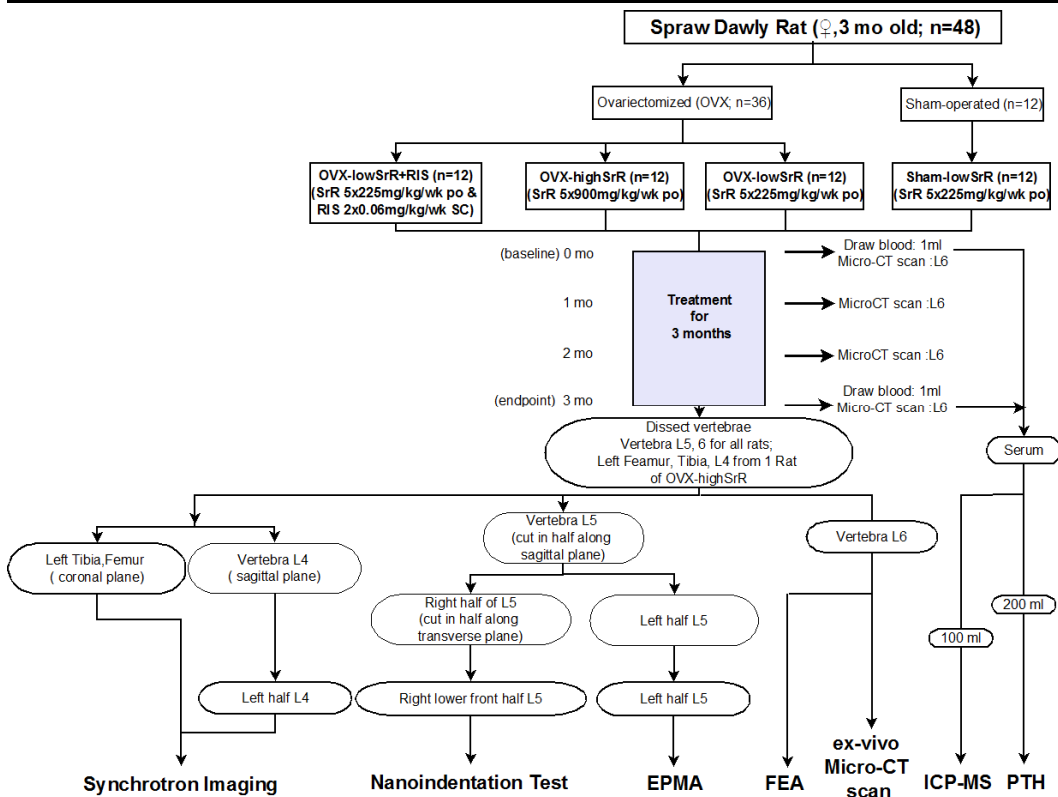


Figure 6-1 The arrangement of animals and bone samples for experiments.

### Parathyroid Hormone (PTH) in Serum by PTH Immunoassay Kit

The PTH level in serum was tested to gauge the influence of PTH upon measured concentrations of Ca and Sr, and following treatment with SrR and RIS. An extraction kit (S-5000, Bachem, Bubendorf Switzerland) was utilized prior to the measurement of PTH to eliminate other potentially interfering substances, such as albumin. Following extraction, the PTH (1-34) assay kit (S-1415, Bachem, Bubendorf Switzerland) was used to determine PTH concentrations in serum.

### Inductively Coupled Plasma Mass Spectrometry (ICP-MS)

Both Ca and Sr concentration in serum were determined using ICP-MS. All the glassware and pipettes used in this experiment were cleaned with concentrated

nitric acid, rinsed with deionized water and dried at 50°C prior to determinations. For each rat, 100µL serum was added to a glass bottle and 1mL nitric acid and 0.5mL hydrogen peroxide added to ensure complete oxidation. Samples were heated at 80°C for one hour until the liquid became clear. Ca and Sr were measured by ICP-MS (Elan6000, PerkinElmer Waltham, MA) by evaluating ions of Ca<sup>44</sup> and Sr<sup>86</sup>. The calibration curve was established from Sr and Ca solutions with a matrix of nitric acid. The measuring range of the standard solutions was between 0.25±0.03ppm ~1.00±0.03ppm for Ca and 5.00±0.03ppb to 20±0.03ppb for Sr. Therefore, each sample was diluted gradually with 1% of nitric acid for measurement. Scandium (Sc) was added to samples and standards as the internal standard to reduce the matrix effect.

### **Micro-Computed Tomography**

The changes in bone microarchitecture during treatment were investigated using in-vivo Micro-CT. The L6 of each rat was scanned every 4 weeks by Micro-CT.

For the settings of Micro-CT scans, please refer to Chapter 5, 5.3.

Excluding the top and bottom growth plates, the vertebral body was segmented out (that segmented bone was designated vertebral column in the following paragraphs). Trabecular and cortical bones were segmented separately from the vertebral column. CTAAn 1.12.0.0 (Bruker-microCT, Kontich BE) was used to analyze the structural parameters of trabecular and cortical bone. For trabecular bone, bone volume/tissue volume (BV/TV; %), trabecular thickness

(Tb.Th; mm), trabecular number (Tb.N; 1/mm) and trabecular separation (Tb.Sp; mm) were reported. For the cortical bone, cortical bone thickness (Ct.Th; mm), cortical bone area (Ct.Ar; mm<sup>2</sup>), total cross-sectional Area (Tt.Ar; mm<sup>2</sup>) and Ct.Ar/Tt.Ar (%) were calculated [Bouxsein et al. 2010].

### **Nanoindentation Test**

The pieces of the L5 vertebral body were removed from acetone and dried in a 40°C oven for 24 hours. Samples were then embedded in epoxy (Epo-Thin®, Buehler, Illinois U.S) and polished gradually to 0.5µm fineness (Thin Section Lab, Geology, University of Alberta, Canada). The indentation was performed along the longitudinal axis of the vertebra. The indentation regions were named “Center” and “Edge” according to the distance (30µm and 150µm respectively) from the cortical bone periosteal surface. That decision was based on the results of our preliminary study, as newly formed bone was seen to deposit on the periosteal surface layer by layer. Thus, superficial bone at the periosteal cortical surface (named “Edge”) was deposited more recently than bone in the center of cortical bone (named “Center”). The nanoindentation test was conducted by TI 900 TriboIndenter (Hysitron Inc., Minneapolis MN) with a Berkovich tip, which was made of diamond. A 3-step, load-hold-unload, with the maximum indentation force of 8000µN was controlled as the input. In every region, thirty indentations were done in two rows with intervals of 15 µm. The displacements upon the force were recorded. The software Triboscan 8 (Hysitron Inc., Minneapolis MN) was used for calculating the reduced modulus (Er) and hardness (H). For converting Er to Young’s modulus (E), the Poisson’s ratio (ν) of the bone was assumed as 0.3.

### **Electron Probe Micro Analysis (EPMA)**

Following the nanoindentation tests, the samples were coated with a carbon film of 20nm thickness for EPMA. Chemical elements, Sr, Ca and phosphorous (P), were then detected by wavelength dispersive spectroscopy (WDS). It was undertaken by JEOL JXA-8800 (JEOL, Tokyo Japan) superprobe. A 15keV of the incident electron beam, 30nA current with 2 $\mu$ m step size was implemented on the half of the sagittal surface. Since the inorganic component of bone is hydroxyapatite (HA;Ca<sub>10</sub>(PO<sub>4</sub>)<sub>6</sub>(OH)<sub>2</sub>) and the treatment may cause depositions of Sr elements in bone, the X-ray lines of P K $\alpha$  , Ca K $\alpha$  and Sr L $\alpha$  were collected. The mineral standards, strontianite for Sr, F-Apatite for P and dolomite for Ca, were used in this experiment.

After the scans for elemental maps, Sr depositions were shown clearly on the following regions: 1) the areas close to growth plates; 2) the free surfaces of cortical and trabecular bone. According to the maps, the quantitative analysis was done in the areas to measure the wt% of Sr, Ca and P. The count time was increased to 20 seconds. A line scan with 20 $\mu$ m intervals was done from the edge of cortical bone toward the center of the bone. The length of the line varied with the samples, as long as it covered both the areas showing relatively more and fewer Sr elements. The background analysis was done to know the continuum X-ray for subtraction later. To correct X-ray signals caused from atomic number (Z; electron backscattering, electron stopping power), absorption (A) and secondary fluorescence (F), a ZAF correction, named PAP correction [Pouchou & Pichoir, 1985] was implemented for post processing. After the quantitative analysis, the

mole ratio of Ca to P, or (Ca+Sr) to P was calculated to present the elemental compositions after drug treatment.

### **Synchrotron Imaging**

The two dimensional distributions of Sr in the cutting surface of bone were detected by EPMA. However, it was not applicable for assessing three dimensional elemental distributions. Therefore, the three dimensional distributions of Sr in bone were further demonstrated by synchrotron K-edge subtraction imaging method [Cooper et al. 2012]. This experiment was completed at the Canadian National Synchrotron Facility, namely, the Canadian Light Source (CLS; Saskatoon, SK, Canada). Samples were dried at room temperature prior to imaging. The principle of this experiment is based on the characteristic binding energy of K shell electrons in Sr elements. A sudden increase in the attenuation coefficient can be detected when the incident energy equals or is slightly higher than the binding energy of K shell electron of the atom. This sudden change of the attenuation coefficient makes an obvious change in the gray scale of images when X-rays pass through matter containing elemental Sr. Since the energy of the Sr K-edge is  $\approx 16.15\text{keV}$ , samples were scanned with incident energies higher ( $16.16\text{keV}$ ) and lower ( $16.08\text{keV}$ ) than the K-edge energy of Sr. Sr deposition was subsequently visualized on images by subtracting images derived above and below the K-edge against each other. Several different concentrations of Sr solutions (0.00~5.00 wt%) were prepared in order to calibrate Sr concentration. Projection images were obtained and ImageJ1.42q plus LOCI plugin was used to convert the raw files (\*.cxd) from synchrotron imaging to \*.mhd. The mhd files

were imported into Athabasca Recon 1.2.2b (Bone Imaging Laboratory, University of Calgary) in order to reconstruct and align the separate sets of projection images. After that, Avizo 6.3.1 (VSG, Burlington MA USA) was used for image registration, subtraction and three dimensional model creations.

### **Finite Element Analysis**

Finite element models were built for each vertebral body obtained from Micro-CT image geometry. Mimics 14.0 (Materialise, Leuven Belgium) was used to build the finite element models. The element size, 18 $\mu$ m, was the same as the pixel size of the Micro-CT images. The models were meshed with hexahedral elements. The meshes were then imported into ABAQUS/CAE 6.12 (Dassault Systèmes, Vélizy-Villacoublay France) for further pre-processing. The material properties of the models were assigned with the average E measured in the bony regions designated “Center” and “Edge”, which were derived from nanoindentation testing. According to the results of the nanoindentation tests, OVX-lowSrR+RIS showed significantly different values between “Center” and “Edge”. Therefore, for OVX-lowSrR+RIS, the volume of “Edge” was segmented out and assigned with the E measured for the “Edge” regions. The remaining volume in OVX-lowSrR+RIS was assigned with the E measured for the “Center” regions. For other groups, since there was no significant difference between “Center” and “Edge”, the model was assigned with the average E for both the “Center” and “Edge” for each sample. All models were set to 0.3 for the Poisson’s ratio. For boundary conditions, the bottom of the model was fixed and the top of the model was loaded with 5% strain for each sample. The analysis was executed

in ABAQUS 6.12 (Dassault Systèmes, Vélizy-Villacoublay France) as a linear analysis with the element type of C3D8. The iterative method was selected as the solver for the large model and linear analysis. After calculation, the total reaction force on the bottom of the models was reported. To derive measures of bone strength, the stiffness (k) of each model was calculated by dividing the force to the displacement.

### **Statistics**

Statistical evaluations were performed using PASW® Statistics 17.0. The results were shown as mean  $\pm$  standard deviation. For comparing results at the same time points among groups, the One-Way ANOVA was used for evaluating significant differences. If significant differences were measured, the LSD test was used for post hoc multiple comparisons, with an asymptotic value (p-value) set to  $<0.05$ .

## **6.4. Results**

### **Serum Biochemistry**

OVX-highSrR showed significantly higher ( $p<0.05$ ) Sr concentration in serum compared to other groups (Sham-lowSrR:  $2.15\pm 0.31$  (mg/L); OVX-lowSrR:  $1.58\pm 0.35$  (mg/L); OVX-highSrR:  $34.72\pm 5.92$  (mg/L); OVX-lowSrR+RIS:  $2.98\pm 0.59$  (mg/L)) at the experimental endpoint. No significant differences were found in serum Ca concentrations irrespective of treatment. Despite increased serum Sr concentration, we did not measure corresponding

increases in PTH in any of the treatment groups at the experimental endpoint.

### **Microarchitecture of Bone**

The longitudinal changes in measured Micro-CT structural parameters are presented in [Figure 6-2]. For most parameters, a clear drug effect was witnessed following the first month of treatment. Trabecular BV/TV of all OVX rats decreased, except for the group with RIS treatment. That reduction in BV/TV continued to the experimental endpoint at 3 months post-OVX surgery. OVX-highSrR significantly conserved BV/TV ( $p < 0.05$ ) in comparison to OVX-lowSrR [Figure 6-2 (a)]. The rank order of BV/TV at the end of treatment was: Sham-lowSrR > OVX-lowSrR+RIS > OVX-highSrR > OVX-lowSrR ( $p < 0.05$ ). The trend for all parameters relating to the cortical bone showed a monthly increase, likely as all rats were experiencing appositional growth during the treatment period [Figure 6-2(c)-(f)]. Although net growth increased in all groups, values for OVX-highSrR and OVX-lowSrR were less for Ct.Th than that measured for Sham-lowSrR and OVX-lowSrR+RIS [Figure 6-2 (c)]. High dose SrR treatment did not stop the erosive degradation measured in cortical bone post-OVX. With respect to Ct.Ar, only the RIS treatment group was significantly higher than the values obtained for all other groups. Combining information of Ct.Th and Ct.Ar, the Tt.Ar of Sham-lowSrR was less than for all other groups [Figure 6-2 (e)]. We can conclude that OVX or drug treatment resulted in the resorption of trabecular bone, and that observation was also reflected in the area of cortical bone cross sections. The morphological changes along the given timecourse were illustrated in the three dimensional models rendered from Micro-CT image data sets [Figure

6-3]. At the conclusion of drug treatment, Tb.Sp was significantly lower in Sham-lowSrR and OVX-lowSrR+RIS groups than for both OVX-lowSrR and OVX-highSrR [Figure 6-4 (b)]. In most groups, Tb.Th did not change significantly over the course of treatment. Only OVX-highSrR exhibited a trend towards increased Tb.Th compared to all other groups [Figure 6-4 (a)].

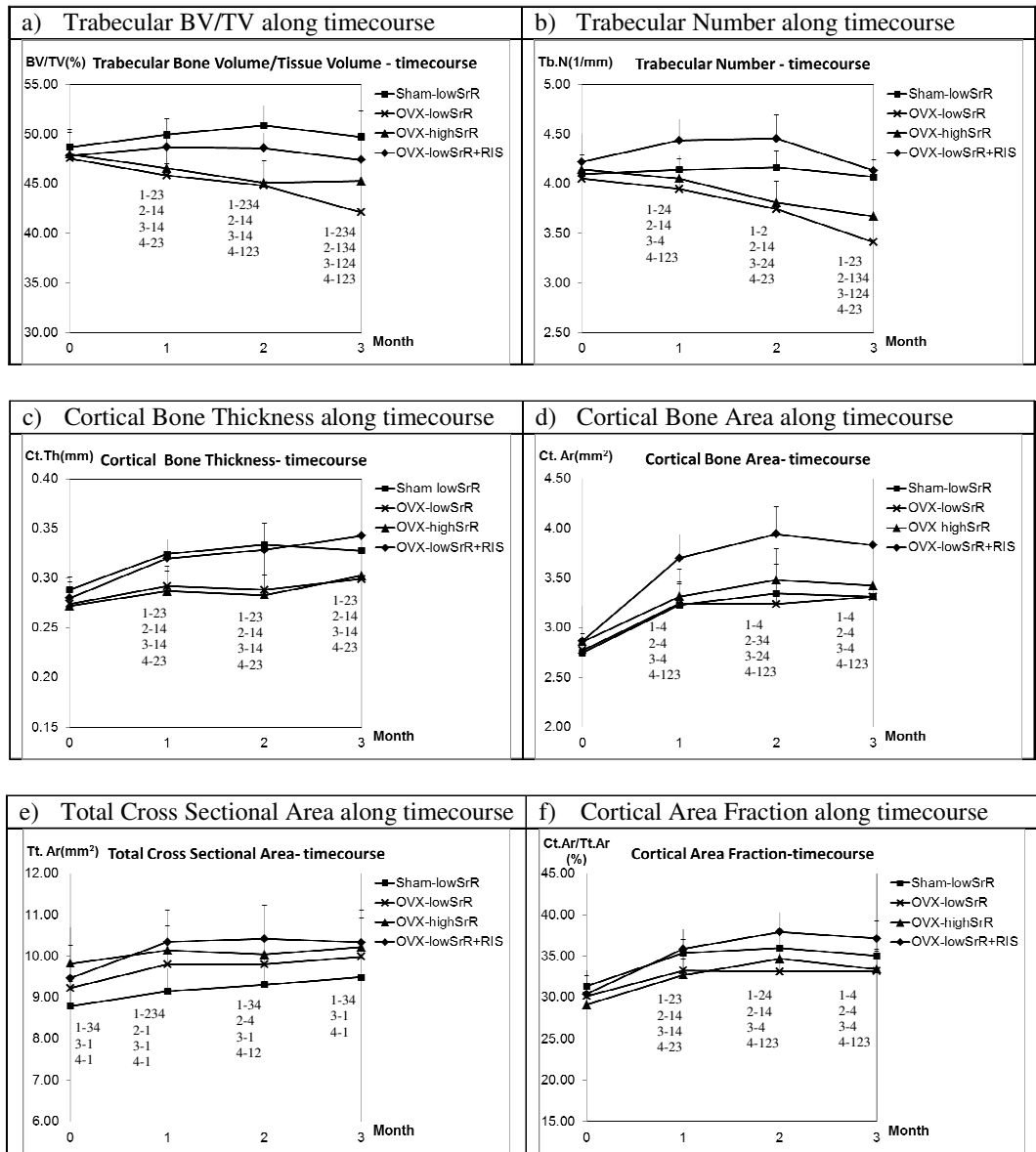


Figure 6-2 Longitudinal changes in structural parameters of vertebral column by Micro-CT along timecourse. The x-axis indicates the months after drug treatment. (1: Sham-lowSrR; 2: OVX-lowSrR; 3: OVX-highSrR; 4: OVX-lowSrR+RIS. Statistics result, e.g. “1-23” means 1 is significantly different from 2 and 3 while comparing results at the same time point.)

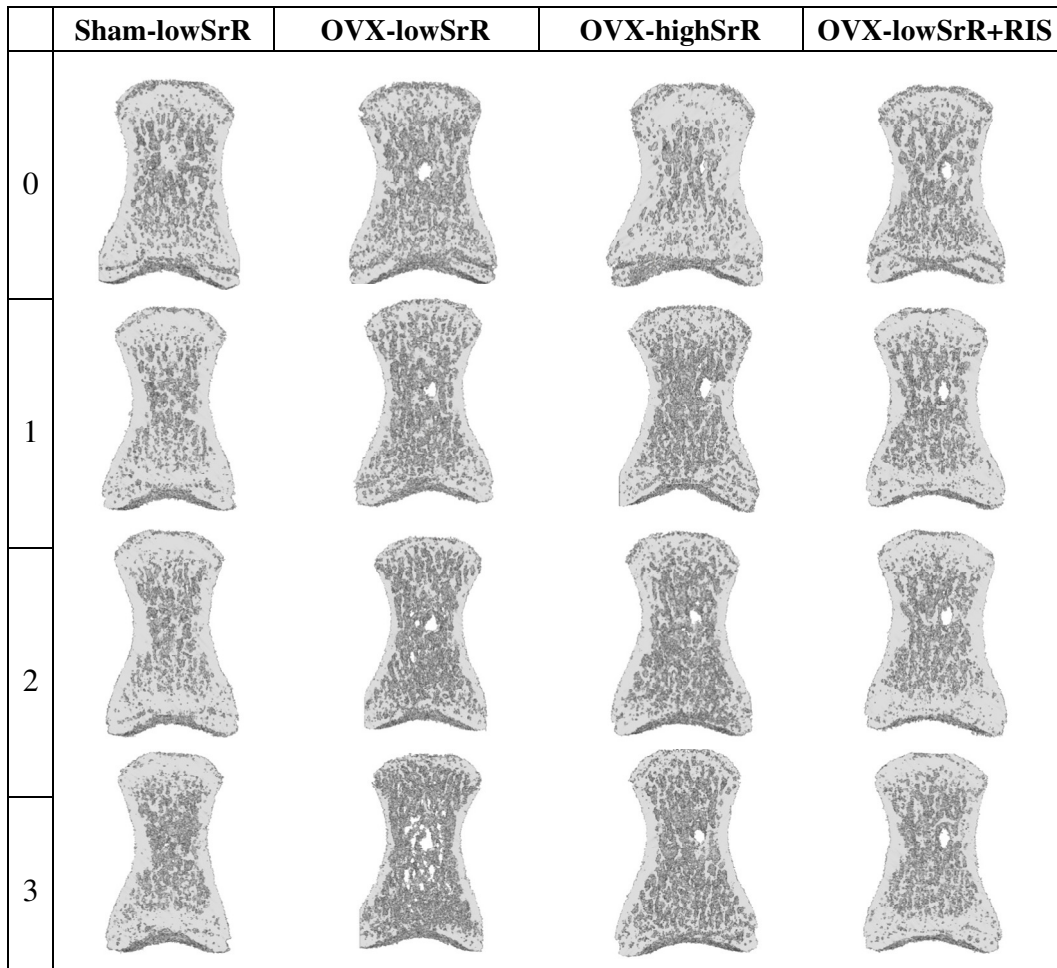


Figure 6-3 Morphological changes of bone architecture of rats in different groups. Longitudinal direction, 0, 1, 2, 3, indicates the month after drug treatments.

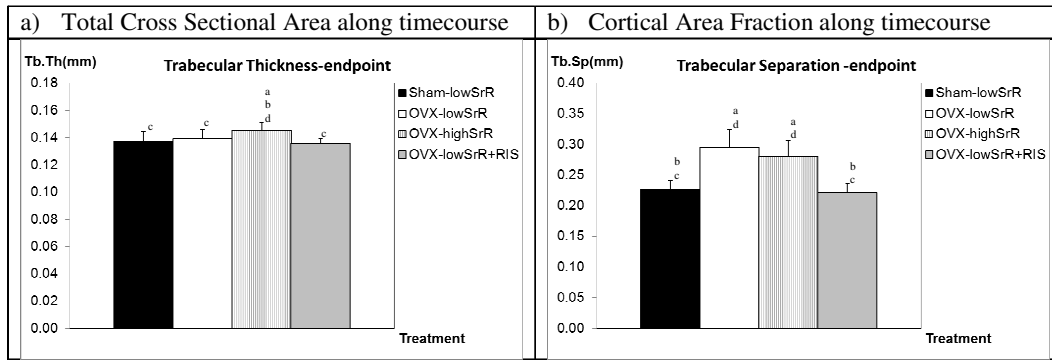


Figure 6-4 Changes in structural parameters of vertebral column by Micro-CT at the endpoint. (Significantly different from <sup>a</sup>Sham-lowSrR; <sup>b</sup>OVX-lowSrR; <sup>c</sup>OVX-highSrR; <sup>d</sup>OVX-lowSrR+RIS)

### Bone Mineral Deposition and Spatial Sr Distribution

Elemental EPMA maps clearly localized depositions of Sr, Ca and P. The deposition of Sr was seen on all maps of dosed rats, both from OVX and sham groups [Figure 6-5], and/or high or low dosage of Sr. Elemental Sr deposition was expected in areas where new bone formed during the treatment period [Li et al. 2010]. From our results, we determined that most elemental Sr was distributed on periosteal surfaces, at the primary spongiosum of growth plates, and regionally throughout the endosteal trabecular bone. Nonetheless, in comparison with other groups, OVX-lowSrR+RIS showed reduced trabecular bone with Sr deposition [Figure 6-5]. Regarding quantitative analysis, the Sr wt% of lowSrR treatment groups was  $\approx 0.5$  wt% and those values decreased from the cortical bone edge towards the center of the vertebral body. That amount of Sr deposition was recently reported to have no significant treatment effect [Ammann et al. 2004]. The Sr wt% of the bone in OVX-highSrR was greatly increased at  $\approx 2\%$ , predominantly at the periosteal edge and deposited at growth plates. It was also measured to decrease from the cortical bone edge towards the center of the

vertebral body [Figure 6-6(a)]. No significant variation in the mole ratio of (Ca+Sr)/P among groups or between regions with or without Sr was calculated. Therefore, it was feasible that Sr incorporated into the HA by substituting for elemental Ca in bone. In contrast, the concentration of Ca was in the order of 25~30 wt%.

From the results of EPMA, we concluded that it was readily possible to locate bone surfaces undergoing active bone remodelling and mineralization. However, as the area of bone scanned under EPMA was limited to a small surface, and only two dimensional maps were produced by EPMA, we elected to pursue synchrotron k-edge imaging as a means to visualize Sr distribution in remodelling bone in three dimensional models [Figure 6-6 (b)].

### **Material Property of Bone**

The Young's modulus determined in the center area of cortical bone, consisting predominantly of bone formed prior to drug treatment, did not show significant differences between any of the groups [Figure 6-7 (a)]. However, we measured significantly reduced values ( $p < 0.05$ ) in regions of newly formed bone regions (Edge) in the OVX-lowSrR+RIS compared to values from other groups. With respect to OVX-highSrR, the 2 wt% of Sr deposition in the OVX-highSrR group did not alter the Young's modulus, under the conditions we tested. The hardness of OVX-lowSrR+RIS in preformed bone regions (Center) was measured to be significantly lower than for that of Sham-lowSrR and OVX-lowSrR. We utilized those calculated values as references for calculating bone strength subsequently [Figure 6-7 (b)].

### **Bone Stiffness**

The stiffness of bone at the end of treatment reflected the effects of drugs on material properties, microarchitecture and geometry. Although OVX-lowSrR+RIS showed significantly lower E ( $p < 0.05$ ) in the newly formed bone than the bone formed before treatment, its stiffness was still as high as the stiffness of Sham-lowSrR [Figure 6-8]. OVX-highSrR showed slightly higher stiffness than OVX-lowSrR. However, the difference was not significant at this time point, although its trabecular BV/TV reflected significant higher values than OVX-lowSrR.

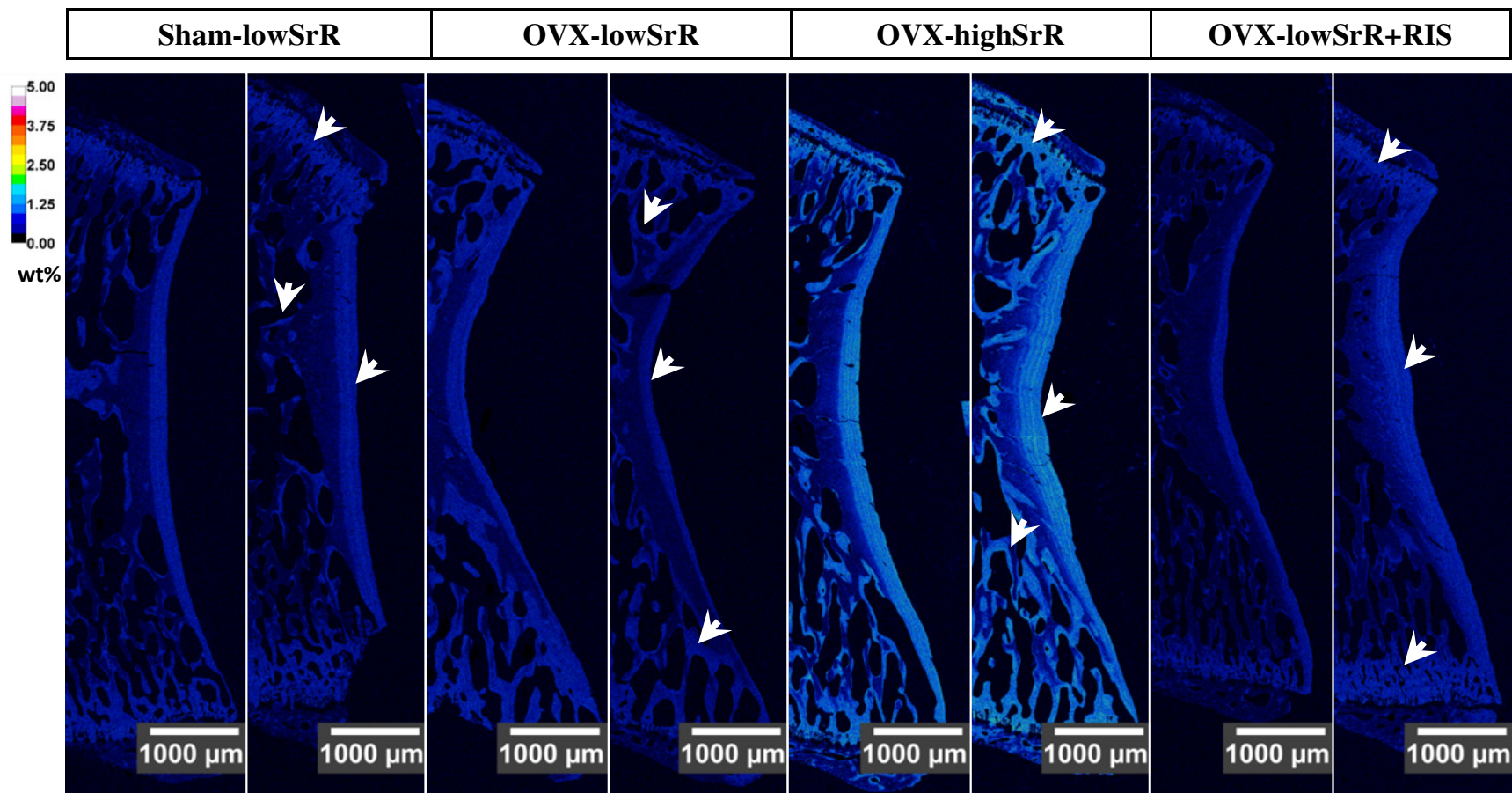


Figure 6-5 The distributions of elemental strontium in vertebra L5 (sagittal plane) in rats by EPMA after drug treatment for three months. Warmer color indicates higher concentrations of Sr. White arrows identify locations with Sr deposition.

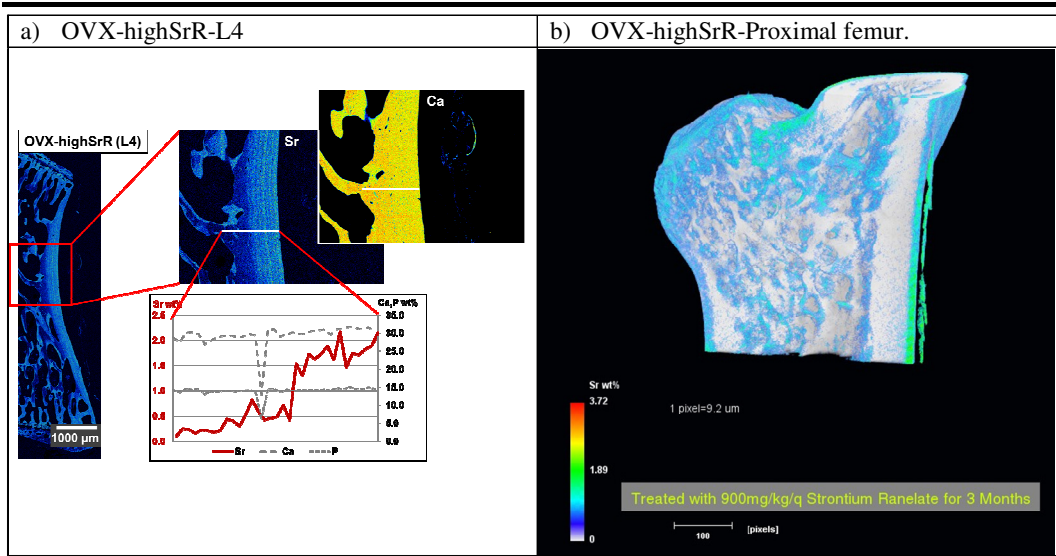


Figure 6-6 Distributions of elements in OVX-highSrR: (a) at the vertebra L4-the wt% of Ca, Sr and P along the line from the edge to the center of the cortical bone by EPMA. The concentration of Sr decreased from the edge (~ 2.0%) to the center. (b) at the proximal femur by synchrotron imaging. Colors show the distribution of Sr.

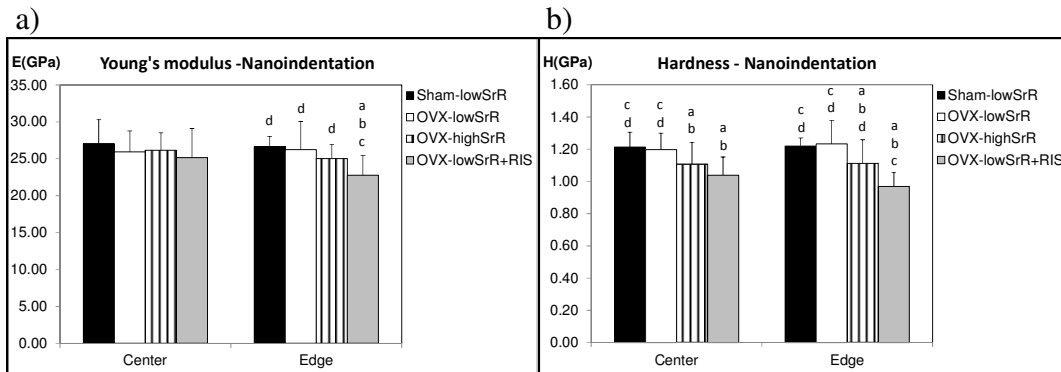


Figure 6-7 Material properties a) Young's Modulus (GPa) and b) Hardness (GPa) at Center and Edge regions of bone by nanoindentation tests at the endpoint. (Significantly different from <sup>a</sup>Sham-lowSrR; <sup>b</sup>OVX-lowSrR; <sup>c</sup>OVX-highSrR; <sup>d</sup>OVX-lowSrR+RIS)

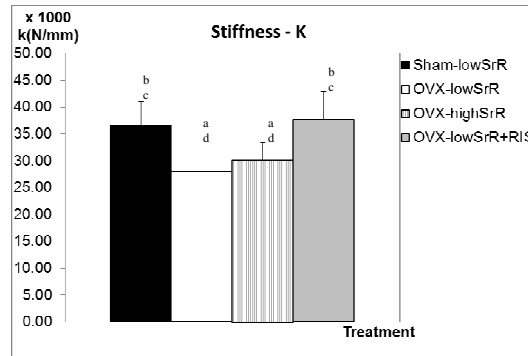


Figure 6-8 Stiffness of vertebral column in rats by finite element analysis at the endpoint. (Significantly different from <sup>a</sup>Sham-lowSrR; <sup>b</sup>OVX-lowSrR; <sup>c</sup>OVX-highSrR; <sup>d</sup>OVX-lowSrR+RIS)

## 6.5. Discussion

Our study demonstrated that in OVX rats, three months of treatment with high dose SrR (5 x 900mg/kg/wk) led to significant Sr incorporation into the HA of remodelling bone. Despite the incorporation of Sr, the ratio of (Ca+Sr)/P remained the same as that measured in untreated HA. Nonetheless, high dose SrR preserved trabecular BV/TV. In contrast, RIS treatment lowered the Young's modulus of newly formed bone but also significantly preserved BV/TV. Both OVX-lowSrR+RIS and OVX-highSrR were measured with reduced bone hardness in comparison to Sham-lowSrR and OVX-lowSrR on both Center and Edge regions. It is important to note that our study is limited to just three months of treatment, but nonetheless serves as valuable preliminary findings that predict the impact of long-term SrR and/or bisphosphonate drug treatment.

### Micro-CT

We found that our longitudinal evaluations of BV/TV in each treatment group were as expected, since OVX-lowSrR+RIS reduced resorptive bone losses

by inhibiting osteoclastic bone resorption. That effect of bone preservation was evident immediately upon the initiation of drug treatment. However, we also measured a relative reduction in new trabecular bone formation at later time points. High dose SrR was not effective at preserving BV/TV prior to the third month of therapy. There were few differences in Tb.Th among groups, except for OVX-highSrR, which showed a slightly higher value than other groups. That observation may serve as potential evidence of the purported anabolic effect of OVX-highSrR, as inhibiting bone resorption alone using BP did not increase Tb.Th. Our findings supported those recently published by Campbell and coworkers who measured that Tb.Th was increased after treatment with the anabolic drug, PTH [Campbell et al. 2011]. The increasing values for Tb.Sp in OVX-lowSrR and OVX-highSrR reflected the resorption and disappearance of trabeculae following the OVX surgery. In contrast, RIS potentially blocked bone resorption, and that was evidenced in the values of Tb.Sp. In contrast to the trabecular bone, all values relating to the cortical bone exhibited an upward trend. This was suggestive of bone apposition as a result of appositional bone growth as the juvenile rats aged, and those changes in bone volume needed to be considered independently of trabecular bone remodelling events. By the end of drug treatment, RIS preserved the thickness of OVX cortical bone to the same degree as for the Sham group. That may be explained by the inhibition of bone resorption on the endosteal surfaces of cortical bone following RIS treatment. However, the cortical area was measured to be significantly increased in the RIS treated rats over that measured in all other groups, and no significant differences were

measured in Tt.Ar. With respect to bone formation, our EPMA maps of spatial Sr deposition provided further evidence in support of our explanations.

### **Spatial Sr Depositions by EPMA**

Previous studies have shown that low dose SrR (225 mg/kg/wk) is not effective at increasing bone strength, even with two years of continuous treatment. Therefore, we elected to utilize this low “sub-therapeutic” dosage of SrR as a dynamic label of bone turnover. Our interest was in the spatial distribution and quantity of elemental Sr as measured in EPMA maps between treatment groups. From the EPMA maps of Sham-lowSrR and OVX-lowSrR (i.e., sub-therapeutic dosage, likely with no treatment effect), elemental Sr remained readily detected throughout the trabecular and cortical bone. Those findings suggest that elemental Sr may serve as a surrogate for Ca and will become incorporated into mineralizing bone during routine bone remodelling. That premise was supported in part by the reduced Sr incorporation in OVX-lowSrR+RIS treated rats. Bisphosphonates are used to inhibit bone resorption, but are known to also inhibit bone formation (to a lesser extent, as bone resorption and formation are coupled). In relation to Sr deposition in cortical bone, they were evidenced mainly on periosteal surfaces, in concentric lamellar layers. Sr depositions were also witnessed on the endosteal surfaces of cortical bone. Globally, OVX-highSrR showed more aggressive uptake of Sr – in terms of both areal distribution and concentration. According to our quantitative analysis, the highest concentration of Sr in OVX-highSrR was around 2 wt%; wt% of Ca was 25~30. Converting wt% to moles, the mole ratio of Sr with respect to Ca was  $\approx 3\%$ . Our results approximate those measured in

another study that examined the substitution of Ca by Sr [Li et al. 2010]. Although the dose of SrR used was much higher than that reported in our previous study, the Sr uptaken by bone was limited. The wt% of Sr was measured to be decreasing from the periosteal cortical edge towards the cortical bone center; that was suggestive of the loss of elemental Sr in mineralized bone crystals over time. Furthermore, no significant change in the ratio of (Ca+Sr) /P was found in all groups. Thus, our measurements provided evidence to support that Ca was replaced by Sr to form  $Sr_xCa_{10-x}(PO_4)_6(OH)_2$  (x: the number of Sr). Bisphosphonate treatment (RIS) did not increase the wt% of P, although it was likely that elemental P from the phosphonate moieties of RIS attached to the Ca primarily at actively remodelling bone sites [Papapoulos 2008]. The P connected to Ca of HA in bone was likely dissolved in acetone during the sample preparation. Thus, SrR changed the Sr content in bone, but RIS treatment did not alter the P concentration in bone. In the following section, we further discussed the potential change in bone material properties based on changes in bone elemental composition.

### **Nanoindentation**

The most curious finding with material properties was the E of strontium-hydroxyapatite (Sr-HA) bone compared to HA bone. With respect to the divalent cationic alkaline earth metals being studied, the E of Sr (15.7GPa) is less than the value of Ca (20GPa). In our rat bone study, 2 wt% of Sr in OVX-highSrR did not lower E significantly in comparison to the 0.5 wt% of Sr in Sham-lowSrR and OVX-lowSrR. The indented area of our nanoindenter was in the micron scale,

which may span several bone crystals. Therefore, the material properties we measured were actually averaged values of material in the micron range. In OVX-lowSrR+RIS, the E of newly formed bone was significantly lower than for bone in all other groups (and in preformed “old” bone), although the ratio of the inorganic elements was not different from other groups. That supports the notion that the bone remodelling process, in the presence of RIS, was altered during bone formation, and resulted in variations in the organic component, compared to the normal bone. The change in bone hardness in OVX-highSrR and OVX-lowSrR+RIS supported that drug intervention did, in fact, alter the material properties of dosed bone. The high dose Sr treatment maintained the same E as Sham and further showed a trend toward the preservation of BV/TV by the end of the third month of treatment. Although RIS treatment showed greater BV/TV than highSrR group, the lowered E may, in fact, weaken bone structure following long-term treatment, particularly once the reduction in BV/TV passed a certain point following OVX. That stands to reason, as hardness is related to the yield stress of the material [Pavlina and Van Tyne 2008]. Drug intervention appeared to lower bone hardness, particularly with RIS treatment. Thus, the bone that has incorporated RIS will reach a permanent deformation more quickly than untreated bone, or bone that has received SrR under the same loading conditions. FEA was performed to measure bone stiffness at the end of the study. At that time point, the bone stiffness of OVX-lowSrR+RIS remained significantly higher than for other OVX groups. However, that may not hold true following long-term bisphosphonate treatment. Accordingly, both the changes of E and H in OVX-

lowSrR+RIS served as the principal elements predictive for bone fracture after long-term treatment with bisphosphonates [Rizzoli et al. 2011].

### **Limitations**

Finding the relationship between Micro-CT images and bone stiffness to predict bone fracture remain challenging, either in lab studies or in clinical practice. The most difficult aspect of studies on the effects of drugs upon material properties is to relate short-term findings to long-term effects, according to the limited information collected. Our study was successful in providing evidence that bone material properties were altered following three months of bisphosphonate and/or SrR drug treatment, although these findings remain to be confirmed following long-term drug treatment. With respect to bone fracture, which ultimately is of most clinical importance, it must be recognized that bone stiffness remains as a descriptive index to the health of bone, and not as a direct indicator of imminent fracture.

### **6.6. Conclusion**

In summary, this study supported that high dose SrR treatment will preserve trabecular bone volume, which can be evidenced from BV/TV measurements following three months of SrR therapy. The significantly increased Tb.Th following high dose SrR therapy also provided potential evidence of the anabolic effects of SrR upon bone. Despite those findings, Young's modulus of OVX-highSrR showed no significant change in comparison to Sham-lowSrR, despite the 2 wt% increase of Sr deposited in the bone after treatment with high dose SrR.

Our findings suggest that treatment with high dose SrR maintains normal OVX bone stiffness better than untreated OVX bone, particularly with continuation of treatment. On the other hand, RIS treatment will rapidly preserve BV/TV following initiation of treatment. However, as the bone remodelling rate is greatly reduced, the BV/TV will at best reach a nominal level of remodelling balance, whilst the resulting Young's modulus and hardness will remain significantly lower than the values for untreated bone. Thus, the resistance to permanent deformation of bone following RIS treatment may be inferior to bone that received treatment with SrR, particularly after long-term treatment.

### **Acknowledgments**

The authors thank Dr. Jon I Johansson in the Research Support Group at Academic Information & Communication Technologies, University of Alberta for help with the resources of Avizo 6.3. We also thank Dr. Sergei Matveev for assistance with the EPMA analyses at the Vrije University, Amsterdam.

### **6.7. References**

Ammann P, Shen V, Robin B, Mauras Y, Bonjour J-P, Rizzoli R. Dec 2004. Strontium ranelate improves bone resistance by increasing bone mass and improving architecture in intact female rats. *J Bone Miner Res*, 19(12):2012-2020

Bonnelye E, Chabadel A, Saltel F, Jurdic P. Jan 2008. Dual effect of strontium ranelate: stimulation of osteoblast differentiation and inhibition of osteoclast formation and resorption in vitro. *Bone*, 42(1):129-138

Borgström F, Ström O, Coelho J, Johansson H, Oden A, McCloskey E, Kanis JA. Feb 2010. The cost-effectiveness of strontium ranelate in the UK for the management of osteoporosis. *Osteoporos Int*, 21(2):339-349

Bouxsein ML, Boyd SK, Christiansen BA, Guldberg RE, Jepsen KJ, Müller R. Jul 2010. Guidelines for assessment of bone microstructure in rodents using micro-computed tomography. *J Bone Miner Res*, 25(7):1468-1486

Campbell GM, Bernhardt R, Scharnweber D, Boyd SK. 2011. The bone architecture is enhanced with combined PTH and alendronate treatment compared to monotherapy while maintaining the state of surface mineralization in the OVX rat. *Bone*, 49(2):225-232

Chapurlat RD, Delmas PD. Apr 2006. Drug insight: Bisphosphonates for postmenopausal osteoporosis. *Nat Clin Pract Endocrinol Metab*, 2(4):211-9; quiz following 238

Cooper DML, Chapman LD, Carter Y, Wu Y, Panahifar A, Britz HM, Bewer B, Zhouping W, Duke MJM, Doschak M. Sep 2012. Three dimensional mapping of strontium in bone by dual energy k-edge subtraction imaging. *Phys Med Biol*, 57(18):5777-5786

Drake MT, Clarke BL, Khosla S. Sep 2008. Bisphosphonates: mechanism of action and role in clinical practice. *Mayo Clin Proc*, 83(9):1032-1045

Harris ST, Watts NB, Genant HK, McKeever CD, Hangartner T, Keller M,

Chesnut 3rd CH, Brown J, Eriksen EF, Hoseyni MS, Axelrod DW, Miller PD.

Oct 1999. Effects of risedronate treatment on vertebral and nonvertebral fractures in women with postmenopausal osteoporosis: a randomized controlled trial. vertebral efficacy with risedronate therapy (VERT) study group. *JAMA*, 282(14):1344-1352

Keen R, Osteoporosis: strategies for prevention and management. *Best Pract Res*

*Clin Rheumatol*, Feb 2007; 21(1):109-122

Krefting ER, Frenzel K, Tessarek J, Höhling HJ. Mar 1993. Strontium, a tracer to

study the transport of calcium in mineralizing tissues by electron probe microanalysis. *Scanning Microsc*, 7(1):203-207

Li C, Paris O, Siegel S, Roschger P, Paschalis EP, Klaushofer K, Fratzl P. May

2010. Strontium is incorporated into mineral crystals only in newly formed bone during strontium ranelate treatment. *J Bone Miner Res*, 25(5):968-975

Mashiba T, Turner CH, Hirano T, Forwood MR, Johnston CC, Burr DB. May

2001. Effects of suppressed bone turnover by bisphosphonates on microdamage accumulation and biomechanical properties in clinically relevant skeletal sites in beagles. *Bone*, 28(5):524-31

Odvina CV, Zerwekh JE, Sudhaker Rao D, Maalouf N, Gottschalk FA, Pak CYC.

Mar 2005. Severely suppressed bone turnover: a potential complication of alendronate therapy. *J Clin Endocrinol Metab*, 90(3):1294-1301

- Papapoulos SE. Feb 2011. Use of bisphosphonates in the management of postmenopausal osteoporosis. *Ann N Y Acad Sci*, 1218:15-32
- Papapoulos SE. Oct 2008. Bisphosphonates: how do they work? *Best Pract Res Clin Endocrinol Metab*, 22(5):831-847
- Pavlina EJ, Van Tyne CJ. 2008. Correlation of yield strength and tensile strength with hardness for steels. *Journal of Materials Engineering and Performance*, 17(6):888-893
- Pouchou JL, Pichoir F. 1985. "PAP"(phi-rho-z) procedure for improved quantitative microanalysis. In: Armstrong JT, editor. *Microbeam Analysis*. San Francisco Press: San Francisco, 104-106
- Reginster J, Minne HW, Sorensen OH, Hooper M, Roux C, Brandi ML, Lund B, Ethgen D, Pack S, Roumagnac I, Eastell R. 2000. Randomized trial of the effects of risedronate on vertebral fractures in women with established postmenopausal osteoporosis. vertebral efficacy with risedronate therapy (VERT) study group. *Osteoporos Int*, 11(1):83-91
- Rizzoli R, Akesson K, Bouxsein M, Kanis JA, Napoli N, Papapoulos S, Reginster J-Y, Cooper C. Feb 2011. Subtrochanteric fractures after long-term treatment with bisphosphonates: a European society on clinical and economic aspects of osteoporosis and osteoarthritis, and international osteoporosis foundation working group report. *Osteoporos Int*, 22(2):373-390
- Seeman E. Jun 2006. Strontium ranelate: vertebral and non-vertebral fracture risk reduction. *Curr Opin Rheumatol*, 18 Suppl 1:S17-S20

Shane E, Burr D, Ebeling PR, Abrahamsen B, Adler RA, Brown TD, Cheung AM, Cosman F, Curtis JR, Dell R, Dempster D, Einhorn TA, Genant HK, Geusens P, Klaushofer K, Koval K, Lane JM, McKiernan F, McKinney R, Ng A, Nieves J, O'Keefe R, Papapoulos S, Tet Sen H, van der Meulen MCH, Weinstein RS, Whyte M. Nov 2010. Atypical subtrochanteric and diaphyseal femoral fractures: report of a task force of the American society for bone and mineral research. *J Bone Miner Res*, American Society for Bone and Mineral Research. 25(11):2267-2294.

U.S. Food and Drug Administration (FDA). Oct 2010. FDA drug safety communication: Safety update for osteoporosis drugs, bisphosphonates, and atypical fractures. <http://www.fda.gov/drugs/drugsafety/ucm229009.htm>

Wang X, Allen MR, Burr DB, Lavernia EJ, Jeremić B, Fyhrie DP. Oct 2008. Identification of material parameters based on mohr-coulomb failure criterion for bisphosphonate treated canine vertebral cancellous bone. *Bone*, 43(4):775-780

Zhang J, Saag KG, Curtis JR. Aug 2011. Long-term safety concerns of antiresorptive therapy. *Rheum Dis Clin North Am*, 37(3):387-400, vi

## **Chapter 7**

### **General Discussion and Conclusion**

## 7.1. Discussion

This general discussion will focus on the effects of strontium ranelate (SrR) treatment of bone and the limitations of this research.

### 7.1.1. The effects of SrR on bone

In response to our original hypothesis, our results supported that the elemental composition and material properties of bone were changed after treatment with SrR and/or risedronate (RIS). Nonetheless, based upon the experimental studies conducted in this thesis, are we able to summarize the treatment effects which SrR has upon ovariectomized (OVX) rat bone? The following literature review of clinical studies on SrR bone disease may provide corroborative evidence to support our findings.

#### **Clinical Studies in Support of SrR for the Treatment of Bone Disease**

Several clinical trials have investigated the efficacy of SrR for the various bone diseases, different age levels of subjects, bone fracture locations (vertebral, non-vertebral and major fractures of the hip, wrist, pelvis and sacrum, ribs and sternum, clavicle and humerus), and the number of years after treatment. In addition to the monitoring of biomarkers in urine and blood, the bone mineral density (BMD) and the risk of fracture are common clinical outcome measures to evaluate drug efficacy. In addition, studies have evaluated patient quality of life (QoL) using surveys to indicate improvement of QoL after SrR treatment [Marquis et al. 2008]. Based on the results of that research, this review was focused on alternations of bone strength involving

indices of BMD and risk of fracture after SrR therapy for osteopenic bone disease. In addition, as the effects of long-term drug treatment are also of clinical relevance, this review was structured in ascending years, spanning one to eight years of treatment.

The clinical studies reviewed below were completed by treating patients with SrR 2g daily, with results compared to placebo dosed controls. Following one year of treatment with SrR, osteoporotic subjects showed significant increases in BMD of 5.9% at the lumbar spine, 2.6% at the femoral neck, and 2.7% at the total hip. The level of the bone formation marker, bone-specific alkaline phosphatase (BSAP), was also increased significantly at 6 and 12 months [Hwang et al. 2008]. For studies evaluating three years of SrR treatment, clinical trials were listed below by risk of fracture caused by osteoporosis (OP) or osteopenia. The treatment of peripheral osteoporosis study (TROPOS) trial followed the incidence of non-vertebral and hip fractures in osteoporotic patients treated with SrR. Results showed that there was a 16% reduction in the risk of non-vertebral fractures ( $p = 0.04$ ) and a 19% reduction in major fractures ( $p = 0.031$ ). Women with OP who were over 74 years of age had a 36% reduction in the risk of hip fracture ( $p = 0.046$ ). The difference in BMD between groups was 8.2% for femoral neck and 9.8% for total hip at 3 years [Adami 2006]. Those findings spurred our interest in examining the relationships between BMD and the reduction of fractures in different bone locations. An increase in the femoral neck BMD was associated with a proportional reduction in vertebral fracture

incidence (1% increased BMD versus a 3% reduction of vertebral fracture) [Bruyère et al. 2007a] and a decrease in hip fracture incidence (1% increased BMD versus a 7% reduction of hip fractures) [Bruyère et al. 2007b]. The baseline osteoporosis risk factors, such as family history of OP, baseline BMI, and addiction to smoking, were independent of the anti-vertebral fracture efficacy of SrR treatment for postmenopausal OP women [Roux et al. 2006]. Regarding treatment of osteoporotic patients over 80 years of age, treatment with strontium ranelate safely reduced the risk of vertebral and non-vertebral fractures in women with osteoporosis. In the intent-to-treat analysis, the risk of vertebral, non-vertebral, and clinical (symptomatic vertebral and non-vertebral) fractures was reduced within 1 year by 59% ( $p = 0.002$ ), 41% ( $p = 0.027$ ), and 37% ( $p = 0.012$ ), respectively. At the end of 3 years, vertebral, non-vertebral, and clinical fracture risks were reduced by 32% ( $p = 0.013$ ), 31% ( $p = 0.011$ ), and 22% ( $p = 0.040$ ), respectively [Seeman et al. 2006]. Overall, SrR has a broad range of anti-fracture efficacy on vertebrae, femoral neck fractures for osteoporotic and osteopenic patients during the three years of treatment, despite patients being over 80 years of age [Seeman 2006; Seeman et al. 2008].

For treatments over 4 years for 50~60 years old OP women, SrR significantly reduced the risk of vertebral fracture by 35% (relative risk 0.65; 95% CI 0.42 to 0.99,  $p < 0.05$ ) and increased BMD by 15.8% at lumbar spine and 7.1% at femoral neck [Roux et al. 2008]. SrR treatment over 5 years for 74 years old or older osteoporotic women showed that the risk of non-

vertebral fracture was reduced by 15%. The risk of hip fracture was decreased by 43% (relative risk 0.57 [95% confidence interval 0.33-0.97]), and the risk of vertebral fracture was decreased by 24% (relative risk 0.76 [95% CI 0.65-0.88]) [Reginster et al. 2008]. The treatment of osteoporotic women 80 years or older resulted in the 31% reduction of vertebral fracture risk (relative risk, RR=0.69; 95% confidence interval, CI 0.52-0.92), non-vertebral fracture risk by 27% (RR=0.73; 95% CI 0.57-0.95), major non-vertebral fracture risk by 33% (RR=0.67; 95% CI 0.50-0.89) and hip fracture risk by 24% (RR=0.76; 95% CI 0.50-1.15, not significant) [Seeman et al. 2010]. A study showed the risk of fracture was maintained over time from 3 years to 5 years. SrR treatment decreased the risk of vertebral fractures, by 41% over 3 years treatment, and by 49% within the first year of treatment. This risk of non-vertebral fractures was decreased by 16% and, in patients at high risk for such a fracture; the risk of hip fracture is decreased by 36% over 3 years treatment. Recent 5-year data showed that the anti-fracture efficacy is maintained over time [Roux 2008].

From the review of clinical studies, the reduction of fracture risk increased continuously from one to three years of treatment. Would the risk of fracture decrease continuously beyond three years treatment? Could the relationship between BMD and the risk of reduction be used as an evaluation method for long-term treatments? A long-term study of eight years of SrR treatment delineated the possible answer to those questions. Postmenopausal osteoporotic women having participated in the 5-year efficacy trials of the

Spinal Osteoporosis Therapeutic Intervention (SOTI) and TROPOS were invited to enter a 3-year open-label extension study. The cumulative incidences of new vertebral and non-vertebral fractures (13.7% and 12.0%, respectively) over the years 6 to 8 were non-statistically different from the cumulative incidences in the first 3 years of the original studies (11.5% and 9.6%). The BMD at lumbar spine, femoral neck, and total hip increased throughout the 8-year period [Reginster et al. 2009]. In summary, the review of clinical studies concluded that: 1) the treatment of SrR for OP patients increased BMD over time, however, 2) reduction of fracture risk was only effective in the first three years of treatments; it was sustained after three years.

The summary of those clinical studies of SrR treatment in osteoporotic patients can be explained scientifically by the outcomes of our research. Firstly, elemental Sr incorporated into bone through bone remodelling (Chapter 2) confirmed that regions of bone were continually renewed during the course of drug treatment. As a result of Sr deposition in bone, the BMD will be biased by the increased content of elemental Sr under X-ray imaging (Chapter 4). That was perfectly explained by the increase of BMD over time in clinical trials. Secondly, in our research, experiments showed that the bone volume/tissue volume (BV/TV) of SrR treated OVX rat bone increased gradually after treatment but was maintained at the same level after 2 months of treatment (Chapter 5). In addition, nanoindentation results indicated that Sr deposition in bone did not weaken the material properties of bone compared

to that of sham operated controls (Chapter 5). In light of those experimental results, our findings support those of the clinical trials in that the reduction in fracture risk was effective in the first three years of treatment but remained steady afterward.

In the aggregate, our results support the effects of SrR in maintaining bone strength during the treatment of OP.

### 7.1.2. Limitation of this research

In this research, we have developed methodology capable of validating bone strength in OP rat bone after drug treatment. However, other than for the micro-computed tomography (Micro-CT) scans undertaken in this research, the techniques used for detecting bone compositions and material properties remain limited to ex-vivo assessment. It is important to question if alternatives of those methods can be undertaken in-vivo?

To undertake electron probe micro analysis (EPMA), the evaluations need to be performed under high vacuum in order to avoid the collision of non-related atomic particles during the emission of electrons. EPMA can distinguish different elements by the characteristic X-ray energy of each element. Other than EPMA, X-ray fluorescence (XRF) and proton/particle excited X-ray emission analysis (PIXE) are also based on the principles of characteristic X-rays to identify and quantify specific elements. However, the excitation beam source for XRF and PIXE are X-rays and protons, which can be introduced in the air. In-vivo XRF has been applied in detecting elemental

Sr in various studies [Moise et al. 2012; Wohl et al. 2013]. However, In-vivo XRF is limited based on assumptions related to bone strontium distribution, in order to obtain a quantitative strontium measurement [Zamburlini et al. 2009] and by the low resolution because of background noise. Conversely, PIXE has greater detection accuracy than XRF and was also developed to image elemental compositions [Kawamura et al. 2007], although published studies to date are limited to small creatures, such as insects [Ohkura et al. 2011]. One major limitation of this research is the lack of direct evidence of drug effects following long-term drug treatment. The rat model we employed is not conducive for long-term study, as the life span of rats is generally 1~2 years. It may be possible to confirm our experimental results in-vivo in larger animal models.

### 7.2. Conclusion

In this research, we have presented a scientific process, from lab experiments to computer simulations, capable of validating the effects of drugs on OVX rat bone compositional and material properties. The effects were represented by evaluating the bone strength which can be indirectly interpreted by BV/TV, BMD and fractal dimension (FD), as well as by other histomorphometric indices ascertained by Micro-CT, elemental compositions by EPMA and material properties by nanoindentation test, and the stiffness of bone by FEA. The complex process of implementing FEA from Micro-CT scans to finite element modelling was also explained and simplified in this research.

The drugs, SrR and RIS, were shown to be effective at changing either the elemental composition of bone or the mechanical properties of bone material in this research. The treatment of SrR for three months in OVX rats resulted in ~2 wt% of Sr depositions, while permitting new bone to form during treatment. Despite those events, the integration of elemental Sr into bone crystals did not alter the material properties of bone. Bone strength of Sr-laden bone remained dominated by the change of bone microarchitecture, which improved significantly over untreated OP bone after high-dose treatment with SrR for three months. On the other hand, treatment with the bisphosphonate drug RIS decreased the material strength of bone. The strength of RIS treated bone remained dominated by bone microarchitecture. Extrapolating our results, long-term treatment with SrR may preserve bone strength. However, long-term treatment with RIS will conversely result in the erosion of bone strength. Our findings may help explain the emerging trend of spontaneous femoral shaft fractures in patients following long-term BP drug treatment.

One primary concern of SrR therapy for the treatment of OP was the bias of increased BMD resulting from elemental Sr under X-ray imaging. Our research confirmed that bias and established that every 1 mole% of Sr/Sr+Ca in bone will result in a corresponding increase of BMD by 6.24%. That bias can be corrected with a known ratio of Sr to Sr+Ca element relative to that bone sample.

### 7.3. Future Direction

The experimental methods developed in this research are robust and capable of evaluating drug effects upon bone strength, and ready for cross-application to other bone drug treatments.

With respect to the evaluation of bone strength, further efforts are required in order to develop appropriate evaluation techniques, either direct or indirect, for use in the clinic.

### 7.4. References

Adami S. Feb 2006. Protelos: nonvertebral and hip antifracture efficacy in postmenopausal osteoporosis. *Bone*, 38(2 Suppl 1):23-27

Bruyère O, Roux C, Badurski J, Isaia G, de Vernejoul MC, Cannata J, Ortolani S, Slosman D, Detilleux J, Reginster JY. Dec 2007b. Relationship between change in femoral neck bone mineral density and hip fracture incidence during treatment with strontium ranelate. *Curr Med Res Opin*, 23(12):3041-3045

Bruyère O, Roux C, Detilleux J, Slosman DO, Spector TD, Fardellone P, Brixen K, Devogelaer J-P, Diaz-Curiel M, Albanese C, Kaufman J-M, Pors-Nielsen S, Reginster JY. Aug 2007a. Relationship between bone mineral density changes and fracture risk reduction in patients treated with strontium ranelate. *J Clin Endocrinol Metab*, 92(8):3076-3081

Hwang JS, J Chen F, Yang TS, Wu DJ, Tsai KS, Ho C, Wu CH, Su SL, C. Wang J, Tu ST. Nov 2008. The effects of strontium ranelate in asian women with postmenopausal osteoporosis. *Calcif Tissue Int*, 83(5):308-314

Kawamura Y, Ishii K, Yamazaki H, Matsuyama S, Kikuchi Y, Yamaguchi T, Watanabe Y, Oyama R, Momose G, Ishizaki A, Tsuboi S, Yamanaka K, Watanabe M. 2007. In-Vivo Elemental, Analysis By, and PIXE- $\mu$ -CT. *Int J PIXE*, 17(1 & 2):41-46

Marquis P, Roux C, de la Loge C, Diaz-Curiel M, Cormier C, Isaia G, Badurski J, Wark J, Meunier PJ. Apr 2008. Strontium ranelate prevents quality of life impairment in post-menopausal women with established vertebral osteoporosis. *Osteoporos Int*, 19(4):503-510

Moise H, Adachi JD, Chettle DR, Pejović-Milić A. Jul 2012. Monitoring bone strontium levels of an osteoporotic subject due to self-administration of strontium citrate with a novel diagnostic tool, in vivo XRF: A case study. *Bone*, 51(1):93-97

Ohkura S, Ishii K, Matsuyama S, Terakawa A, Kikuchi Y, Kawamura Y, Catella G, Hashimoto Y, Fujikawa M, Hamada N et al. May 2011. In vivo 3D imaging of drosophila melanogaster using PIXE-micron-CT. *X-Ray Spectrom*, 40(3):191-193

Reginster JY, Bruyère O, Sawicki A, Roces-Varela A, Fardellone P, Roberts A, Devogelaer JP. Dec 2009. Long-term treatment of postmenopausal

- osteoporosis with strontium ranelate: results at 8 years. *Bone*, 45(6):1059-1064
- Reginster JY, Felsenberg D, Boonen S, Diez-Perez A, Rizzoli R, Brandi M-L, Spector TD, Brixen K, Goemaere S, Cormier C, Balogh A, Delmas PD, Meunier PJ. Jun 2008. Effects of long-term strontium ranelate treatment on the risk of nonvertebral and vertebral fractures in postmenopausal osteoporosis: Results of a five-year, randomized, placebo-controlled trial. *Arthritis Rheum*, 58(6):1687-1695
- Roux C, Fechtenbaum J, Kolta S, Isaia G, Cannata Andia JB, Devogelaer JP. Dec 2008. Strontium ranelate reduces the risk of vertebral fracture in young postmenopausal women with severe osteoporosis. *Ann Rheum Dis*, 67(12):1736-1738
- Roux C, Reginster JY, Fechtenbaum J, Kolta S, Sawicki A, Tulassay Z, Luisetto G, Padrino JM, Doyle D, Prince R, Fardellone P, Sorensen OH, Meunier PJ. Apr 2006. Vertebral fracture risk reduction with strontium ranelate in women with postmenopausal osteoporosis is independent of baseline risk factors. *J Bone Miner Res*, 21(4):536-542
- Roux C. Jul 2008. Strontium ranelate: short- and long-term benefits for postmenopausal women with osteoporosis. *Rheumatology (Oxford)*, 47 Suppl 4:iv20-iv22
- Seeman E, Boonen S, Borgström F, Vellas B, Aquino J-P, Semler J, Benhamou CL, Kaufman JM, Reginster JY. Apr 2010. Five years treatment with

- strontium ranelate reduces vertebral and nonvertebral fractures and increases the number and quality of remaining life-years in women over 80 years of age. *Bone*, 46(4):1038-1042
- Seeman E, Devogelaer JP, Lorenc R, Spector T, Brixen K, Balogh A, Stucki G, Reginster JY. Mar 2008. Strontium ranelate reduces the risk of vertebral fractures in patients with osteopenia. *J Bone Miner Res*, 23(3):433-438
- Seeman E, Vellas B, Benhamou C, Aquino JP, Semler J, Kaufman JM, Hoszowski K, Varela AR, Fiore C, Brixen K, Reginster JY, Boonen S. Jul 2006. Strontium ranelate reduces the risk of vertebral and nonvertebral fractures in women eighty years of age and older. *J Bone Miner Res*, 21(7):1113-1120
- Seeman E. Jun 2006. Strontium ranelate: vertebral and non-vertebral fracture risk reduction. *Curr Opin Rheumatol*, 18 Suppl 1:S17-S20
- Wohl GR, Chettle DR, Pejović-Milić A, Druchok C, Webber CE, Adachi JD, Beattie KA. Jan 2013. Accumulation of bone strontium measured by in vivo XRF in rats supplemented with strontium citrate and strontium ranelate. *Bone*, 52(1):63-69
- Zamburlini M, Campbell JL, de Silveira G, Butler R, Pejović-Milić A, Chettle DR. Jul 2009. Strontium depth distribution in human bone measured by micro-PIXE. *X-Ray Spectrom*, 38(4):271-277